THE EFFECT OF MICROSTRUCTURE ON THE STRAIN LOCALIZATION IN COARSE-GRAINED AA5754 SHEETS

By

ZHU, GUOZHEN, B.Eng.

A Thesis

Submitted to the School of Graduate Studies

in Partial Fulfilment of the Requirements

for the Degree

Master of Applied Science

McMaster University

MASTER OF APPLIED SCIENCE (2009) McMaster University

Department of Materials Science and Engineering Hamilton, Ontario

TITLE: The Effect of Microstructure on the Strain Localization in Coarse-grained AA5754 Sheets

AUTHOR: Guozhen. Zhu, B.Eng.

SUPERVISOR: Dr. David S. Wilkinson

NUMBER OF PAGES: xii, 113

ABSTRACT

Al-Mg sheets (5xxx series) for body-in-white (BIW) application are mostly used for automotive structural parts due to their specific combination of formability and strength. The limiting behavior for the wide application of AA5754 sheets is strain localization. The effect of microstructure inhomogeneties on strain localization have recently been attracting a great deal of interest but not fully understood. In this present work, the effect of grain-level microstructure inhomogeneties in AA 5754 sheets is investigated.

Uniaxial tensile experiments combined with two 2-dimensional Digital image correlation (DIC) techniques have been performed on coarse-grained specimens to evaluate the deformations of individual grains. Grain orientations and their evolution were measured by the electron backscattered diffraction (EBSD) technique, and surface features such as slip traces were observed by optical microscopy.

The regions of high local strain ('hot spots') within coarse-grained samples nucleate at a very early stage of deformation and most of them continuously grow throughout most deformation stages. 'Hot spots' are correlated with 'soft' grains (i.e. grains with high Schmid factors) and soft-evolution grains (i.e. grains with the <101> direction close to tensile axis).

ACKNOWLEDGEMENT

My first and foremost thanks go to my supervisor Dr. Wilkinson for his guidance and suggestions for my project. It has always been an enjoyable experience to discuss with him. He always helped me to find the valuable points and links among those complex experimental results.

I would like to express my sincere thankfulness to Dr. Xiaohua Hu for his advice and encouragement over the past two years. I got lots of valuable suggestions from the discussions with Dr. Hu about my experiments and data analysis.

My special thanks are given to Dr. Jidong Kang for his help on the set-up of tensile tests with two 2-dimensional DIC and his suggestions on writing thesis.

The assistance of the following people at McMaster University and GM R&D center is also appresciated:

Dr. Michael Bruhis and Mr. Rob Lemmon for DIC and mechanical testing

Dr. Raj K Mishra and Mr. Bob Kubic for EBSD and insitu tensile testing

Mr. Doug Culley and Mr. Chris Butcher for metallography

Dr. Yansheng Liu for one etching method

I also obtained enormous help from my friends. I am truly grateful to Tom (Tihe) Zhou, Yuepeng Zhang, Paul Okrutny, Juan Kong and other good friends. Finally, the support of my father and mother were very much appreciated.

TABLE OF CONTENTS

LIST OF FIGURES:

LIST OF TABLES

CHAPTER ONE

INTRODUCTION

Based on economical and environmental pressure to produce light weight vehicles, there is growing interest in aluminum alloys within the automotive industry due to their unique set of properties: high strength/stiffness to weight ratio, good formability, good corrosion resistance, recycling potential and so on. Aluminum was applied to car body panels in early automotive industries, then gave its dominant position to steel resulting from high cost and low productivity, while now Al gains worldwide attention for its weight reduction potential. When substituted of steel, aluminum can save up to 50% of the body-in-white (BIW) mass and up to 20%-30% total vehicle weight. However, raw material and manufacturing cost impedes its large-scale application.

1.1 Background: Aluminum Alloy AA5754 sheets

Non-heat treatable Al-Mg sheets (5xxx series) for body-in-white (BIW) application are mostly used for internal structural members due to their specific combination of formability and strength. European car makers also use 5xxx alloys as the materials of choice for outer panels and they produce these alloys in the SSF (Stretcher Strain Free) condition to overcome the strain markings problems due to PLC effect and Lüders-band formation [1]. When alloyed with magnesium, the 5xxx series are moderate-to-high-strength non-work-hardenable alloys. As the magnesium concentration is increased, so is the strength of the alloy [2]. However, higher magnesium content (>3wt%) limits the intergranular corrosion resistance, especially at elevated temperature and high stress [3].

Recently AA5754 alloys combining good formability and good intergranular corrosion resistance, have received increasing attention for structural applications. Traditionally, AA5754 sheets are made using a semi-continuous process called the direct-chill casting (DC). Molten alloys first form DC ingots through a water-cooled mold, following a homogenizing treatment, and then hot rolled to final gauge and finished in an annealing process. The long post-solidification process and large casting thickness (typically ~ 0.5m) offer DC alloys homogeneous and fine structure but at high price.

Continuous strip casting (CC) is a cheaper alternative method to make aluminum sheets by eliminating the hot rolling process. Molten metal enters a cavity set by two cooled counter-rotating rolls or belts and is then solidified at a high cooling rate. The short thermo-mechanical process limits the development of homogeneous microstructure and further affects the formability of CC alloys. The comparable cost with steel on a per car basis is the cardinal driving force for the development of the CC procedure.

1.2 Research Motivation:

A considerable body of work was performed in order to concentrate on the development of aluminum material properties and produce cost-effective aluminum sheets to replace steel. This was done by finding more cost-effective manufacturing methods to make aluminum products, developing new alloy systems by changing components or adding some elements, improving mechanical properties of the existing alloy systems, even trying to reduce cost through other aspects such as easy painting ability and so on.

The AA5754 sheets produced using the DC method provide a more homogeneous microstructure and better formability while those produced using the CC method have good economic value. Previous results [4] showed that the failure type of AA5754 is flow instability and the spatial distribution of second-phase particles causes the early failure of CC sheets. Therefore, it is interesting and valuable to study their flow instability process, or so-called strain localization process.

The formation and development of shear bands within this alloys is an attractive study with many details in dispute. Bifurcation and imperfection theories were developed to describe such phenomena; however none of these theories could predict the localization region accurately and practically. Considering industrial type sheets, any inhomogeneities including geometric and microstructural aspects could be referred to as initial defects and no clear description of the influence of microstructural inhomogeneities on strain localization was presented until now.

The sheet manufacturing industry urgently calls for an intelligent-operating method to describe and predict the deformation process. However, in order to improve the prediction accuracy, microstructural effects need to be considered.

The biggest challenge with microstructural-based models is that they are often time consuming at the specimen scale. These challenges were overcome and fast-calculating models were built in order to make calculations finish within a reasonable amount of time. Now experiments are needed in order to calibrate the models.

1.3 Objectives and Structure of the Thesis

The objective of the present work is to develop a good comprehension of the microstructure and mechanical properties relationship emphasizing the strain localization process in AA5754 alloys. Uniaxial tensile experiments have been performed on coarse-grained specimens to magnify the effect of super-grain level inhomogeneities and then to calibrate the fast-calculating model.

The structure of the current thesis is as follows. Chapter 2 systematically reviews the previous work on these important aspects relating to the current topic. Chapter 3 describes the experimental methods and techniques applied in the present work. In Chapter 4, we present the principal experimental results: obtaining and characterization of coarse-grained structure, the results of uniaxial tensile tests of coarse-grained specimens and then the characterization of deformed microstructure. Following the experimental results, Chapter 5 gives the analysis of the microstructure-deformation relationship, including the microstructure effect on strain localization and the comparison with experimental results and simulation. Conclusions are stated in Chapter 6.

CHAPTER TWO

LITERATURE REVIEW

The primary limiting factor for producing high quality aluminum-magnesium sheets is their production and manufacturing cost. Cost effective production processes (i.e. CC) usually lead to poor mechanical properties due to their heterogeneous microstructure. In this chapter, we will start by reviewing the sequence of heterogeneous deformation processes during uniaxial tensile deformation. Along with sequence of deformation we will focus on reasons causing strain concentration, mainly focusing on material inhomogeneities. After that, we briefly summarize microstructure-based models available in the literature to account for the grain-level inhomogeneities and place emphasis on the development and critical results of fast-calculating full crystal plasticity (CPFEM) and Taylor-based finite element models (FE-TBH) which are developed in the current group. We close this chapter with a brief critical assessment.

2.1 The Sequence of Heterogeneous Deformation Processes

The formability of sheets dominates their application for manufacturing body panels of cars. The limiting behaviors for sheet forming are described by two kinds of events: fracture and deformation instability. Fracture limit is defined as that required for separating materials while the limit of deformation instability is defined as the transition of stable-to-unstable deformation. In general, elastic instability is frequently in the form of buckling while plastic instability is usually due to the onset of (localized) necking.

For Al-Mg sheets, plastic instability is the limiting behavior. As a general rule, plastic instability is a type of plastic flow localization process, short for flow localization [5] or shear localization [6] which means concentrated deformation in a narrow region. The deformation process is heterogeneous, both at the macro-level and micro-level [7]. In this part however, only the macroscopic flow localization process is considered.

First the general deformation procedures, then all kinds of strain concentration phenomena in Al-Mg alloys (Portevin-Le Châtelier (PLC) bands, diffuse necking band and localized necking bands) are considered.

2.1.1 General Tensile Response of Al-Mg Sheets

A typical engineering stress-strain curve (Figure 2-1) for tensile sheets includes three regions [8]:

I). Region I: Pertains to macro relatively homogeneous deformation until the load reaches its maximum. This region describes the tensile response before diffuse necking. However, since elastic and plastic deformations have different mathematical models, researchers prefer yield point as the initial state of Region I.

II). Region II: Localized deformation with near constant load. Region II is the region of so-called diffuse necking process, which is the intermediate procedure between the onset of instability and the development to localized necking. The deformation is non-uniform while still relatively stable.

III). Region III: Localized necking is presented with the load declining rapidly. In Region III, the cross-sectional reduction in area is mainly contributed by thickness reduction. Deformation becomes unstable and concentrates to a narrow band.

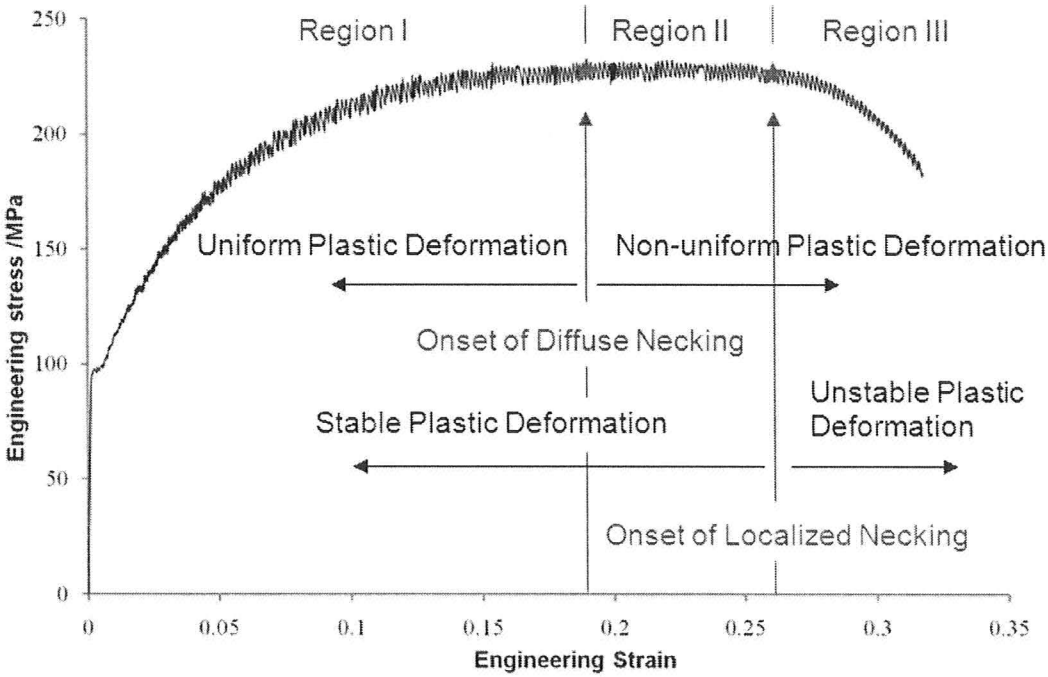

Figure 2-1 Typical engineering stress-strain curve of AA5754 sheets

2.1.2 Portevin-Le Châtelier (PLC) bands

In solute-strengthened alloys the Portevin-Le Châtelier (PLC) effect, denoted as the nucleation and propagation of PLC bands, emerges at small

strain, approximately at the beginning stages of plastic deformation, which hints that macroscopically heterogeneous deformation starts at rather small strain.

At the macroscopic level, serrated plastic flow appears in the stress-strain or stress-time curves under a certain range of temperature and strain rates. Strain concentration zones show up as PLC bands on the sample surface with a typical width in the range of μm to mm. This phenomenon is associated to negative strain rate sensitivity (nSRS) [9]. During deformation, relatively high-strain-rate zones become these soft regions, which lead to the nucleation sites of local instability. PLC bands leave markings, which are visualized using contours of surface roughness data [10-11].

Experiments on AA5052-H32 alloys [12] proposed that no threshold strain exists in thinner or mechanical polished samples implying that the initialization threshold of stress-based bands is at the meso-scale when compared to the sample thickness. Kok [13-14] showed that three PLC band types are generated and are transmitted without defects. In other words, PLC bands are due to the internal properties of materials related to the texture and its evolution and also have strong correlation with surface roughness.

According to the initiation and motion of PLC bands there is a widely acceptable phenomenological classification for their types: Type A, B and C [11, 15-16]. Type A bands usually nucleate at one sample end and then continuously move to another end. The amplitude of stress under this type does not go through significant changes. Type B usually has an oscillatory or intermittent propagation, saying that this series of bands occur one after another at regular interval time and space. Compared to Type A, Type B causes much larger change in stress serration. Type C bands nucleate randomly in space but with regular frequency, which brings out irregularly periodic load serrations.

Two possible growth mechanisms were proposed and related to different bands [17-18]. Type A and B bands tend to associate with the first mechanism. A sample-scale band nucleates at the specimen surface and then expands along the tensile axis until stress relaxation. Type C bands are placed in the second category. An embryo band appears at the lateral sample surface and grows into the bulk at an angle on the frontal plane.

The micro-mechanism for such serrated plastic flow is due to dynamic strain ageing (DSA) and its details are still in debate. Glide dislocations pile up at these obstructions such as solutes or solute clusters, and the growth of PLC bands starts when those stacked dislocations are reactivated.

2.1.3 Necking

Necking is the occurrence of non-uniform plastic flow[19] and indicated by concentrated cross-sectional reduction in area in a specific region. Ductile round bar samples have only necking before fracture. As a counterpart, the necking process of tensile sheets is more complex since specimens lack shape symmetry. The necking process of sheet bars is generally classified as: (a) diffuse necking, describing the process that deformation is concentrated in an appreciable region, the length of which is around the width of sheet bars; (b) localized necking, during this process the reduction of cross-sectional area extends over the length compared to the samples thickness.

Criteria for diffuse necking in uniaxial tension were well developed. Considère[20] derived a criterion (E2-1) under Holloman law for strain-rate-insensitive materials:

$$\frac{d\sigma}{d\varepsilon}=\sigma \text{ or } \frac{d\sigma}{de}=\frac{\sigma}{1+e} \qquad \text{E2-1}$$

in which, σ, ε and e are the true stress, true strain and engineering strain, respectively. As for the strain-rate-sensitive materials such as AA5754, Hart [21] considered the effect of strain rate and defined the dimensionless strain-hardening coefficient γ:

$$\gamma = \frac{1}{\sigma}\left(\frac{\partial \sigma}{\partial \varepsilon}\right)_{\dot{\varepsilon},T} \qquad \text{E2-2}$$

For stable uniform deformation, $\gamma + m \geq 1$, where m is the strain-rate-sensitivity coefficient. Therefore, Hart criterion for diffuse neck point is: γ+m=1.

Localized necking happens when the flow focuses in a narrow band, i.e. shear band, along a special direction in poly-crystals or slips localize in single crystal [22-23]. Bifurcation and defect analysis were well developed to describe and predict localized necking.

Bifurcation theories established the criterion for localized necking in specimens with the initial homogenous matrix. McClintock [24] gave the upper bound for the occurrence of shear instability in which shear localization happens when the load for shearing is less than that for homogeneous flow in uniaxial tension. Hill [25] proposed the linear description of localized necking under plane stress condition of strain-rate insensitive materials (E2-3). The Hill criterion is applied in the special case: one of the two in-plane principal strains is positive and the other is negative. Under such condition, the orientation of the possible localized necking site is the direction of zero extension.

$$\frac{1}{\sigma}\frac{d\sigma}{d\varepsilon} \leq \frac{\partial f}{\partial f}\frac{\partial \sigma_1}{\partial \sigma} + \frac{\partial f}{\partial f}\frac{\partial \sigma_2}{\partial \sigma} \qquad \text{E2-3}$$

where, σ_1 and σ_2 are the two in-plane principal strains and f is the yield function.

Defect analysis assumed that imperfections exist from the beginning. Marciniak and Kuczynski methods (M-K methods) [26] assumed that deformation

localization occurs at the pre-existing defect, the region with geometrical or material heterogeneities. Shown in Figure 2.2(a), region B, so-called groove or trough, experiences a proportional load. Defect function $f = t_{Ao}/t_{Bo}$ is defined as the ratio of initial thickness in region A and B. To satisfy the equilibrium condition $\sigma_{1A}t_A = \sigma_{1B}t_B$ and compatibility condition $\varepsilon_{2A} = \varepsilon_{2B}$, localized necking happens when the weak region reaches its maximum strain.

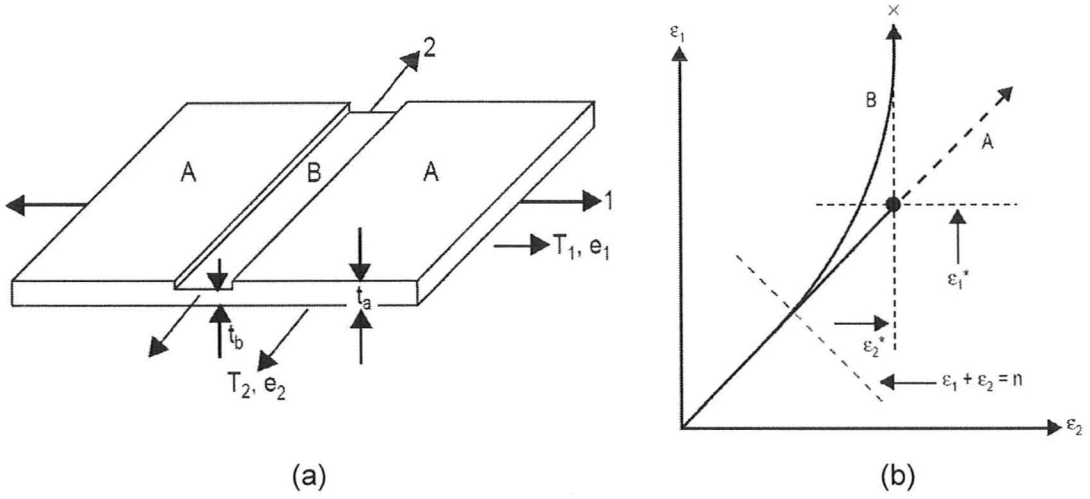

Figure 2-2 A schematic showing how strain in the defect (region B) departs from those outside the defect (region A). [26]

2.2 Microstructural Factors Affecting Strain Concentration

Strain localization could be explained through the understanding of vertex effect [27]. Vertices result in flow localization through an abrupt change in loading path from tension to shear. Vertices come from the yield surface with different features related to several factors:

a). Microstructural factors, including grains, defects and other materials heterogeneities, are important, complex and not fully understand yet.

b). Geometrical factors: size and geometry of tensile coupons, surface imperfection, cracks and so on. Strain concentration appears at the local minimum cross-section area.

c). Load parameters: strain path, rate (i.e. big capacity for strain energy dissipation at high strain rate[7]) and history (more homogeneous distribution of solutes and dislocations [28]).

d). Temperature

The effect of microstructure on the localization behavior was proposed at different scale: a) Grains: grain size, initial grain orientation and its spatial distribution and grain orientation evolution (i.e. geometric softening caused by lattice rotation [29]); b) Second-phase particles: their position and distribution; c) Dislocations: initial dislocation density and distribution, dislocation evolution (i.e. rapid dislocation multiplication with initial low mobile dislocation density, dislocation channeling through a dispersion of shearable obstacles; d) Solutes: their concentration and distribution; e), Microcavities and so on.

In addition, interaction between localized phenomena (interaction between PLC bands and necking[30-31], cooperative shears [32] et al) and work hardening (i.e. transient reduction in work hardening [32]) also affect the localization behavior.

2.2.1 Grains

The orientation effect on non-uniform deformation in ductile single crystals is still an open question. The appearance of shear bands is related to the orientation of single crystals of f.c.c metals as Al-Mg and Cu [33-34]: shear bands were observed with $(211)[\bar{1}11]$ copper orientation but not with $(011)[\bar{1}00]$ Goss orientation. Earlier experimental works [35-36] done on Al-Cu, Al-Zn, Al-Ag and

Cu-Be alloys showed that 'coarse slip bands' are similar in direction to the active slip system. On the other hand, experiments on other single crystals such as Al-Cu alloys showed that shear bands misorient with active slip planes at the beginning and progression of deformation, slip planes tend to appear along with shear bands. Later, Chang and Asaro [37] thought the lattice misorientation between macroscopic bands and the surrounding cause a geometric softening. However, geometric softening is limited to explain all bands structure, and then, latent hardening is introduced by other researchers [34].

In polycrystalline metal, the role of grains, including size, orientation and its spatial distribution is still not entirely clarified. Some possible grain-level mechanisms were summarized by Nesterenko [38], shown in Figure 2-3. Grain-size inhomogeneity is based on the Hall-Petch relationship: strength increases with decreasing grain size. A large number of experiments[39-40] were successfully set up to prove the Hall-Petch relationship at micron scale although cases become more complex at nanometer scale [41] and millimeter scale[42]. It is worth to mention for the sheets with coarse grains (< 20 layers of grains through thickness): strength decreases with decreasing the number of layers of grains, while strength increases with increasing grain size in specimens with one-layer grains. Experimental results on Cu, Al-4.8Mg and Al-1.8Cu alloys showed the increasing tendency for shear banding with increasing initial grain size.

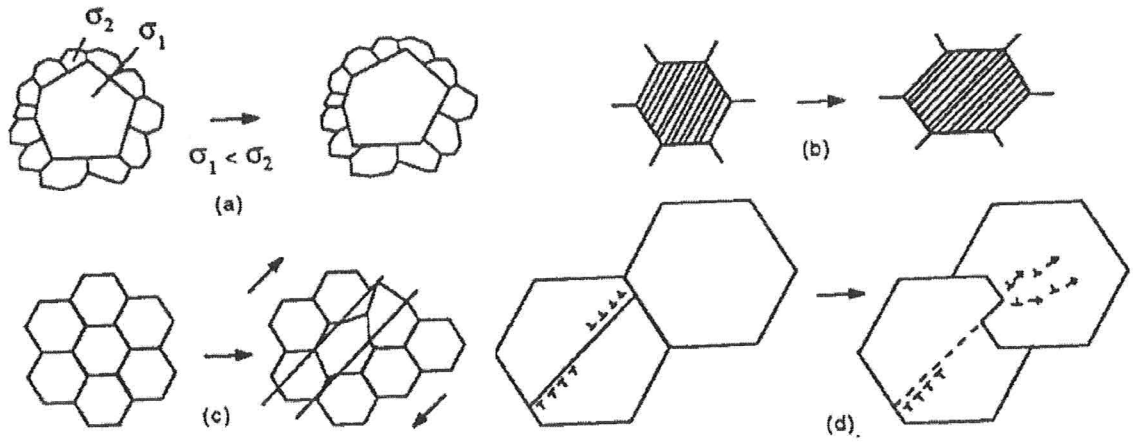

Figure 2-3 Shear band initiation mechanisms: (a) grain-size inhomogeneity; (b) geometrical softening; (c) Peirce-Asaro-Needleman textural localization and (d) dislocation pile-up release [38]

Geometrical softening mechanism requires lattice rotation during deformation. The deformation-caused evolution of grains is a widely acceptable idea; however, the evolution processes and paths of grains are still under study. Nevertheless experiments were done on the evolution of individual grains. Margulies and Winther [43-44] used X-ray diffraction methods to trace the evolution paths of a single layer of grains, shown as hollow circles and squares in Figure 2-4. Tatschl [45] through insitu tensile testing got the evolution paths of surface grains, shown in circle in Figure 2-4. Although these paths are not full consistent, grains with <0 1 1> axis are general toward to <0 0 1>-<1 1 1> line.

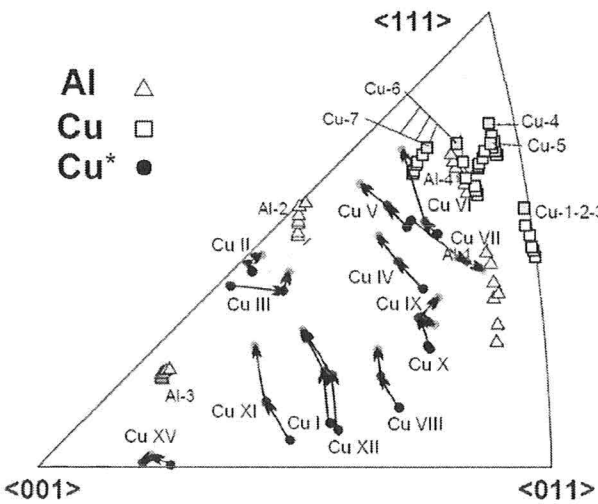

Figure 2-4 Tensile direction evolution paths of 4 aluminum grains and 7 copper grains

Note: The grey symbols indicate the final stage

Since no direct experimental results were presented to trace the evolution paths of bulk grains models for these behaviors are proved to be extremely useful. The evolution path strongly depends on the stress or strain tensor assumption of individual grains in different models [46]. (Figure 2-5) In the models of Sachs, each grain behaves like a single crystal. In Taylor-based and Mao's models, <111> and <001> are the final directions.

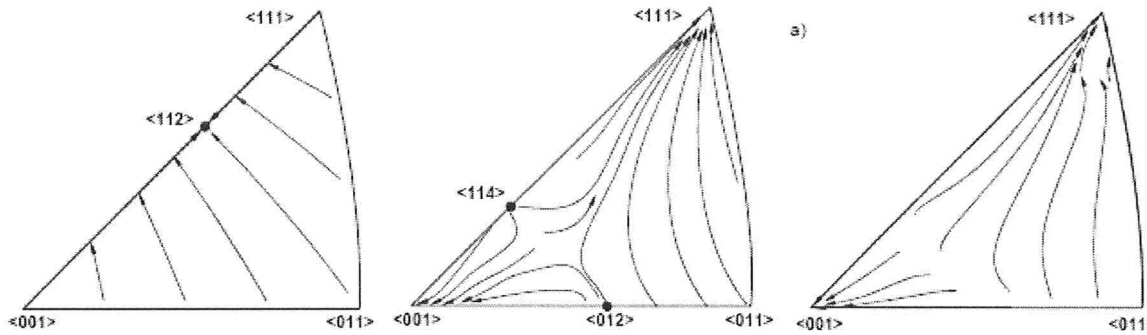

(a) Sachs assumption (b) Taylor assumption (c) Mao assumption

Figure 2-5 Tensile direction evolution predicted by different models[46]

Orientation changes could partly explain the angle of shear bands. Shen[47] analyzed the crystallographic nature of 35° shear bands which are rooted in the non-homogeneous transition from copper and brass-type texture to Goss-type texture. Goss oriented grains lead to the 35° shear band due to their easily deformed nature and their orientation consistency. However, excessive trans-granular 35° shear bands were usually observed in Goss oriented grains. Moreover, EBSD scanning [7] indicated that main texture components remain the same as no observable difference for the bulk materials was noticed although surface grains have more a randomly texture compared to the initial state.

Texture localization and dislocation pile-up release are caused by the co-deformation of adjacent grains in which the key is the interaction between grains. Franciosi and Zaoui [48-49] experimentally studied relative values of the interaction coefficient between the 12 slip systems in f.c.c crystals according to

dislocation theories. Their results revealed that the order of the interaction coefficient between slip systems of adjacent grains from the smallest to largest is the following: a). when they are the same; b). when they form Hirth lock and co-planar junctions; c) when they form glissile junctions and d) when they form sessile Lomer-Cottrell lock. Havner[50] provided a general approach for determining probable active slip systems and their slip rates, which are not full agree with Franciosi's conclusion. Zaefferer's results [51] revealed that even a small-angle grain boundary could effectively impede the dislocation.

These four mechanisms were built on statistical experimental results and slip theories with a crystallographic nature. However, how slip forms the crystallographic and non-crystallographic type micro-bands and finally leads to macro shear bands is still not fully understood. Therefore, direct experimental evidences of heterogeneous deformation for materials with real microstructure are urgently needed.

Wright[52] found that local stress concentration favors grains with low Taylor factors over grains with high Taylor factors. Lee and Chan [53] simulated that shear band forming is not only sensitive to texture variation but also the alignment of texture colonies. Wu's simulation [54] gave a similar conclusion: texture profiles usually indicate heterogeneous deformation. On the other hand, experiments on polycrystalline materials [55-57] conclusively demonstrated the non-crystalline nature of shear bands showing that shear bands run through grains without derivation considering the misorientation of grains.

With new techniques for measuring local displacement and local orientation, experiments on oligocrystal materials (i.e. samples with one-layer grains with millimeter size) have focused attention on grain-level inhomogeneities[58-60] Raabe[58] provided detailed strain mapping under compression and proved that macroscopic boundary conditions and grain interaction work together to enlarge heterogeneities. Zhang and Tong [60]

described that aluminum multi-crystals favor easy slip transmission and accommodation among grains. Zhao and Raabe [59] recently suggested that grain topology (i.e. the geometry of grain boundaries) and micro-texture play an important role in strain heterogeneities. However, the story of grain-level inhomogeneities effect on strain concentration still lacks some chapters.

2.2.2 Second-phase Particles and Voids

Second-phase particles, specifically their spatial distribution, play an important role on the heterogeneous deformation in AA5754 alloys. Research done on tensile[61], shear[31] and bending[62] tests reached the following conclusions: DC sheets are more stable during the post-localized necking process as compared to CC sheets. Second-phase particles seem to be the most likely microstructure reason for such difference: three time higher stringer density in CC sheets than in DC sheets with similar volume fraction at 0.21wt.% Fe level, and particles with slightly larger aspect ratio and subtle high overall volume fraction in CC sheets[63]. Little damage is displayed just before facture [64] and no damage is seen just underneath the facture surface[31] in such AA5754 alloys. This implies that particles actually affect the forming and developing of shear bands and not only act as nucleation sites of damage.

Void nucleation and growth could interact with flow localization to promote the early onset of plastic instability. Void profusion[27] promotes plastic instability even if the essential reason is local strain concentration, and the effect of void increases with decreasing strain rate sensitivity. For steel, voids usually appear before shear bands. In strain-rate-sensitive materials as aluminum alloys, shear localization precedes the detectable damage nucleation and only facture surface is dominated by the void sheeting.

In conclusion, second-phase particles affect the strain concentration process.

2.2.3 Interaction between Localized Phenomena

Lüders fronts are a type of inhomogeneous deformation and may lead to local soft areas[65] which appear in Al-Mg systems with a small grain size (i.e.<30μm) due to static strain aging[66]. At a certain temperature, DSA takes over as Lüders is complete and this transition is known as the PLC effect.

Diffuse necking band usually nucleates at PLC bands although no observable interaction between PLC bands and all other features related to tensile instability is shown in Figure 2-6. Kang et al [7] treated PLC bands as a geometric imperfection using the M-K method and obtained experimental global strain at necking through PLC bands strain which proves that the presence of PLC bands is responsible for the early onset of diffuse necking.

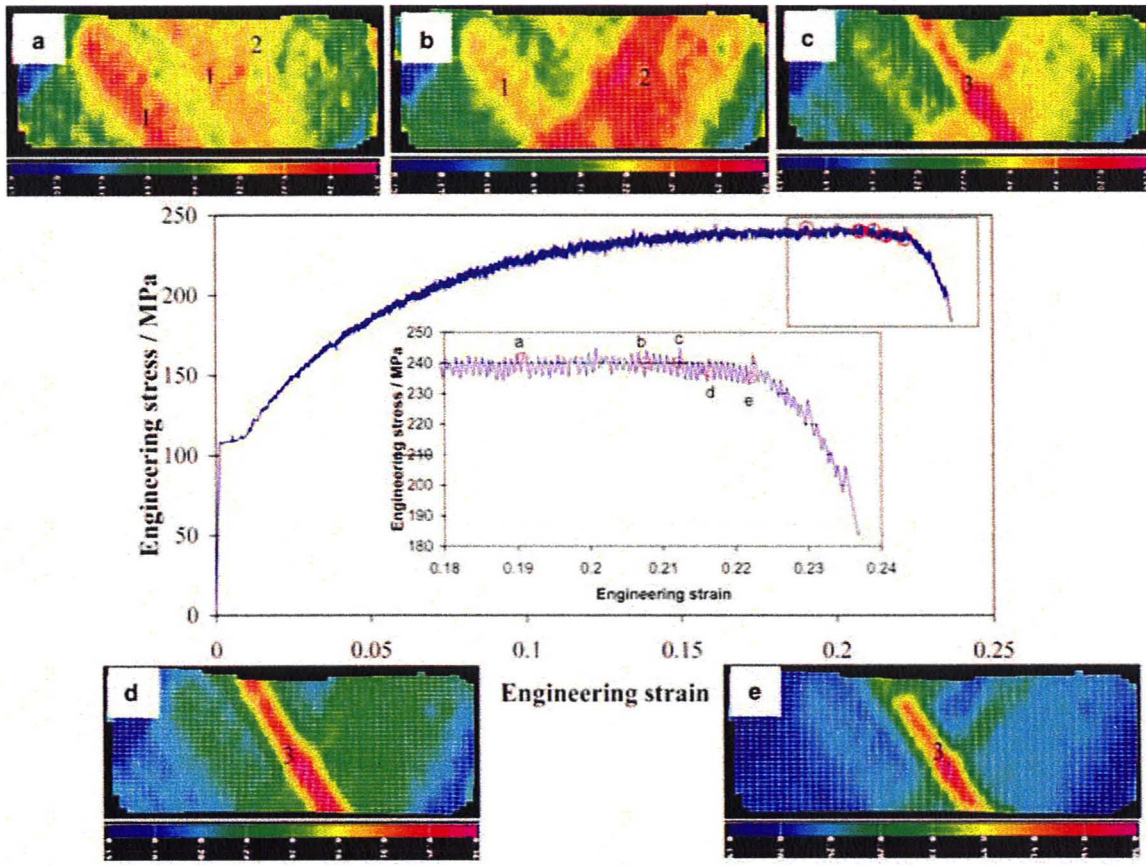

Figure 2-6. Tensile deformation sequence [7]

Note: 1, 2 and 3 stands for the PLC bands, Diffuse necking band and Localized necking bands

Chung et al[67] thought that the PLC effect creates conditions for strain localization and reduces the stress requirement for void growth in shear bands. However, Halim et al[28] observed that shear bands form on a conjugate plane rather than the same plane of PLC bands.

To clarify the interaction between PLC bands and shear bands after diffuse neck, two-steps experiments were set up to isolate the primal interaction of PLC bands and necking bands by Kang et al [68]: first, samples were deformed to the diffuse neck or localized neck position without PLC effect at low temperature and deformed again at room temperature to observe the interplay of

PLC bands and shear bands. They concluded that PLC bands provide nucleation sites for shear bands, and probably are the reason for the only one localized necking band which appears between the conjugated set of shear bands.

Deformation-causing roughening could be a possible explanation for the interaction. Surface roughening is associated to texture profiles [69], strain hardening [70] etc.

To sum up, the existence of PLC bands shortens uniform deformation regions by providing nuclei of diffuse localization and is therefore strongly related to shear bands. Experimental results on single crystals and polycrystals revealed that shear bands favor forming inside of diffuse necking bands. Therefore, different heterogeneous deformation processes are in fact strongly associated with each other.

2.3 Microstructure-based Simulation Predicting Strain Concentration

Numerous models were built to describe the strain localization processes. Bifurcation theories such as J_2 corner theory [71] introduce yield surface vertex effects. Imperfection analysis considers the softening effect due to initial defects, which has the advantage to predict the position of localization.

With the help of finite elemental methods, it is possible to simulate strain concentration caused by heterogeneous microstructure especially grain-level inhomogeneities. We first summarize these polycrystal plasticity models, and then focus on the development of microstructure-based models: CPFEM and FE-TBH. Some simulation results are proposed at the end of this section.

2.3.1 Polycrystal Plasticity Models

Starting from the 20th century, many polycrystal plasticity models were developed to reveal the nature of plastic deformation. According to the different deformation assumptions of individual grains in different models, six kinds of models were proposed [72-73]: (a) 'no constraints' model ; (b), 'full constraints' model; (c), 'relaxed constraints' model; (d), self-constraint model, (e), multi-grain model and (f) full crystal plasticity finite-element model (CPFEM).

Sachs model (1928) is called the 'no constraints' model, with the assumption that individual grains undergo the same stress. In this model, activated slip system(s) inside different grains is the one which has reached critical resolved shear stress, which implies that each grain deforms like a single crystal. However, the necessary strain compatibility between grains is not considered.

The Taylor model (1938) is the 'full constraints' model. In this model, individual grains experience the same strain as the macroscopic strain of the entire specimen. Five independent slip systems are required to fulfill the constraints for each grain. Additional energy assumptions are required to identify the active slip systems. In 1951, Bishop and Hill gave an advanced interpretation of Taylor's assumption though the concept of yield locus. Therefore, the Taylor model and the Bishop-Hill model are often called by a single name: the Taylor-Bishop-Hill model. However, this model maximizes the effect of the geometrical constraints and could not provide clear explanation on the different stress tensors for adjacent grains.

To overcome the strain incompatibility of Sach's model and the stress incompatibility of Taylor's model, 'relaxed constraints' models were built; however, none of them were completely successful. Kochendorfer(1941) modified Sach's model to include complex multiple slip systems which are activated near the

grain boundaries. Leffers (1968) introduced the effect of reaction stress among grains. Several further modifications were done recently on the description of reaction stress, including normal reaction stress [72] and shear reaction stress[46, 74].

The 'relaxed constraints' approaches of both Taylor-type and Bishop-Hill type framework are exactly equivalent [75]. A constraint for the corresponding stress component is added in Bishop-Hill type model, while frictional stress is introduced in Taylor theory. As the local strain components are not needed to be the same for different grains, less slip systems are needed to achieve compatibility. Although introducing relaxed constraints provides better stress equilibrium at grain boundaries, there are some theoretical shortcomings in these models. They are not completely successful for any kind of deformation mode, lack the description for prescribed deformation, and assume the value of relaxation shear rates.

To avoid the complex description of the interaction between neighboring grains in polycrystalline form, self-consistent models assumed other interaction instead of grain interaction[75]. Usually, they are based on a single crystal embedded in a polycrystal matrix. These models are much more complicated than Taylor models.

Compared to experimental results, the results predicted from 'relaxed constraints' models are still not better than those from Taylor model. Therefore, multi-grain models provide another way to consider grain interaction[73]. In this model, Taylor condition is assumed to be maintained at the boundaries of the cluster. Different multi-grain models have different assumptions of the size and shape of cluster, as well as how many grains are in one cluster.

The ultimate multi-grain model is actually the full plasticity finite element model (CPFEM). The models above only consider statistical texture; however,

CPFEM provides a computational framework capable of real microstructure stress and strain compatibility between grains.

2.3.2 Microstructure-based Finite Element Models

Based on calculating slip rate of each slip system, so far crystal plasticity models have the best description for grain-level inhomogeneities. However, most published crystal plasticity models are time consuming at the specimen scale.

To reduce the calculation time, two basic ideas were developed by Hu et al[76]. The first deals with improving the method of calculating slip rate while the second uses grains instead of slip systems as a calculating unit. Generally speaking, the first called CP-FEM, is based on Huang's code[77] and is double the speed of the original programs. The second model, named FE-TBH, has three times the speed.

The modifications and advantages of CP-FEM are listed as follows. ABAQUS explicit code was developed to replace the original implicit ABAQUS code, which allows for a fast calculating speed at specimen size, includes dynamic effect and provides a good link with damage. Eulerian integration instead of tangent modulus method is used to support the large calculating speed.

In FE-TBH, the behavior of isotropic materials of different grain orientations is modified by the Taylor factor. Taylor factors are generally used to represent the 'hardness' of special oriented grains. Taylor factor M_g, which is defined as the increase in total shear per unit macroscopic strain, is a function of strain mode and orientation. For aluminum, under the condition that each slip system has the same critical resolved shear stress, the defining equation becomes E2-4.

$$M_g = \frac{\Sigma \left| \dot{\gamma}^{\alpha} \right|}{\dot{\varepsilon}^{p}} \qquad \text{E2-4}$$

where $\dot{\gamma}^{\alpha}$ and $\dot{\varepsilon}^{p}$ are the slip rate of each activated slip system and the applied macroscopic strain respectively. The modification factor is called the relative Taylor factor R_g, which is Taylor factor of a special grain M_g divide the average Taylor factor M.

$$R_g = \frac{M_g}{\bar{M}} \qquad \text{E2-5}$$

Therefore, flow stress in a given grain is defined by the multiplication of stress σ_0 by relative Taylor factor R_g.

$$\sigma_g = R_g \cdot \sigma_0 \qquad \text{E2-6}$$

Microstructure evolution is based on the same idea as the Taylor-Bishop-Hill (TBH) model for full crystal plasticity. TBH model rotates grains and tries to keep the same direction between macro and slip deformation directions. Then, we obtain the evolution of relative Taylor factor.

2.3.3 Simulation Results

To magnify the grain-level inhomogeneities to the level that is easy to observe and simulate, experiments and simulation on oligocrystal have been given more attention [58-60, 78-79]. Delaire [78] used the finite element crystal plasticity model to describe strain localization under uniaxial tension and trace the history of slip system activation. Raabe's [58] simulation proved that both the macroscopic boundary conditions and grain interaction work together enhancing heterogeneities. Zhang and Tong [60] described that aluminum multi-crystals favor easy slip transmission and accommodation among grains. Cheong and Busso [79] reviewed that in-grain misorientation influences strain-hardening behavior under uniaxial tension. Zhao and Raabe [59] recently suggested that grain topology (i.e. the geometry of grain boundaries) and micro-texture play an important role in strain heterogeneities.

All the above simulations are based only on tens of grains and as a result the heterogeneous deformation strongly depends on one or two grains. Hu[76] simulated a two-dimensional structure with hundreds of grains as shown in Figure 2-7(a)-(c). Simulation results show that the localization bands form due to the grain-level structure. With special particle distribution, localization paths are generally the same but little different details, shown in Figure 2-7(d)-(f),

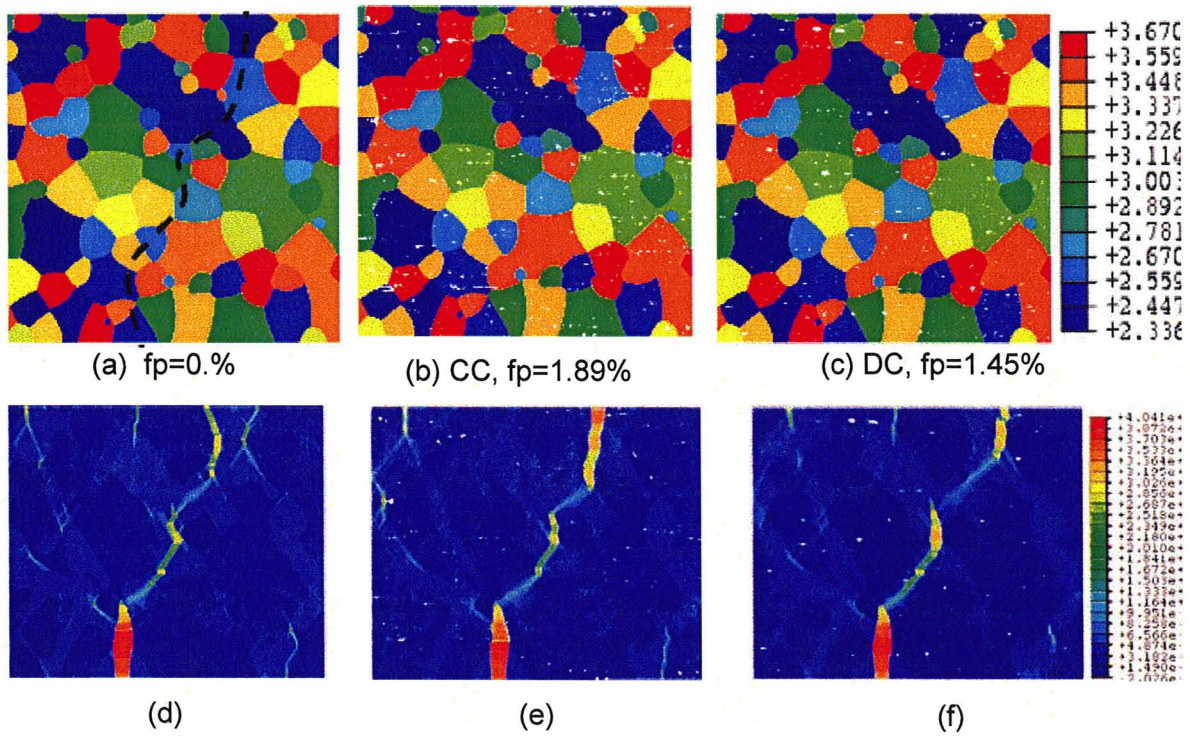

(a) fp=0.% (b) CC, fp=1.89% (c) DC, fp=1.45%

(d) (e) (f)

Figure 2-7 Contour plots of the Taylore factors of the grains with different cases (a)-(c) and their corresponding contour plots of ε_{11} distribution (d)-(f)[76]

2.3.4 Limitation of 2D Models

Simulation results from these 2D models overestimate the influence of grain-level inhomogeneities. Wilson's [80] work showed that localization strain gradually grows with increasing number of grains along the thickness direction when the number of grains is less than 30. A similar conclusion was reached in

Hu et al's [81] simulation. The tendency of necking becomes easier and the necking strain decreases with increasing the number of layers of grains.

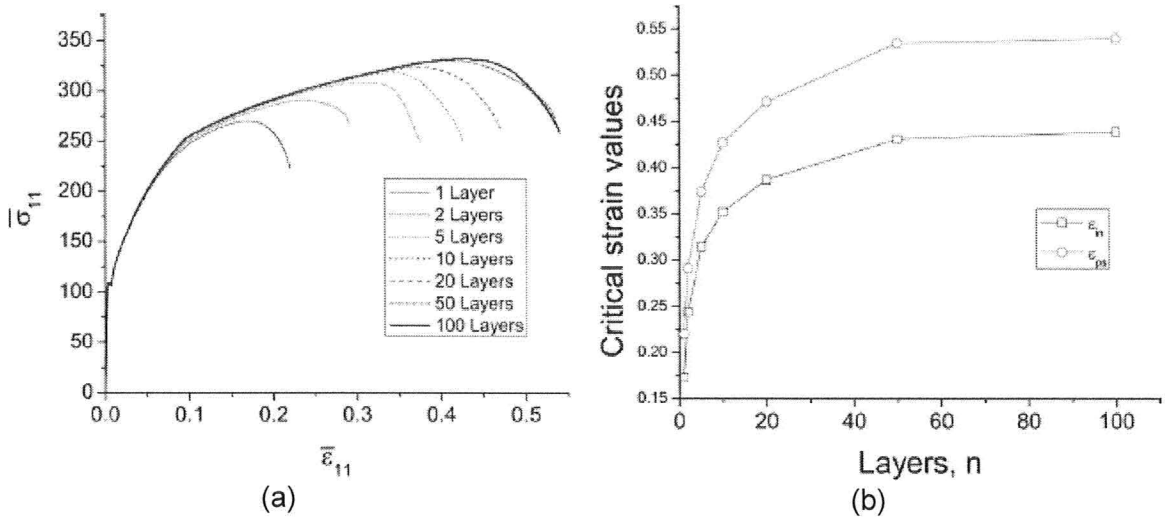

Figure 2-8 (a) The stress-strain curve of the models with Taylor factor of each element is an average of n orientations and (b) the variation of critical strain values with n [81]

Not only grains but also particles are in the same situation during all the 2D simulations. Particles which are treated as going through specimens and penetrating particles probably lead to earlier onset of localization and fracture [82-83].

2.4 Critical Comments

Auto body sheet materials produced from AA5754 alloys usually fail in the form of strain localization. Therefore, microstructural effects on strain localization have recently been attracting a great deal of interest, however even with all the recent interest, they are not fully understood. Experimental and simulated results proved that grain-level structure dominates over sub-grain level inhomogeneities for the localization path. However, there are still gaps in the story of how grains affect deformation.

Intelligent-operating procedures require precise models to describe and predict sheet deformation. Most microstructure-based models do catch some features of deformation however they are extremely time consuming and rapid models are required. Although such rapid models are possible, in order to become so fast they make a great deal of simplifications and so experiments are needed to calibrate them.

In this current thesis, we design experiments on specimens with known microstructure under the deformation with enough time and space to show the grain level inhomogeneities. Our interests focus on the effect of grain interaction on strain localization and the precision of our fast-calculating models.

Thermal-mechanical treatment (annealing after small pre-deformation by cold rolling) was used to get coarse-grained samples. The obtained microstructure should be simple enough for characterization and simulation and complex enough to show grain-level inhomogeneities. Mechanical tests were run on the coarse-grained samples to test the deformation behaviors of individual grains and to compare with the simulation results from models.

CHAPTER THREE

EXPERIMENTAL PROCEDURES

The literature review chapter points out a complex interrelationship between microstructural, geometrical and loading factors with deformation heterogeneities. Isolating each factor and studying their independence effect requires good experimental designs and a proper choice of techniques. This chapter reviews the experimental techniques and methods used in the current work. We first review the general chemical composition and microstructure of the as-received materials and follow with the development methods of coarse-grained sheets. Then, we introduce the sample preparation process and the techniques for characterization. We focus on the techniques to get reliable EBSD data for large scanning area. After that, we enter the mechanical test part. Uniaxial tensile test combined with Aramis is the general route in this research.

3.1 MATERIALS

The present thesis is focused on DC AA5754 with 0.21% Fe composition. The as-received materials are supplied in the form of rolled sheets (1mm thick) produced by cold rolling and then subjected to O-temper (i.e. annealed at 450°C for 2 hrs).

3.1.1 Chemical Composition and Microstructure

Chemical composition of the as-received materials is shown in Table 3-1.

Table 3-1 Chemical composition of DC AA 5754 sheet materials (in wt.%) [4]

Mg	Mn	Si	Fe	Cr	Ni	Cu	V	Zn	Al
3.11	0.25	0.11	0.21	0.04	0.01	0.01	0.01	0.02	Balance

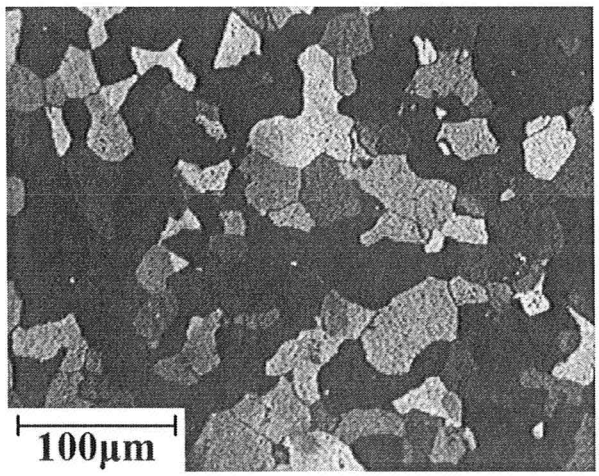

(a) Grain structure

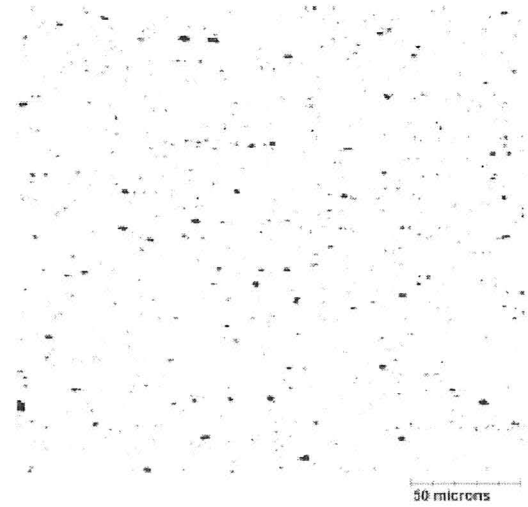

(b) Particles distribution [4]

Figure 3-1 Microstructures of as-received materials: (a) grain structure under polarized light; (b) particle distribution

The grain structure is near equiaxial (Figure 3-1(a)) with an average grain size around 25 microns. Moreover, a random second-phase particle distribution

is seen in this material (Figure 3-1(b)). Most particles were identified as Fe-rich particles [4].

3.1.2 Thermal-mechanical Treatment

In order to produce coarse-grained samples, thermal-mechanical treatment was used in this thesis. The general route was annealing after cold rolling.

As the critical deformation for recrystallization of pure aluminum is around 2-3%[84], pre-deformation of as-received samples was designed in range of 4%-15% thickness reduction. However, deformation precision is limited by the rolling procedure used, which is about ±1%. Given small gauge area of tensile coupons, the effect of non-uniform rolling strain becomes much smaller on the distribution of grain size.

In order to control the grain size, temperature and holding time were carefully examined. The temperature and time is set to obtain full recrystallization and dissolution of large Mg-rich particles. Rolled sheets (7.6 by 10.2 by 0.85-0.96 mm) were heated at 575°C for 3 hours in salt pots and then quenched in water.

3.2 Sample Preparation for Characterization

3.2.1 Machining, Cutting and Mounting

Small rectangular pieces were cut from the as-received and heat-treated sheets using a shearing machine. Samples were mounted in white Lucite for general microstructure characterization. Holes were drilled at the back side of mounted pieces to make electrical conduction for electrical etching.

Tensile bars were machined using Electro Discharge Machining (EDM) to ensure high dimensional precision and minimum surface damage. Tensile bars were glued on to a special stainless steel sample holder designed to attach to the sample holder within the Struers Automatic Polisher (Figure 3-2). Glue must be uniform on surface to ensure even thickness during grinding and polishing.

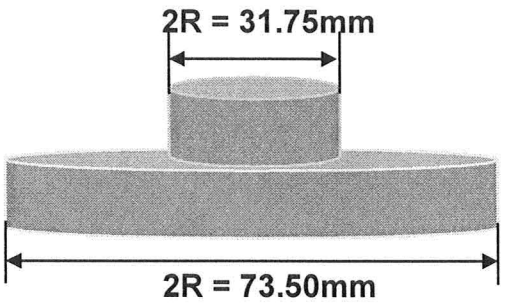

Figure 3-2 Schematic drawing of sample holder

3.2.2 Metallographic Preparation

Grinding and polishing are the general routes to prepare samples for optical metallograpgy, SEM and Electron Backscattered Diffraction (EBSD) in order to avoid the effects of initial surface roughness for tensile tests. Removal of at least 100 microns by grinding for all samples was necessary for the samples to be free of surface effects. Since our materials had comparably good initial surface roughness, 1200 sand paper was selected for the first grinding step for 1 min. Following steps were around 1 min with fine sand paper grinding and 5 min with 3 micron and 1 micron diamond paste polishing. 0.05 microns colloidal silica suspension (OPS) was used as the last step of polishing, 5 min for optical observation and 10 min for EBSD. The colloidal silica not only removed the residual strain layer on the sample surface but also had a slight etching effect to get better Kikuchi patterns.

3.2.3 Etching

Barker's reagent was used for electrical etching to reveal grain structure under polarizing light. When etching 5xxx series aluminum materials, the

specimen was the anode and stainless steel was used as the cathode. Specimens were anodized for 50-70 seconds at 20V.

Table 3-2 Etching solutions and their composition

Reagent	Composition
Barker's	48-50% HBF_4 (conc.)15ml+H_2O(distilled) 90ml
Poulton's	HF(conc.)10ml+HCl(conc.)15ml+HNO_3 25ml+H_2O(distilled)50ml

Poulton's reagent is used to directly reveal grain structure for coarse-grained materials but with large etching depth. With revealed grain structure, we could observe the deformation morphology of grains.

0.5%HF (HF(conc.) 0.5ml + H2O(distilled) 100ml) was used to improve the quality of Kikuchi patterns for EBSD. Sample was immerged in 0.5%HF solution for 20s.

3.3 Characterization Techniques

3.3.1 Optical Microscopy

Optical observation was carried out using the Axioplane2 Imaging System equipped with a Zeiss Optical Microscope as well as North Eclipse v6.0 imaging software under polarizing light. The linear intercept method was used to measure the grain size on the stitched images to ensure sufficient numbers of grains (i.e. 20) across each line. Six lines (four edges and two diagonal lines of a square) were drawn on each stitched image.

A Nikon AZ 100 Stereoscope with Nis-Elements BR 3.0 was used to obtain images of the fractured surface-, top- and thickness-view. Slip trace characterization and facture strain calculation are based on these digital images.

To avoid the effect of surface roughness a RealTime EDF (Extended Depth of Focus) program was used to obtain focused surface morphology images. RealTime EDF is designed to get a series of digital images from a number of auto-captured original images with deferent focal distances.

True fracture strain ε_f and true fracture stress σ_f in the uniaxial tensile tests were calculated as follows.

$$\varepsilon_f = \ln\left(A_0 / A_f\right) \qquad \text{E3-1(a)}$$

$$\sigma_f = L_f / A_f \qquad \text{E3-1(b)}$$

Where, A_0 is the initial cross-sectional area of the gauge portion, A_f is the projected area of a fracture surface and L_f is the load at fracture.

3.3.2 Electron Backscattered Diffraction

Electron Backscattered Diffraction (EBSD) or backscattered Kikuchi diffraction (BKD) is a microstructural-crystallographic technique. A polished specimen is placed into position with a 70° tilt with regard to the normal axis of the diffraction camera. In this project, Kikuchi patterns are collected and indexed using EDAX-TSL OIM Analysis attached to a LEO Scanning Electron Microscope (Carl Zeiss SMT Inc. Peabody, MA) at the General Motor Research & Development Center, Warren, MI.

Maps of Euler angle, inverse pole figure (IPF) and misorientation were processed to detail grain orientation distributions. Euler angle maps display different colors for different orientations by assigning different colors to each Euler angle. Misorientation maps present the misangle of grain boundaries. IPFs allow the crystal orientation to be presented relative to sample coordinates.

In IPF colored maps, symmetric orientations of the f.c.c lattice which have the same mechanical properties are displayed in the same color as shown in Figure 3-3. Furthermore, IPF colouring maps of the tensile axis index Taylor factors for different orientations. Based on Taylor factors, in IPF colouring maps, green and blue grains mean hard while red grains mean soft.

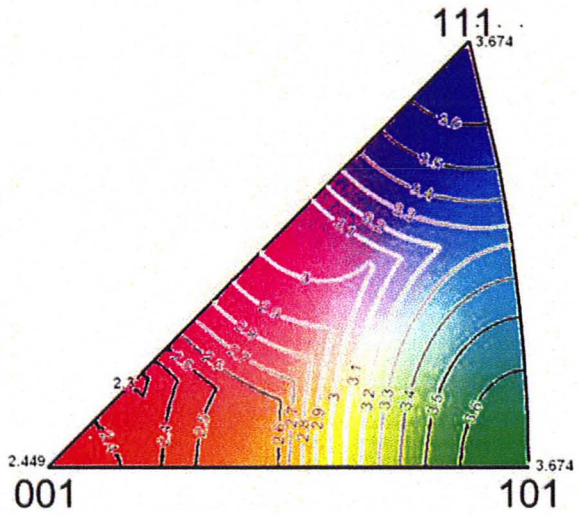

Figure 3-3 The IPF colouring scheme for EBSD mapping

Note: Taylor Factors were calculated from TSL software.

Ideally the distribution of grain orientation should be described based on grains. However, in TSL software, IPFs are based on each EBSD data point which leads to no difference for a fine grain structure. Orientation scattering for a single grain forms the misleading appearance of IPFs, which is not true when only tens or hundreds of grains from 'Beam Scan' for large area are analyzed (Figure3-4 (a)). Therefore, IPFs for coarse-grained samples presented in this thesis are based on grains and the size of spots in these IPFs stands for the comparable size of grains in one diagram (Figure 3-4 (b)).

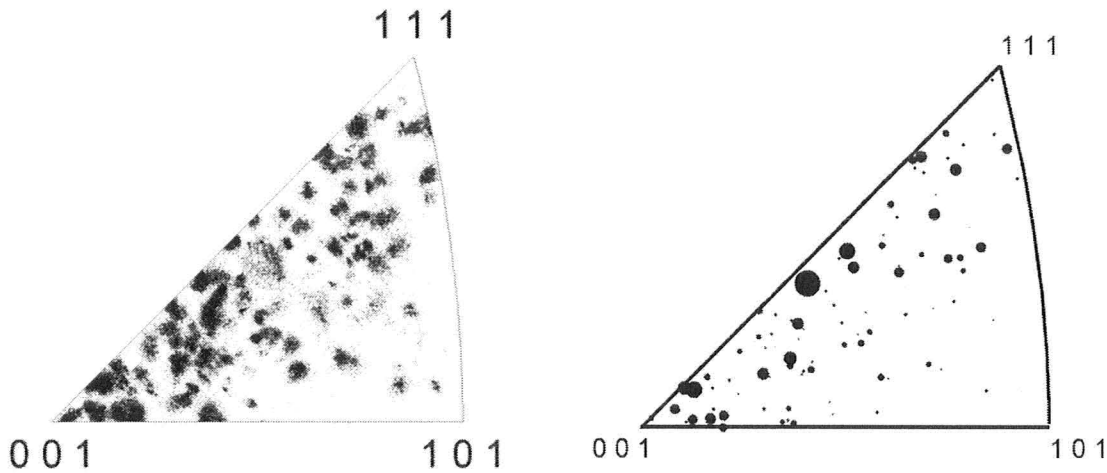

(a) from TSL software (b) after modification

Figure 3-4 IPFs of Normal axis

Note: The methods for modification are listed in Appendix.1.

Holding specimens is a problem for large area EBSD scanning. Specimens must have a flat surface and have good support to diminish the stress caused by its own weight when tilting 70°. Therefore, specimens were not only glued on the sample holder but also supported by the special buttresses shown in Figure 3-5.

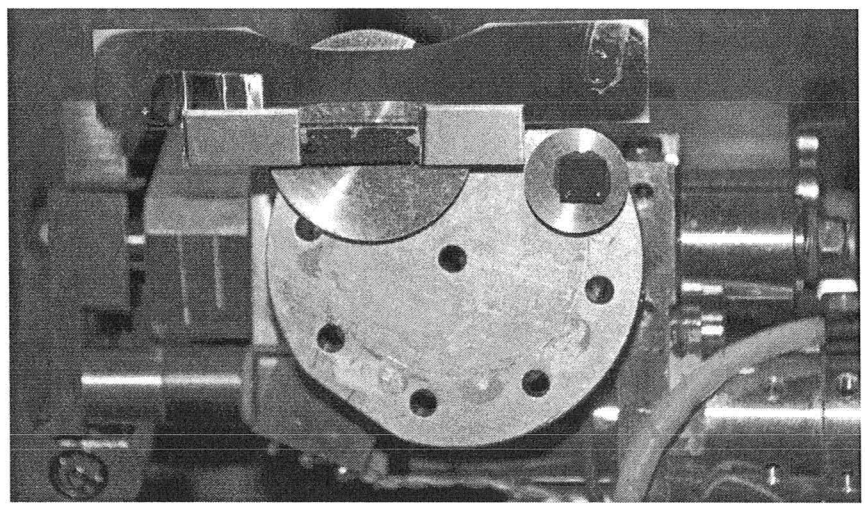

Figure 3-5 Specimen holding for EBSD

The strategy for large area EBSD scanning is to divide the total area into several parts and run 'Beam Scan' for each of them to avoid the image and orientation distortion problems when running 'Beam Scan' for large area. The total scanning time is limited by the movement of the stage to a new scanning position. The number of 'Beam Scan' required is determined by magnification. Therefore, magnification and scan step were carefully chosen to obtain good EBSD data within reasonable scanning time. A set of set-up scanning were run to find the best parameters.

Effect of Magnification was summarized in Figure 3-6. A few data points were different for the slight different position of scanning. Comparing the different grain orientations at 35X and 100X, misorientation between those two was less than 1°. Therefore, our EBSD scans were done at 35X with 15 microns step size to save time.

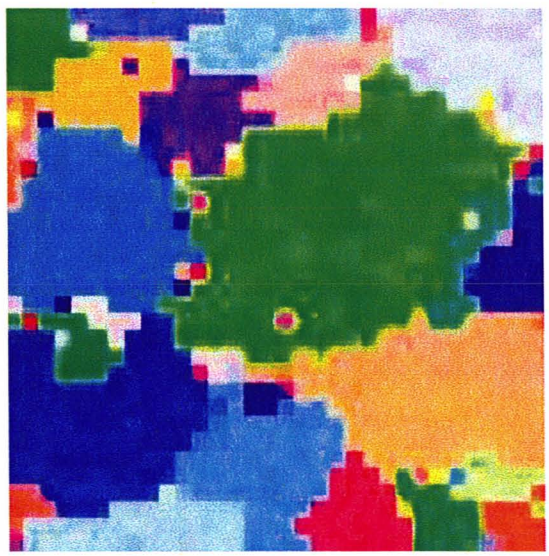

(a)35X, tensile direction

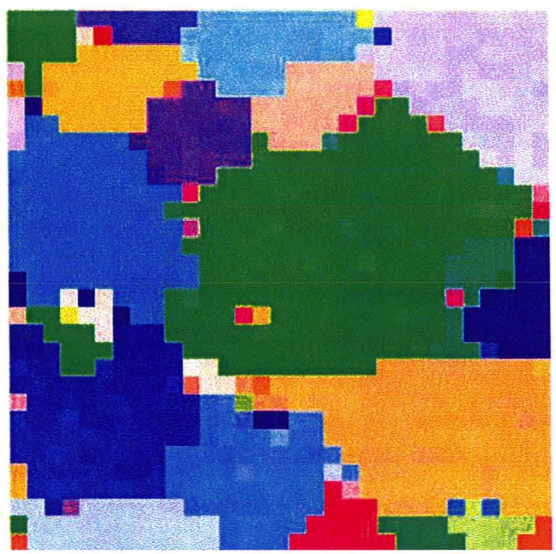

(b) 100X, tensile direction

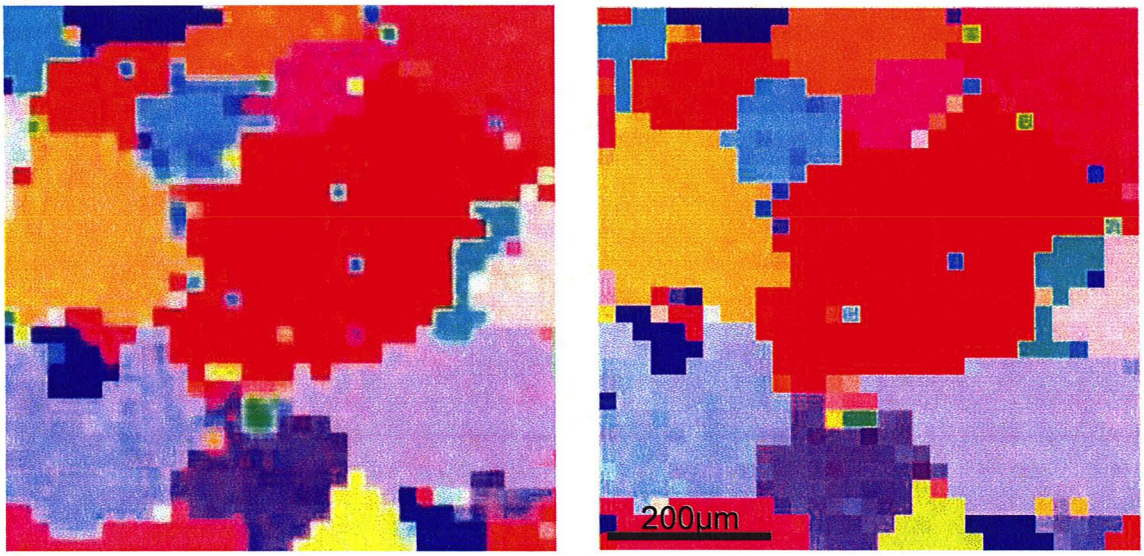

(c) 35X, normal direction (d) 100X, normal direction

Figure 3-6 Effect of Magnification:

(a) and (c), IPF mapping at 35X for tensile direction and normal direction, separately. (b) and (d), IPF mapping at 100X for tensile direction and normal direction, separately.

A set of methods were developed to reduce orientation distortion of edge grains in each scan at low magnification. The misorientation angle between grains in the overlap region of the two scans was probably over 5° due to the curvature of the electrical beam. Calculating mean orientation of grains inside overlapping regions between the two scan reduces experimental error caused by the horizontal or vertical curvature of electrical beams. Based on this, A Matlab program was developed to modify the orientation of edge grain for reliable EBSD data. The experimental error is about 2° after such modifications. Addtionally, all the IPFs and IPF maps in this thesis except Figure 3-4(a) were drawn by the program. Details on the algorithm of the program are shown in Appendix 1.

The quality of EBSD data points were reduced with increasing plastic deformation strain. TSL software defined the confidence index (CI) to describe the quality of indexing Kikuchi patterns. CI > 0.1 means at least 95% accuracy

rate to get the true orientation. Therefore, CI=0.1 was set as the criterion for selecting valid EBSD data of deformed structure.

3.4 Uniaxial Tensile Testing

Tensile tests were performed on a screw-driven tensile machine, Instron 5566. Uniaxial tensile tests were run at a 1mm/min strain rate which provided enough time to show the microstructure inhomogeneities and record the deformation process. Tensile direction was designed as the pre-rolling direction before recrystallization for all tensile bars.

To obtain tensile properties of the coarse-grained structure, flat tensile bars were prepared according to ASTM E 8M-04 (Figure 3-7(a)). A large transition radius is needed to ensure necking within the gauge length. A 12.5 mm gauge length was designed for the standard extensometer. Strain was measured using a strain gauge with better resolution of bulk strain.

The gauge area reducing modification was done to in order to allow for in-situ tensile test in SEM and EBSD scanning (Figure 3-7(b) and (c)). A commercial available digital image correlation (DIC) system (Aramis) was used to follow the surface deformation pattern during tensile test for coupons with shape II and III.

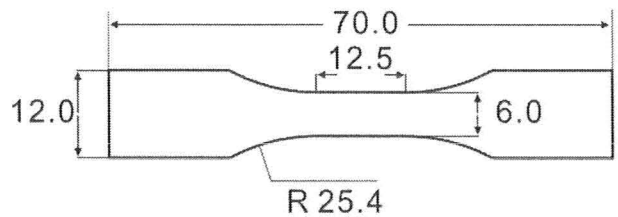

(a) Shape I

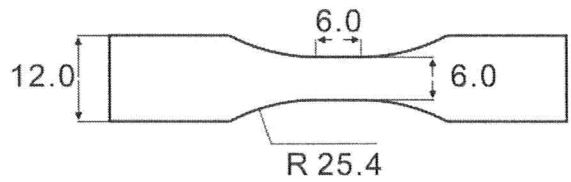

(b) Shape II

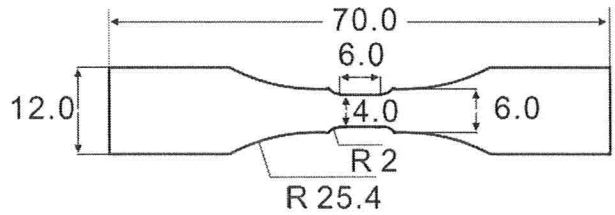

(c) Shape III

Figure 3-7 Dimension of samples

In-situ tension was run in a LEO Scanning Electron Microscope (Carl Zeiss SMT Inc. Peabody, MA) combined TSL with Delphi2 software with tensile stage. In-situ tensile process was controlled by the load, and elongation of bars between two chucks was recorded. The strain rate is 0.5 mm/min. Surface morphology was recorded during the In-situ test.

3.5 Digital Image Correlation

Digital image correlation is an optical non-contact surface strain measurement method based on a series of grey level images. Black and white inks are painted on the specimen surface to form the black and white random speckle pattern. A high-speed camera records the deformation processes at a certain time interval. Depicted in Figure 3-8, deformation is calculated based on the change in distribution of grey scale values of each facet (usually, a rectangular area) in the destination image when compared to the image preceding it. In the Aramis system, the area of interest is in the form of an array of facets in each deformation stages.

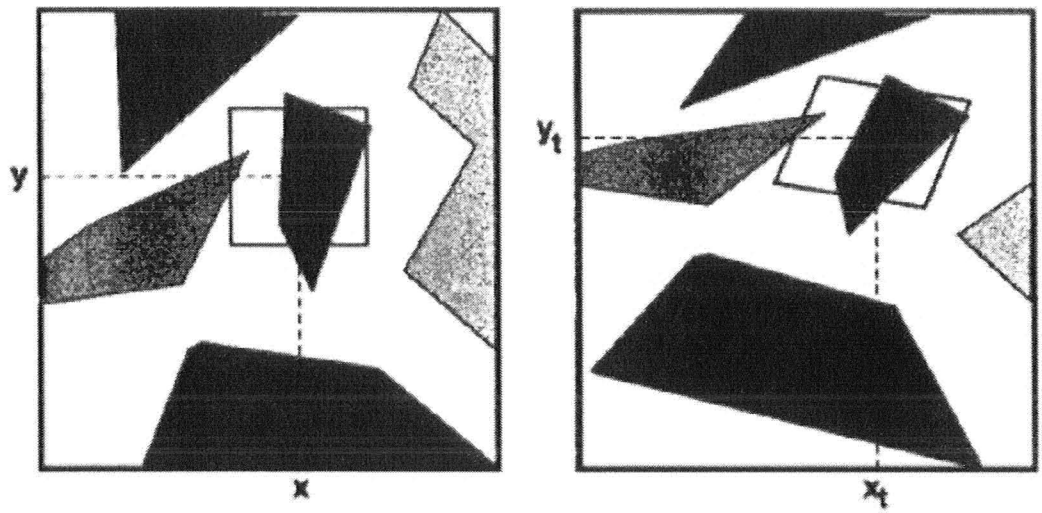

(a) initial facet (b) destination facet

Figure 3-8 Principle of digital image correlation with Aramis [85]

The grey values relationship between the initial and destination points represented by E3-2:

$$g_1(x,y) = g_2(x_t, y_t) \qquad \text{E3-2}$$

where, g1 and g2 are the initial and destination images and x and y are the coordinates on the image. The pixels in each calculated facet of the initial image are transformed to the ones of the destination image using the following transformation:

$$\begin{aligned} x_t &= a_1 + a_2 x + a_3 y + a_4 xy \\ y_t &= a_5 + a_6 x + a_7 y + a_8 xy \end{aligned} \qquad \text{E3-3}$$

in which, a_1 and a_5 describe the translation of the facet's center, a_2-a_8 stands for the rotation and deformation of the facet. A linear radiometric transformation is used to match two images in order to compensate different luminance between them:

$$g_1(x,y) = b_1 + b_2 g_2(x_t, y_t) \qquad \text{E3-4}$$

The criterion to choose a1-a8 and b1-b2 is to minimize the sum of the quadratic deviation of the matched grey values. Standard method used in DIC is the so-called cross-correlation in which a correlation coefficient C is defined as:

$$C = 1 - \frac{\sum (g_1(x,y) \cdot g_2(x_t, y_t))}{[\sum g_1^{\,2}(x,y) - \sum g_2^{\,2}(x_t, y_t)]^{1/2}} \qquad \text{E3-5}$$

Newton-Raphson method is used in Aramis to minimize the correlation coefficient C [85].

In this study, a two 2-dimensional technique was used to record the strain maps for both sides of the tensile samples. Step time was set as 0.5-1 frames/s. This step size gives reasonable numbers of images for strain calculation. A 7x5 facet/step size was used in the strain calculation, which is equivalent to a real dimension of 100-300 /80-200 μm.

CHAPTER FOUR

EXPERIMENTAL RESULTS

With experimental methods and techniques mentioned in chapter 3, experimental results will be presented and summarized in this chapter. First section will focus on the method of producing a coarse-grained structure and the relationship between pre-deformation ratio and grain size for our materials. Following, we focus on the characterization of initial microstructure, including EBSD mapping and second-phase particles. Then we switch to the results of mechanical tests, including the mechanical properties of specimens with different grain size and their strain mapping. This chapter will close with microstructure characterization during the deformation process.

4.1 Coarse-grained Structure

As mentioned in the previous chapter, we need coarse-grained specimens to run our mechanical tests and so we choose a thermal-mechanical treatment to get the expected coarse-grained microstructure. In this section, we first present the surface effect and then introduce typical microstructure under different pre-deformation ratio, finally summarize the relationship between recrystallization grain size and pre-deformation ratio.

4.1.1 Microstructure with Different Pre-deformation Ratio

After heat treatment, a thin layer of small grains exists near the sample surfaces (Figure 4-1). The thickness of this layer is about 100μm. This has then been ground during the sample preparation. Approximately two layers of homogeneous bulk discoid grains make up the recrystallization structure of samples with grain size larger than 600μm. There can be a small number of grains between the top and bottom layers.

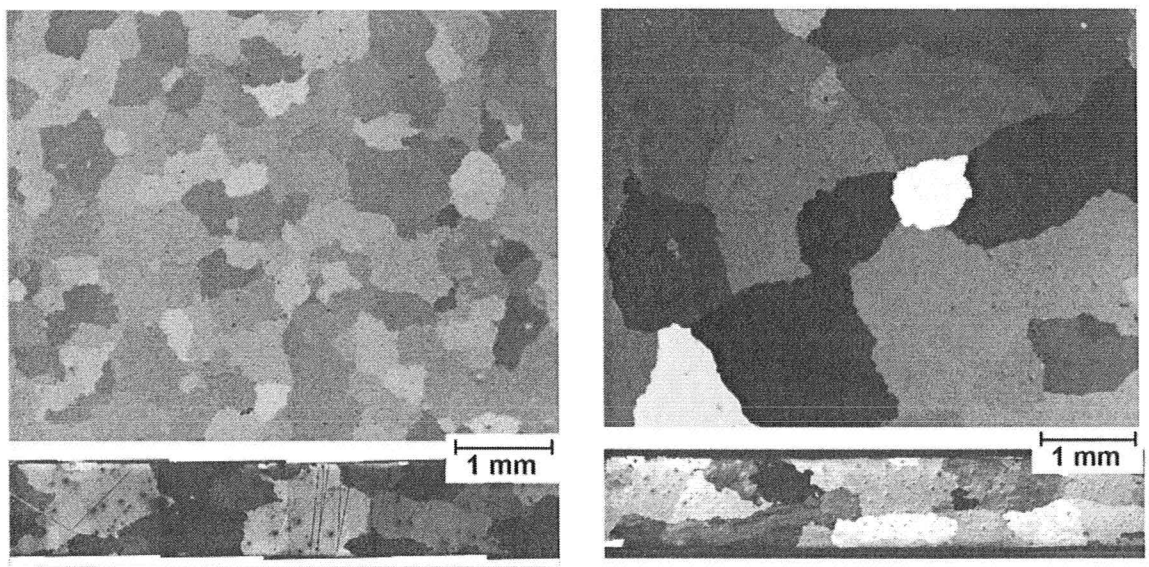

(a) thickness reduction: 7% (b) thickness reduction: 4%

Figure 4-1 Surface (top) and cross-section (bottom) microstructure

With different thickness reduction ratios, surface recrystallization grain size increases with decreasing pre-deformation ratio (Figure 4-1&3). Some small grains within the samples at small thickness reduction probably are the traces of unremoved fine surface grains (Figure 4-1(b) &2(a)).

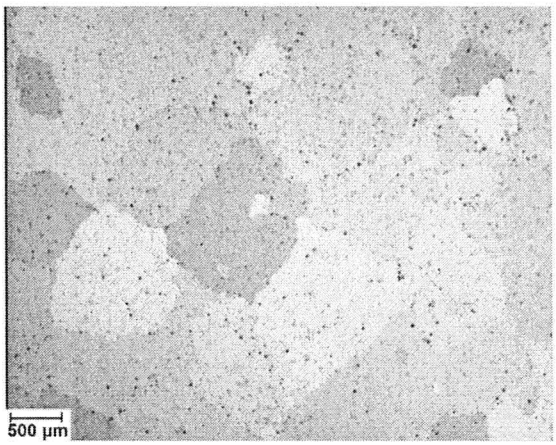

(a) thickness reduction: 5%

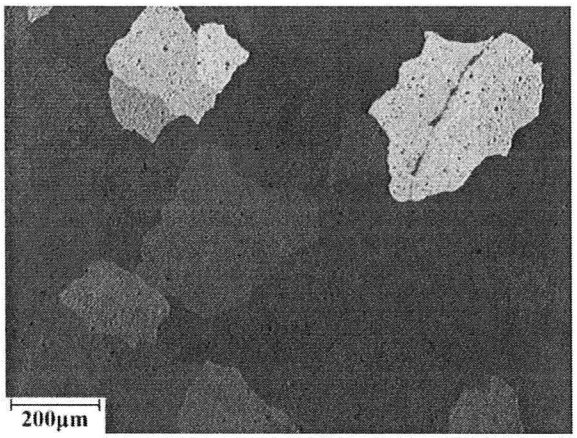

(b) thickness reduction: 9%

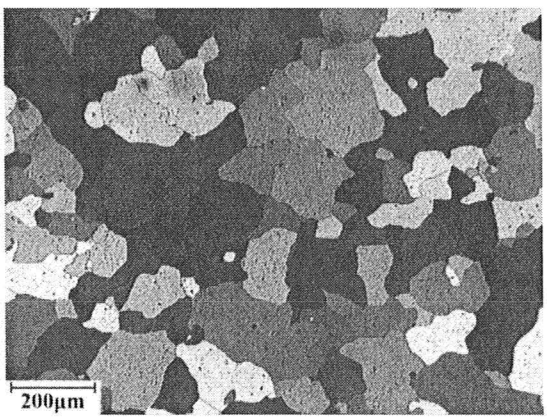

(c) thickness reduction: 15%

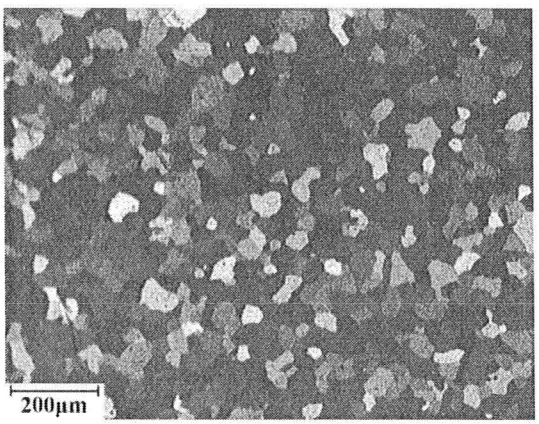

(d) thickness reduction: 20%

Figure 4-2 Microstructure at different thickness reduction ratio by cold rolling: (a)-(d) are for thickness reduction in a range of 5%,9%,15% and 20%, separately

4.1.2 Grain Size versus Pre-deformation Ratio

Average grain sizes with different thickness reductions are summarized in Table 4-1 and plotted in Figure 4-3. The average cross-sectional grain size is

bigger than the average surface grain size due to its discoid shape. Within experimental error, grain size increases with decreasing thickness reduction, and increases dramatically with less than 6% thickness reduction.

Table 4-1 Grain size vs.pre-deformation ratio

Pre-deformation Ratio	Surface Grain Size /μm	Cross-section Grain Size# /μm	Cross-section layers of grains
4%±1%	1500±300	3000±600	1
5%±1%	1250±250	1500±300	1
7%±1%	355±45	600±120	1.5-2
8%±1%	294±33	420±80	1.5-2
9%±1%	150±17		
9%±1%	247±31	384±50#	3-4
11%±1%	96±9	237±30#	4-5
15%±1%	58±4	85±8#	17

Notes: # means only measured using the lines parallel to sample surface.

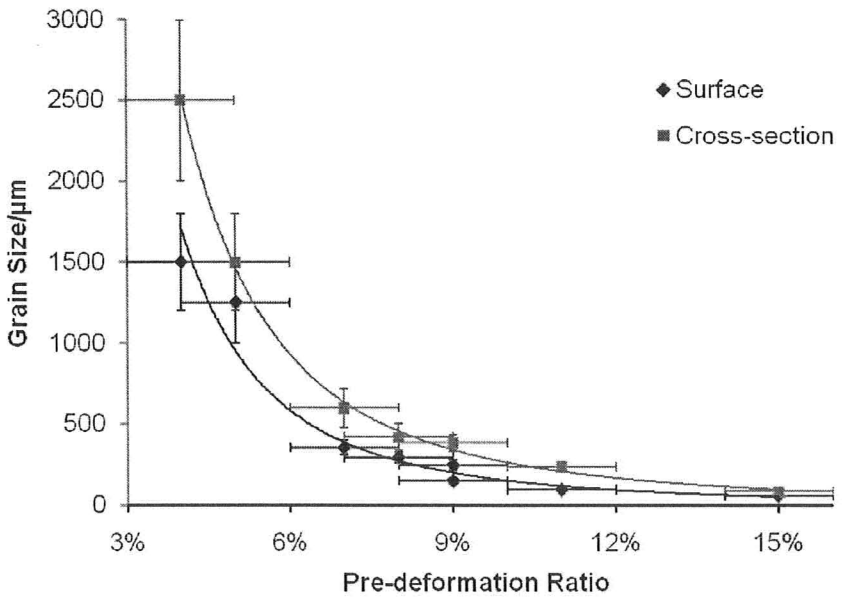

Figure 4-3 Grain size vs. pre-deformation ratio

Grain structure has mirror symmetry to the central line, which is rooted in results in the symmetry of mill rolling procedure. Nucleation sites and grain growth rates reduce from the surface to the center of sheets due to the decreasing deformation stored energy.

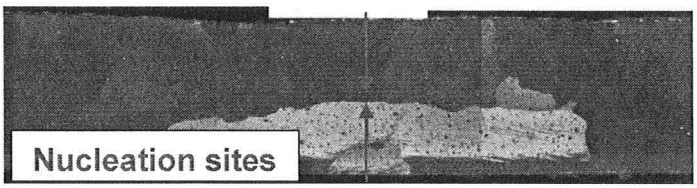

Figure 4-4 Nucleation and growth of grains

The adopted grain size should be big enough to get two-dimensional tensile bars, and small enough to show the grain-level inhomogeneities. Considering that the dimension of tensile bars was 0.55-0.65mm in thickness and 4-6mm in width, the current project mainly works on the grain size region around 300-1200 μm.

4.2 Initial Microstructure Characterization

Microstructure characterization, including EBSD mapping and optical microstructure observation, was done on original tensile bars to collect initial microstructure for further analysis.

4.2.1 Initial EBSD Mapping

As revealed from optical characterization, grain boundaries link to form a center line parallel to the surface. Some through thickness grains were observed in specimens with a grain size of 1250μm. EBSD maps for both sides of the specimen displayed such observation. In specimens with an average grain size of 1250μm, misorientation angles between corresponding grains on different

sides of EBSD maps are less than 30°. Grains with similar orientations (misorientation angle <15°) are observed (Figure 4-5).

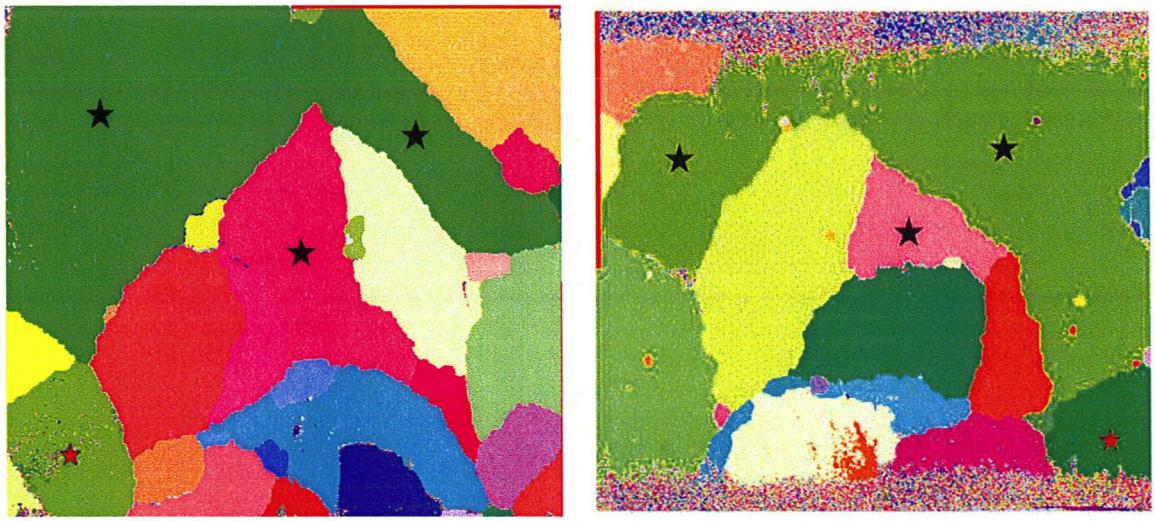

(a) Side A (b) Side B

Figure 4-5 IPFs of normal direction for G1250-2

Note: Modification methods in Appendix.1 are applied to reduce the experimental error within 2° for grain orientation. Grains with similar orientations (misorientation angle <15°) are highlighted with star marks.

Preferred recrystallization grain orientation was obtained from a series of IPFs for specimens with a different grain size. Grains are generally randomly distributed in the transverse direction (Figure 4-6 (a) and (b)), avoid <1 1 1> and <0 0 1> at rolling direction ((Figure 4-6 (c) and (d))), and avoid <0 1 1> at normal direction (Figure 4-6 (e) and (f)). In short, grains prefer $\{001\}$ and $\{112\}$ as the rolling surface, $<110>$, $<3\bar{1}0>$ and $<63\bar{4}>$ parallel to rolling direction. These orientations are closed to R-Cube (Rotated Cube), S and H texture components of these ten major components in aluminum.

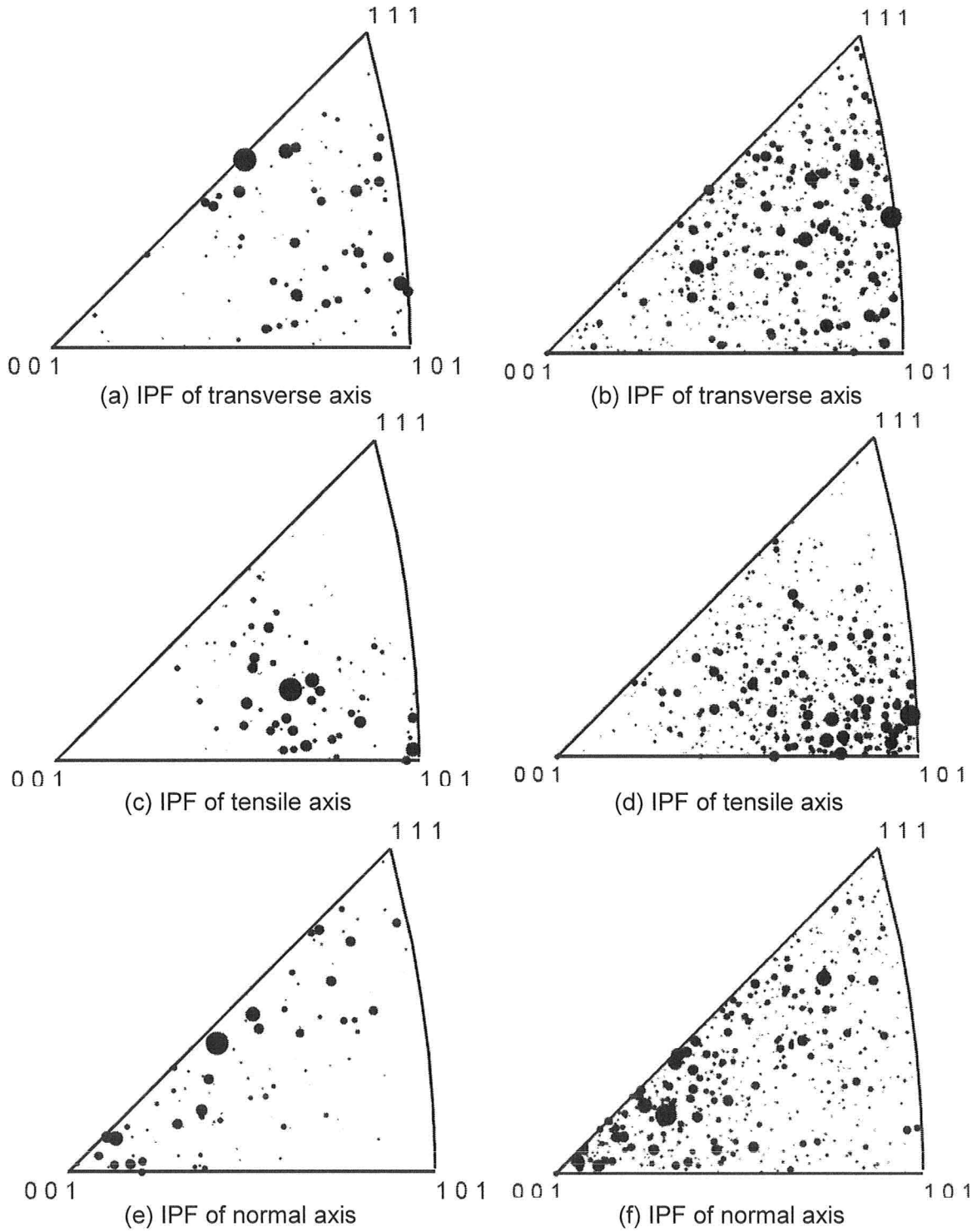

Figure 4-6 IPFs of G600-2 and G350-2: (a),(c) and (e) are for G600-2 and (b),(d) and (f) are for G350-2.

Note: The size of spots stands for the comparable size of grains in one diagram.

4.2.2 Initial Distribution of Second-phase Particles

The volume fraction of second-phase particles is smaller than that of as-received materials because the majority of Mg-rich particles are dissolved during the thermal-mechanical treatment (Figure 4-7).

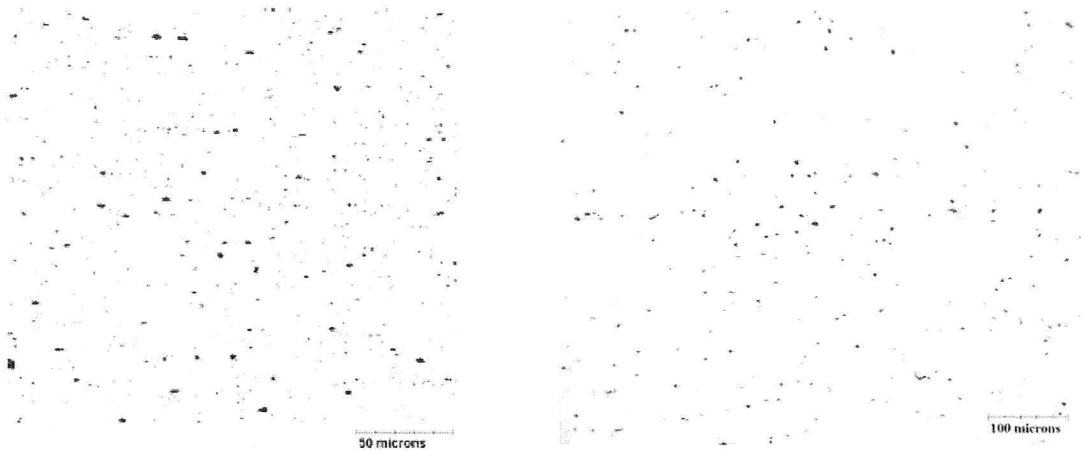

(a) As-received materials (b) After heat-treatment

Figure 4-7 Comparison of the distribution of second-phase particles

4.3 Tensile Properties of Samples with Different Grain Size

Engineering stress-engineering strain curves of specimens with different grain size (Figure 4-8) are obtained by uniaxial tensile tests on two-surface polished samples with shape I. Specimens with larger grain size experienced smaller strength. In addition, samples with larger grain size have comparatively short post-necking processes since the region after maximum load become shorter. Moreover, the transition regions of elastic-plastic deformation are different.

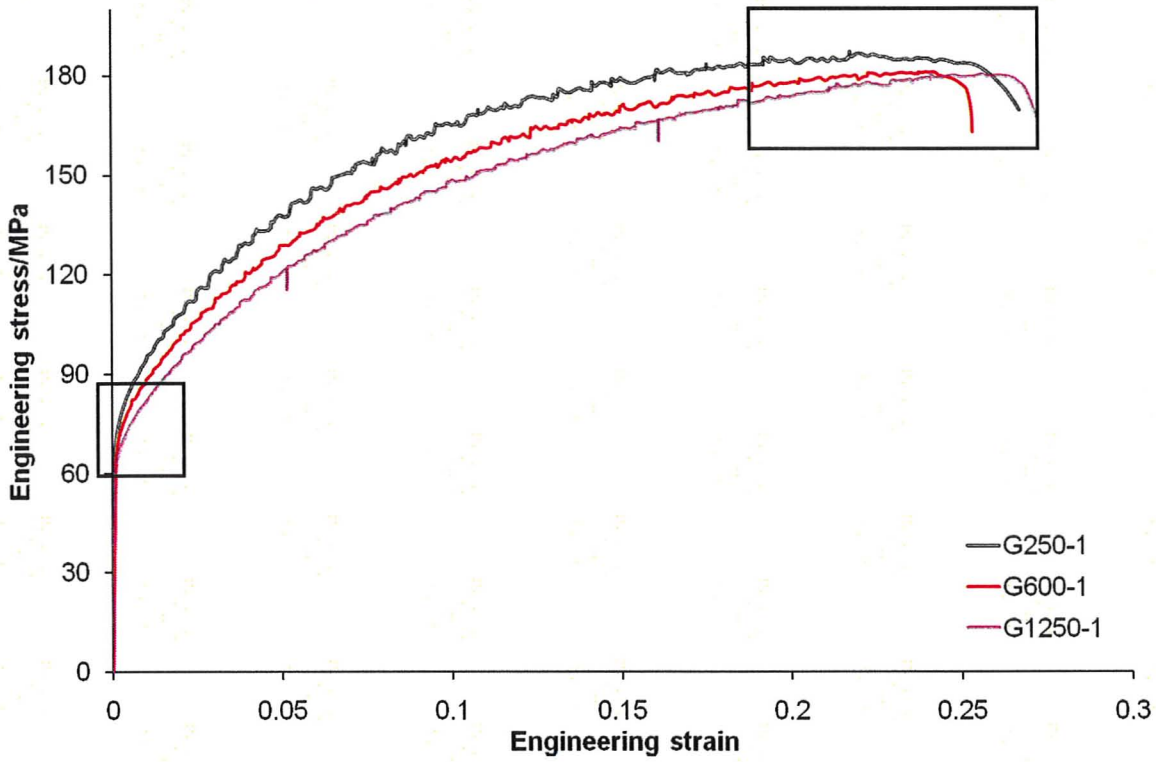

Figure 4-8 Engineering stress-engineering strain curves of selected samples with three typical grain sizes

Another two points are worth to be mentioned here. First, the increment of serrated stress seems fairly small compared to the one with normal grain size, and reduces with increasing grain size. One possible explanation is that large grain inhomogeneities take over the PLC effect in coarse-grained samples. Secondly, several points with suddenly reduced stress may exist during the deformation process, probably because of the rotation of grains: grain rotates to some kind of orientation where they could activate another slip system(s), especially one with a large Schmid factor which may not be activated at the beginning due to compatibility.

Mechanical properties of coarse-grained specimens are listed in Table 4-2.

Table 4-2 mechanical properties of coarse-grained samples

Samples	Grain size /microns	Yield strength*/MPa	UTS/GPa	Work- hardening index n
G1250-1	1200	66.60	227.0	0.3678
G600-1	600	70.24	231.4	0.3357
G420-1	420	71.50	224.8	0.3349
G350-1	350	75.22	230.1	0.3223
G250-1	250	82.47	256.5	0.3352

Petch-Hall relationship is valid for yield strength of the studied materials.

$$\sigma_y = 52.855 + 13.716 \cdot (d)^{-1/2}, R = 0.950 \qquad \text{E4-1}$$

Where, d is the average diameter of grains in millimeters; σ_y is the yield strength in MPa. R is correlation coefficient for linear regression. However, UTS does not show a clear relationship with grain size.

Petch-Hall law is based on grain-boundary strengthening mechanism. Therefore, valid Petch-Hall relationship for yield strength implies the initial boundaries effect, how grains adjust themselves with neighbors.

In addition, true stress–true strain curves are fairly different for the specimens with 1200 μm grain size (Figure 4-9). This brings out the effect of different oriented grains in different coarse-grained samples.

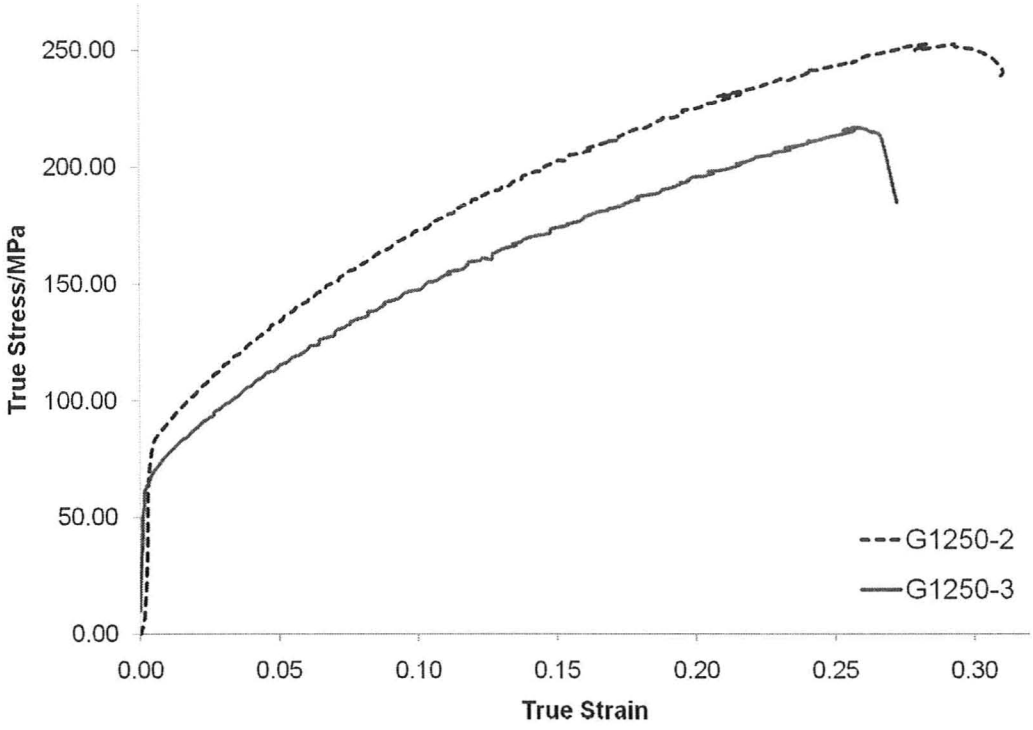

Figure 4-9 Divergence of tensile responses

Note: The true strain in Figure 4-9 was measured by Aramis. G1250-2 and G1250-3 have 1250μm average grain size with 6mm gauge length (Shape II).

To sum up, coarse-grained specimens have shorter post-necking processes and only a slight PLC effect. Their yield strength agrees well with Hall-Petch relationship revealing the initial boundaries effect; different tensile responses of samples with similar grain size support the effect of grain orientation. To show grain-level inhomogeneities, further research was carried on specimens with grain size larger than 500 μm.

4.4 Experimental Results of Specimen G1250s

4.4.1 Initial Orientation Mappings

Grain structure for both sides of the gauge area for the sample with 1250μm grain size G1250-2 is presented in IPF colouring maps (Figure 4-10(a) and (b)). The orientation of Grains (numbering 1-16) is plotted in IPFs of tensile axis (Figure 4-10(c) and (d)).

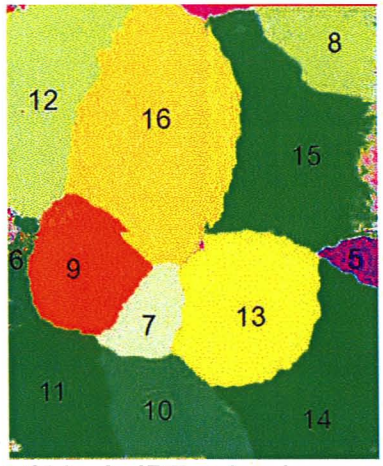

(a) Side A, IPF colouring maps

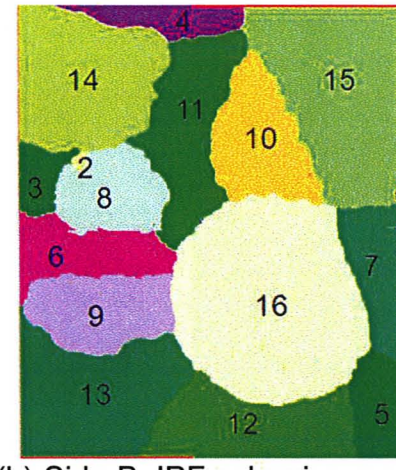

(b) Side B, IPF colouring maps

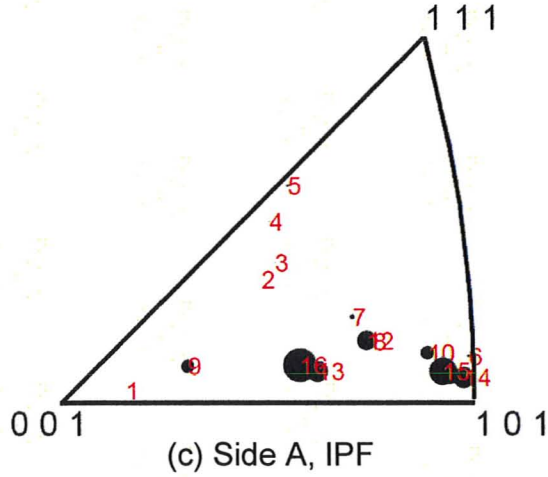

(c) Side A, IPF

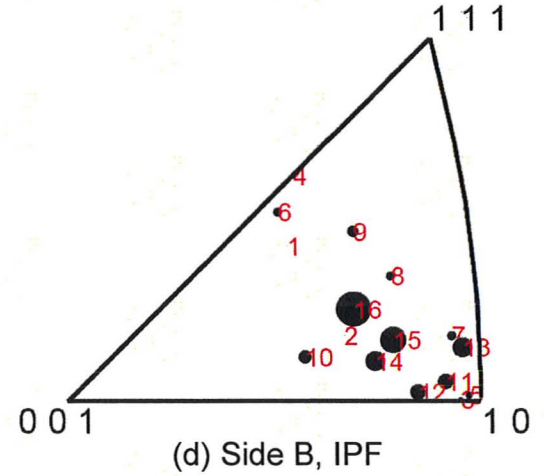

(d) Side B, IPF

Figure 4-10 IPF maps and IPFs of tensile axis for gauge area of G1250-2

Note: Side A and Side B have mirror symmetry at the vertical direction.

4.4.2 Tensile True Strain Mappings

The evolution of surface plastic strain profiles for both sides of G1250-2 with shape II is obtained by 2-2-D DIC techniques. Surface tensile true strain maps for side B are displayed in Figure 4-11. Local strain concentration regions are colored in red within these surface strain maps, and are named as 'hot spot' for their hot color. In specimens with an average 1200 μm grain size, most 'hot spots' form 'hot bands' across the width. These 'hot bands' nucleate at very early stages of the deformation, and keep sustained growth during almost all of the deformation stages.

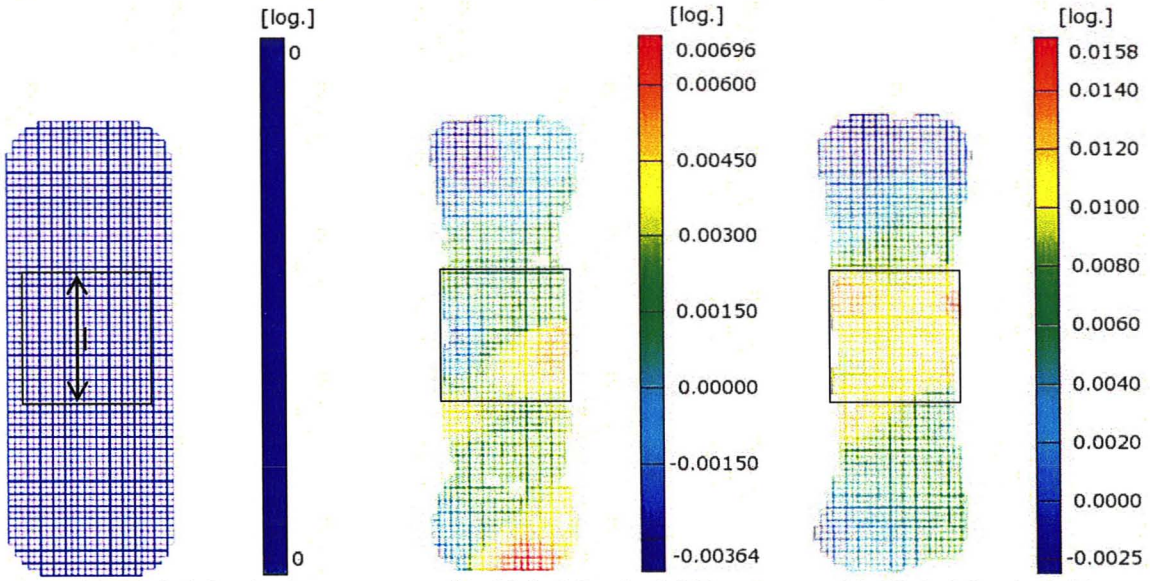

(a) Global Strain:0 (b) Global Strain:0.002 (c) Global Strain:0.01

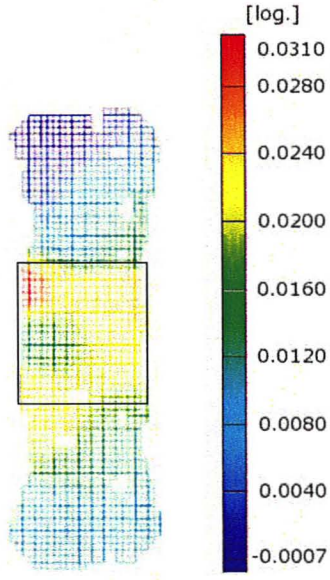

(d) Global Strain:0.02

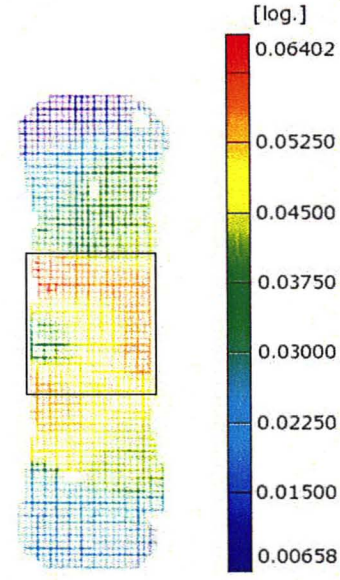

(e) Global Strain:0.05

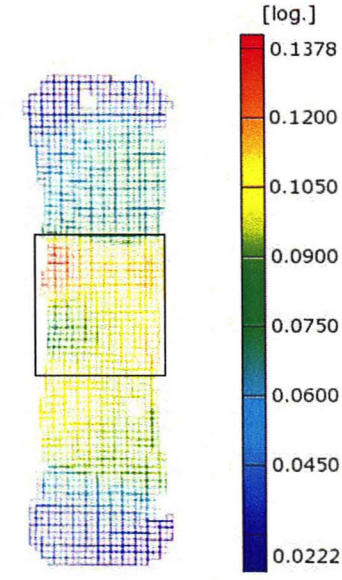

(f) Global Strain:0.1

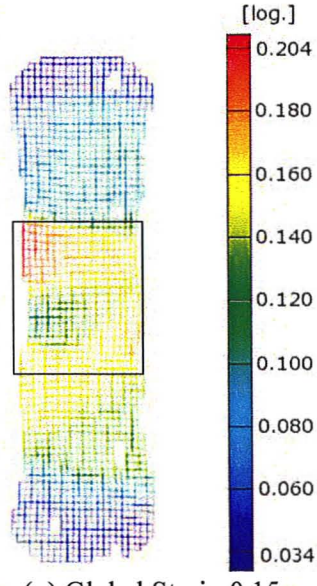

(g) Global Strain:0.15

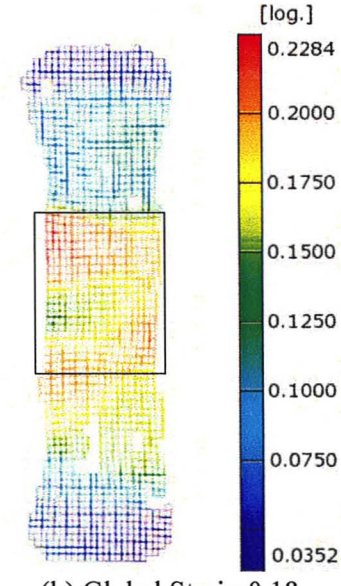

(h) Global Strain:0.18

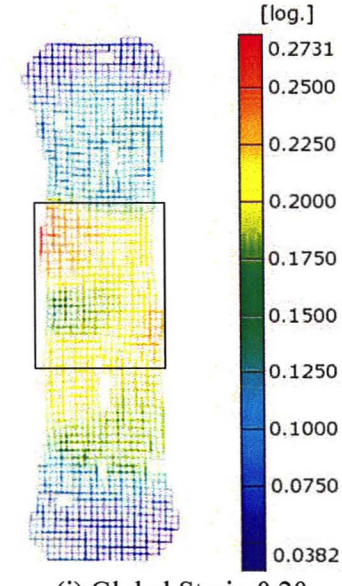

(i) Global Strain:0.20

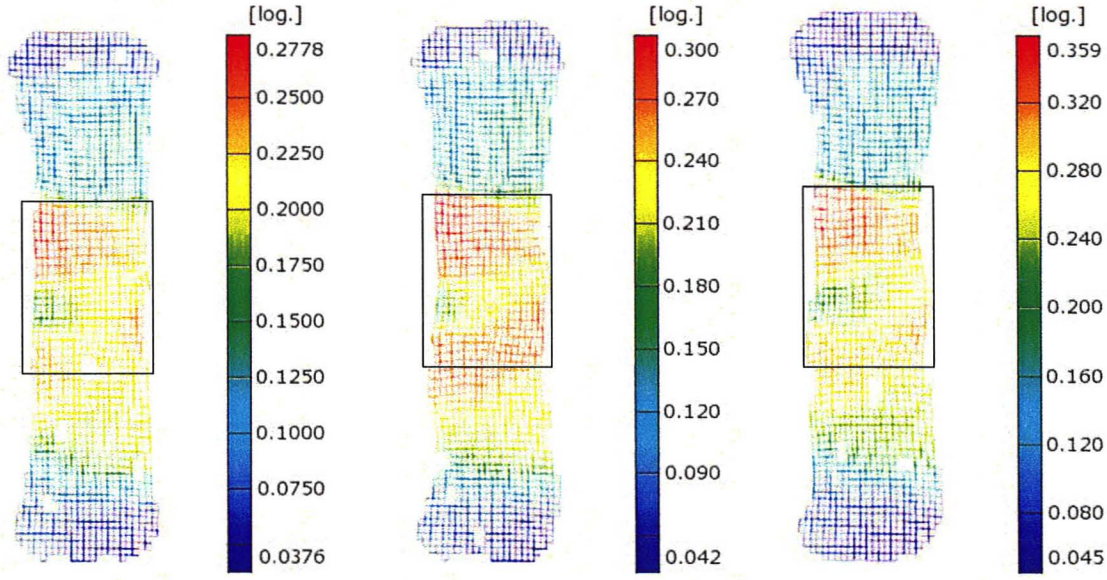

(j) Global Strain:0.22 (k) Global Strain:0.25 (l) Global Strain:0.27

Figure 4-11 Tensile true strain maps for Side B of G1250-2

Note: The area in rectangle for each image is the gauge area shown in Figure 4-10(b).

Section I is the trace of line scan in Figure 4-13.

Tensile true strain maps for both sides are quite similar, which implies that grains in side A have high coordination with corresponding grains in Side B. (Figure 4-12)

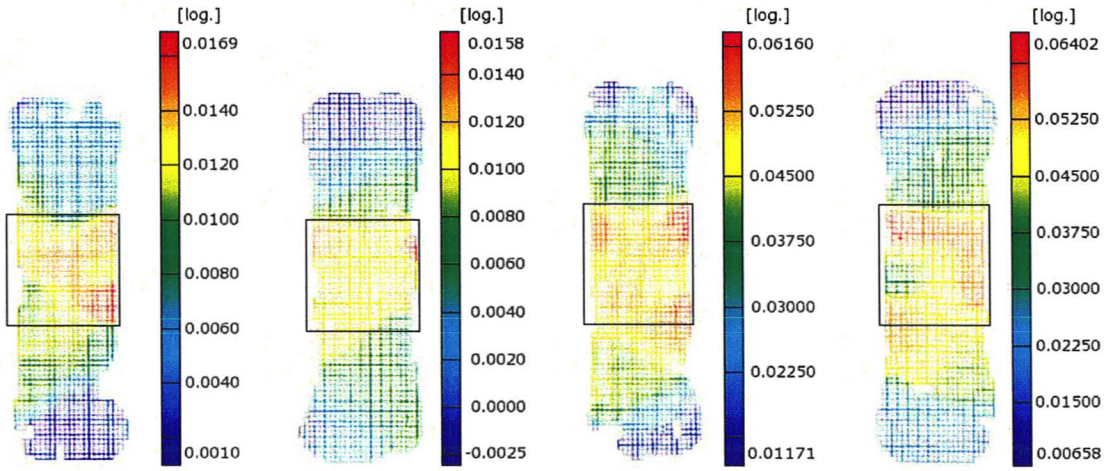

(a) Side A, 0.01 (b) Side B,0.01 (c) Side A,0.05 (d) Side B,0.05

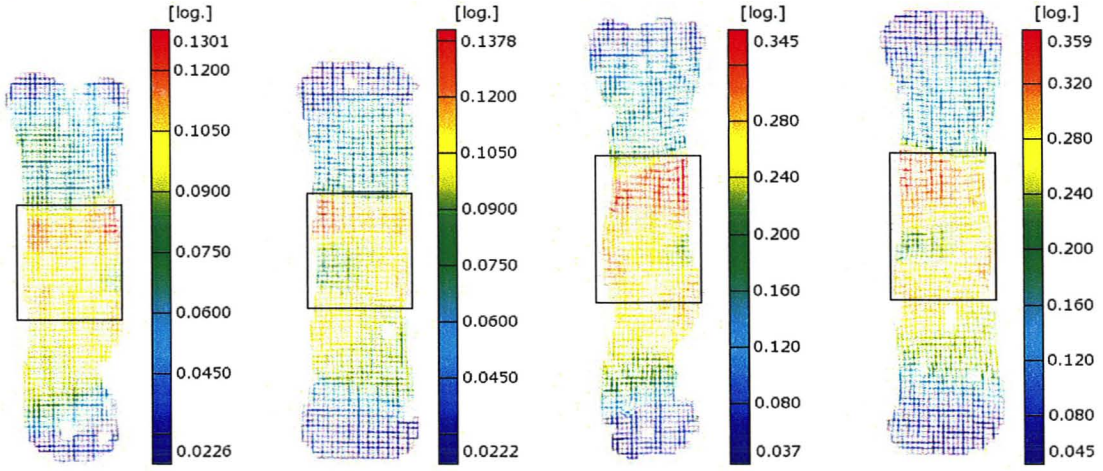

(e) Side A,0.1 (f) Side B,0.1 (g) Side A,0.27 (h) Side B,0.27

Figure 4-12 Comparison of strain maps of both sides at certain true strain

Note: Strain maps in rectangles in (a),(c),(e)and (g) are for the same area of Figure 4-10(a). Strain maps in rectangles in (b),(d),(f)and (h) are for the same area of Figure 4-10(b).

To clarify the evolution of hot bands, strain distribution evolutions of a line scan along tensile direction (section I in Figure 4-11) are shown in Figure 4-13. Strain distribution along the tensile direction keeps similar shape with strain until the deformation concentrates to one of the initial sharp peaks leading to the necking. The periodicity of those peaks is around 4.5mm, containing 3-4 grains.

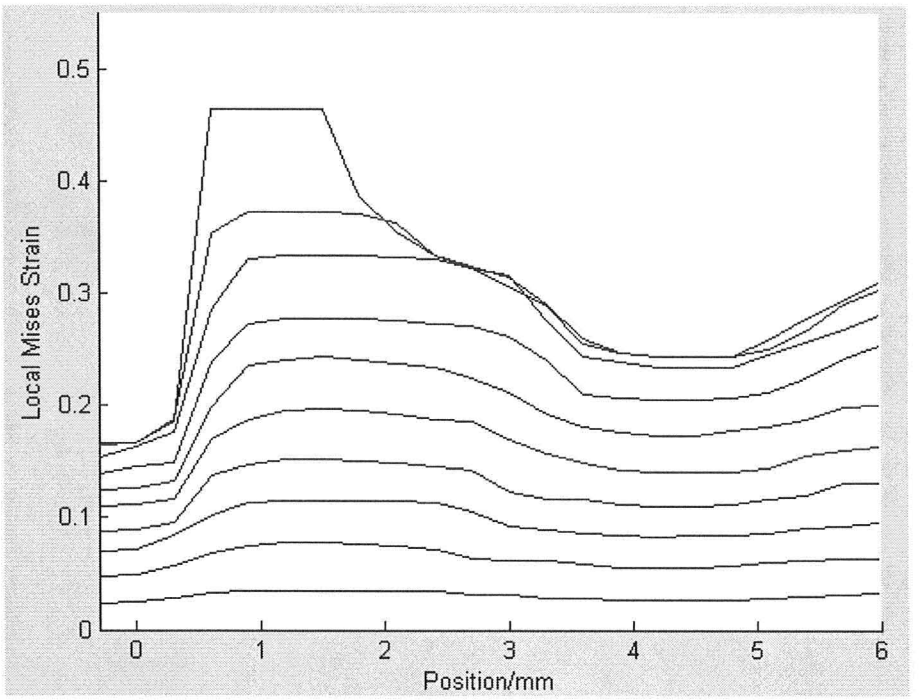

Figure 4-13 true strain vs. position graphs (stage: 0-180; interval: 20)

4.4.3 Surface Features after Fracture

4.4.3.1. Fractography and Fracture Strain

Complete morphology of fracture is presented from top-, surface- and thickness-view (Figure 4-14). Individual grains are indentified directly on the top-view images as seen in Figure 4-14(a) and (b). This implies that plastic deformation inside grains is much more homogenous than that near grain boundaries.

The morphology of the fracture surface is different within different regions since the regions are strongly related to the location of grains (Figure 4-14(d)). Single-directional shear along the fracture profile is observed in the overlap region of Grain A8 (Grain 8 in Side A) and B14 (Grain 14 in Side B) (Figure 4-14(c)). The region with big thickness reduction is located inside the overlap

regions of Grain A12 and B15. Fracture stress is calculated to be 360 MPa from the section area of facture surface.

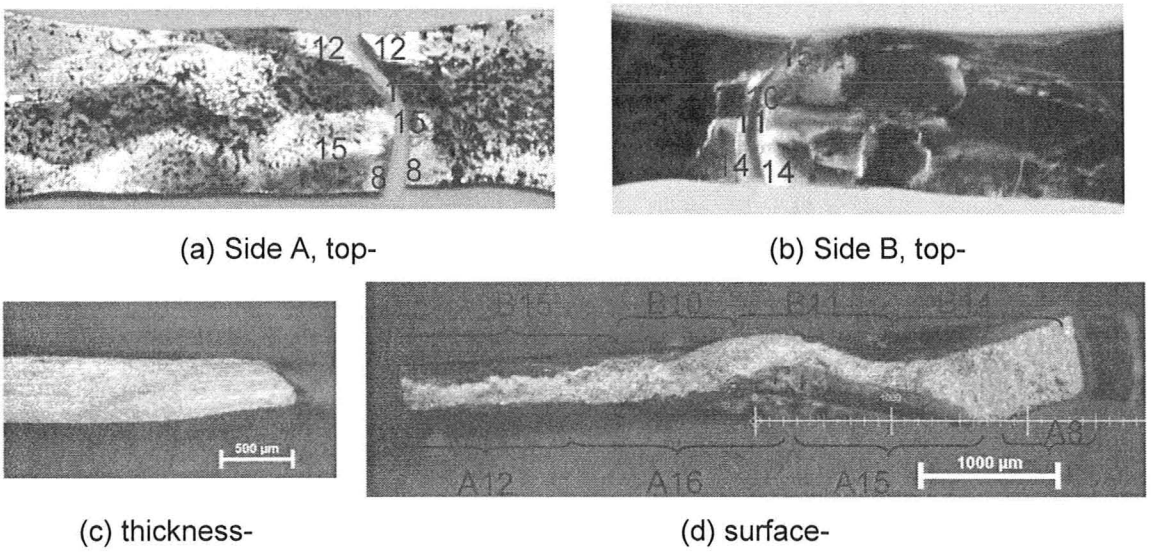

(a) Side A, top- (b) Side B, top-

(c) thickness- (d) surface-

Figure 4-14 Fractography of G1250-2

Note: Grains inside localization region are indentified according Figure 4-10.
A and B in (d) index Side A and Side B, separately.

4.4.3.2 Surface slip traces

One or two series of slip traces with homogeneous internal spacing were observed inside each grain (Figure 4-15(a) and (c)). Inside neighboring grains the same slip direction was observed. Complex morphology of slip traces was observed within a 100 µm transition region while moving from one region to another (Figure 4-15(b)). Slip traces become denser and are more complex for large deformation (Figure 4-15(e) and (f)). Concentration of the slip traces at second-phase particles are presented in Figure 4-15(d).

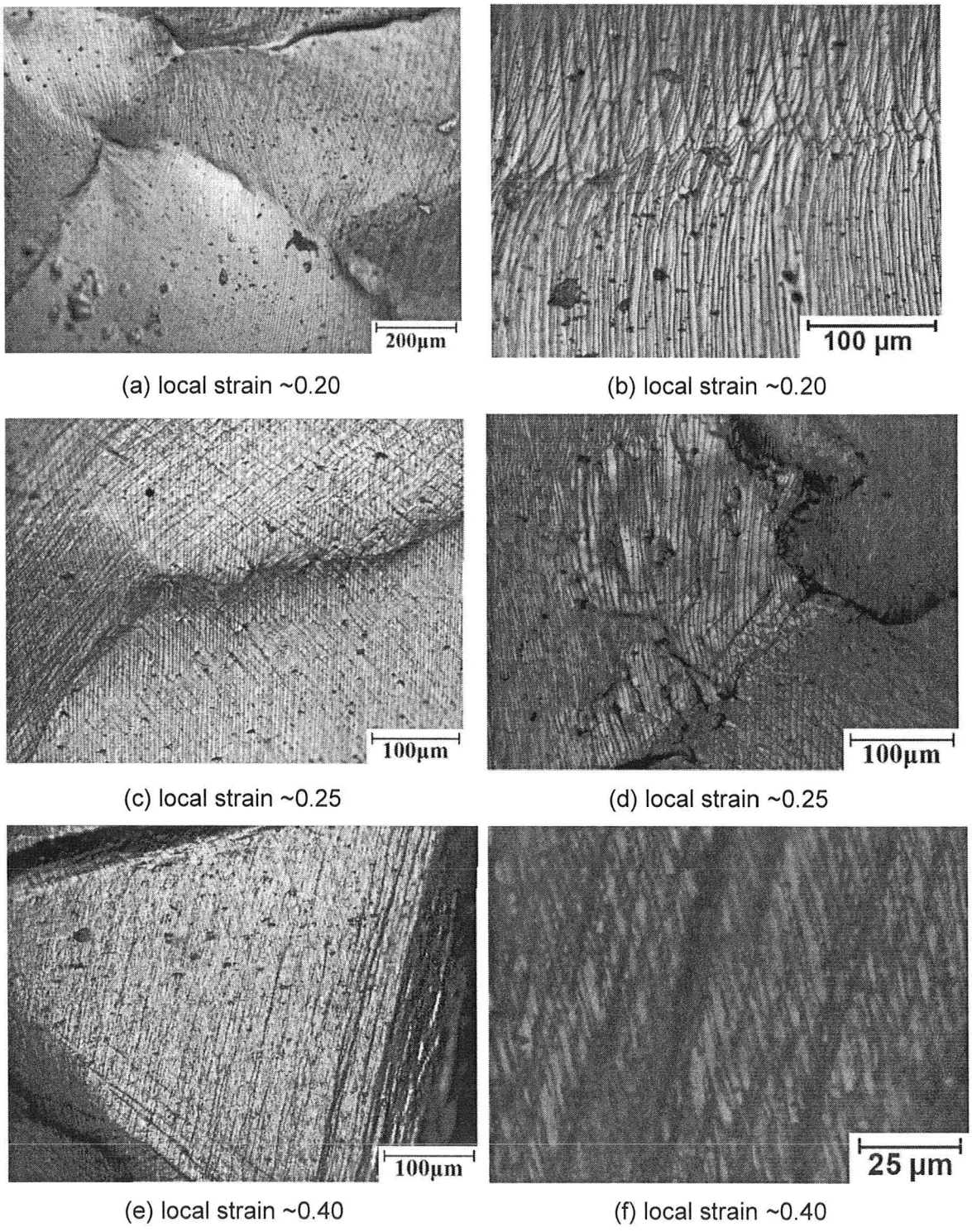

(a) local strain ~0.20 (b) local strain ~0.20

(c) local strain ~0.25 (d) local strain ~0.25

(e) local strain ~0.40 (f) local strain ~0.40

Figure 4-15 Surface traces in specimen G1250-1

The observed slip traces are plotted in IPF colouring maps for both sides of G1250-2 as show in (Figure 4-16). Inside the localization region, major slip traces of Side A grains (Grain 12,16,15,8) hold mirror symmetry to the vertical direction with the ones in the corresponding grains of Side B (Grain 15, 10, 11,14).

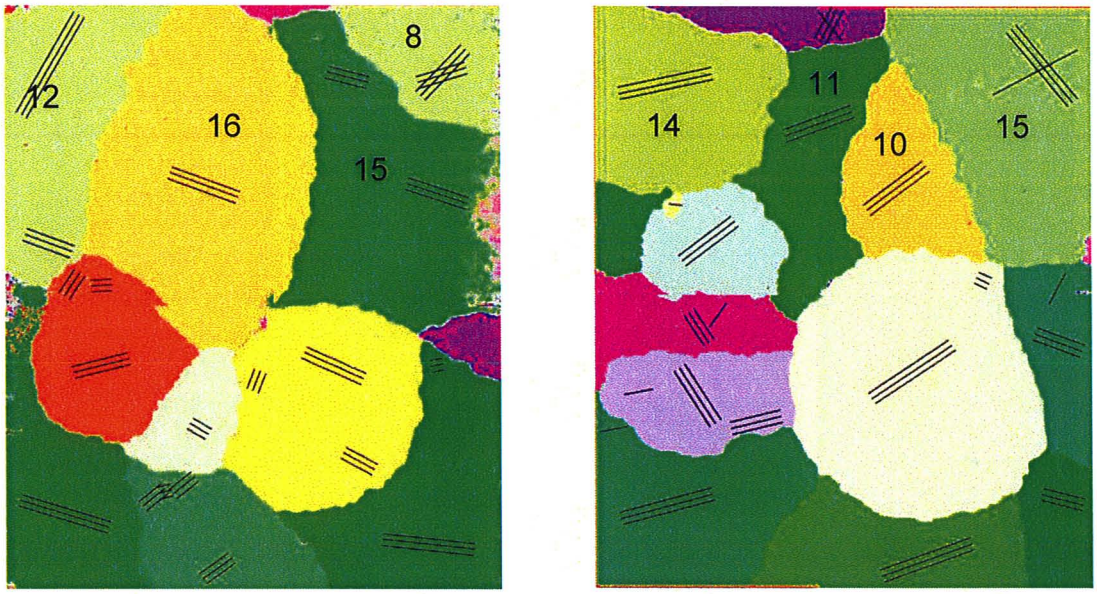

(a) Side A (b) Side B

Figure 4-16 Slip traces in specimen G1250-2

4.5 Experimental Results of Specimen G600s

4.5.1 Initial Orientation mappings

Grain structure for both sides of the gauge region for the sample with 600μm grain size G600-2 is presented in IPF colouring maps (Figure 4-17(a) and (b)). The orientation of Grains is plotted in IPFs of tensile axis (Figure 4-17(c) and (d)).

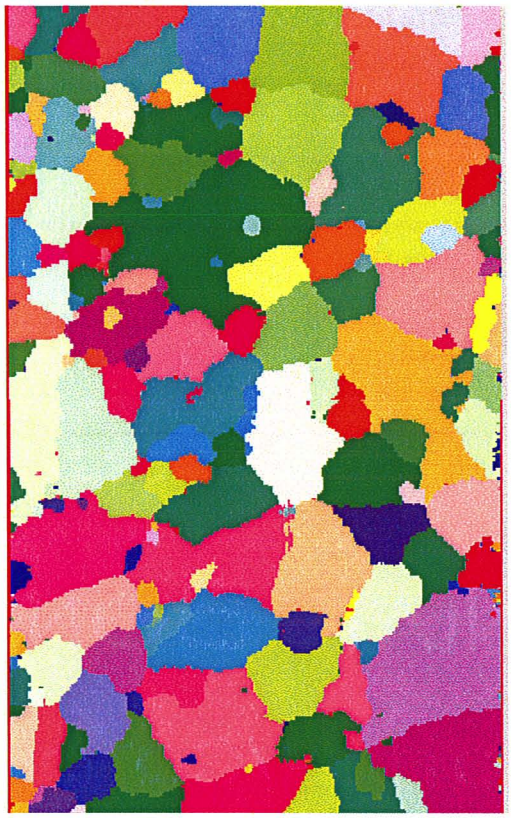

(a) Side A, IPF colouring maps

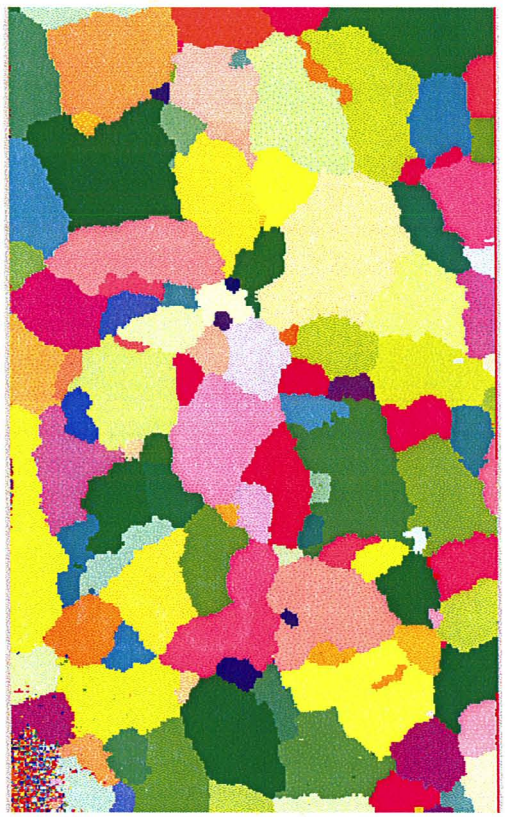

(b) Side B, IPF colouring maps

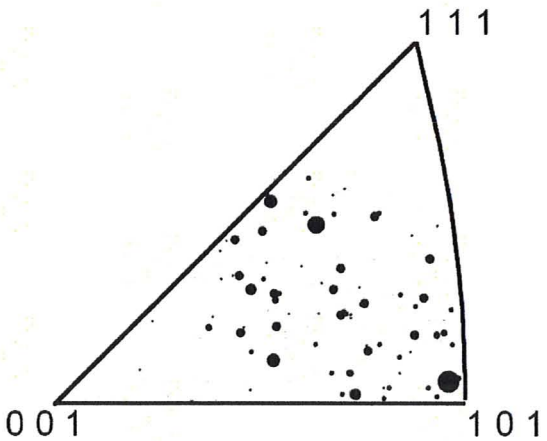

(c) Side A, IPF

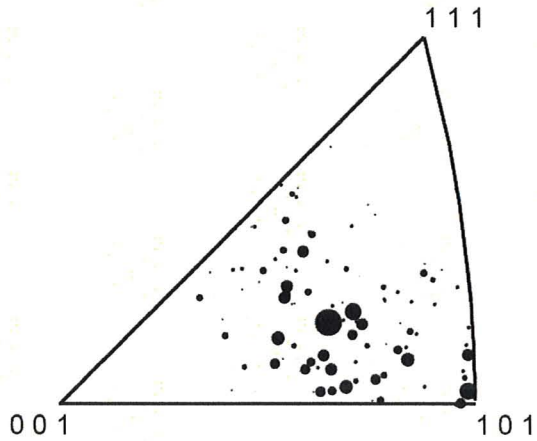

(d) Side B, IPF

Figure 4-17 Initial IPF maps and IPFs of tensile axis for gauge area of G600-2

Note: Side A and Side B have mirror symmetry at the vertical direction.

4.5.2 Tensile True Strain mappings

To enhance the co-deformation effect of grains and get the grain-level inhomogeneities, tensile tests were set up on specimen G600-2 with shape III, which provides more grains across the width compared to G1250-2. Similar phenomena were observed: a few 'hot bands' form at the beginning, and keep sustained growth until facture happens at one of them.

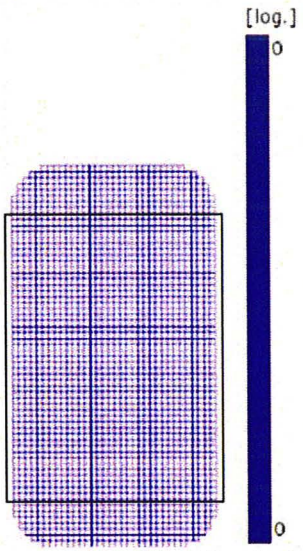

(a) Global Strain:0

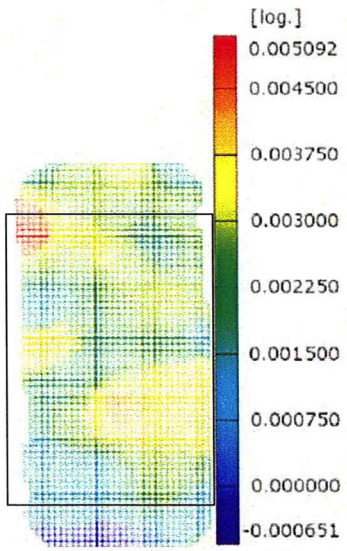

(b) Global Strain:0.002

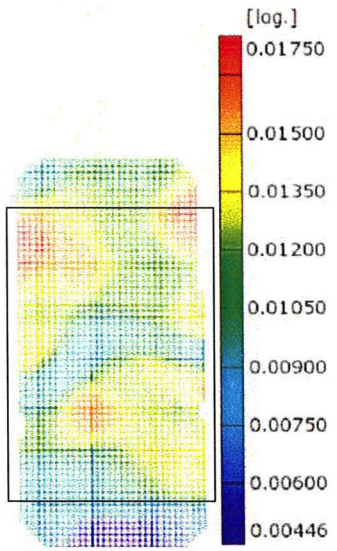

(c) Global Strain:0.01

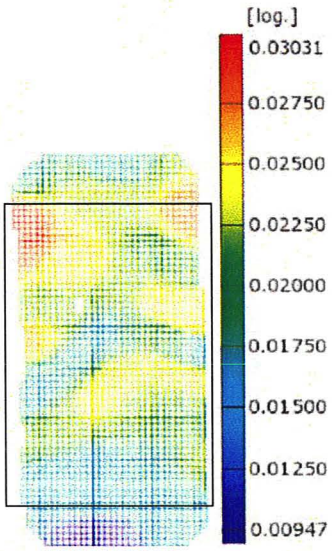

(d) Global Strain:0.02

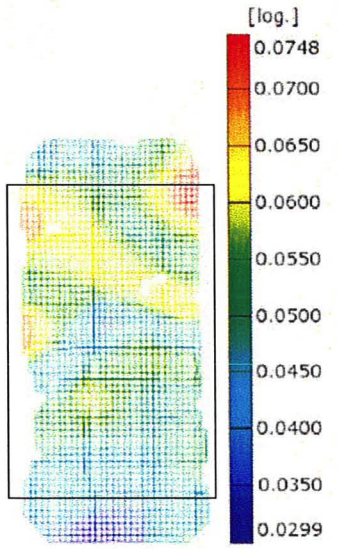

(e) Global Strain:0.05

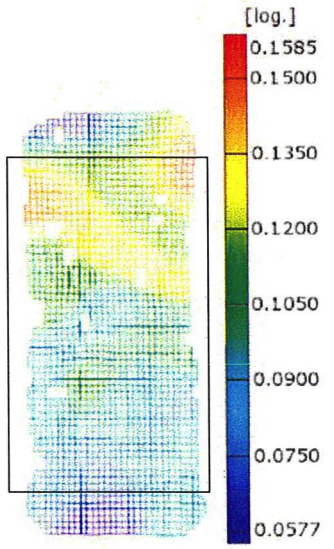

(f) Global Strain:0.1

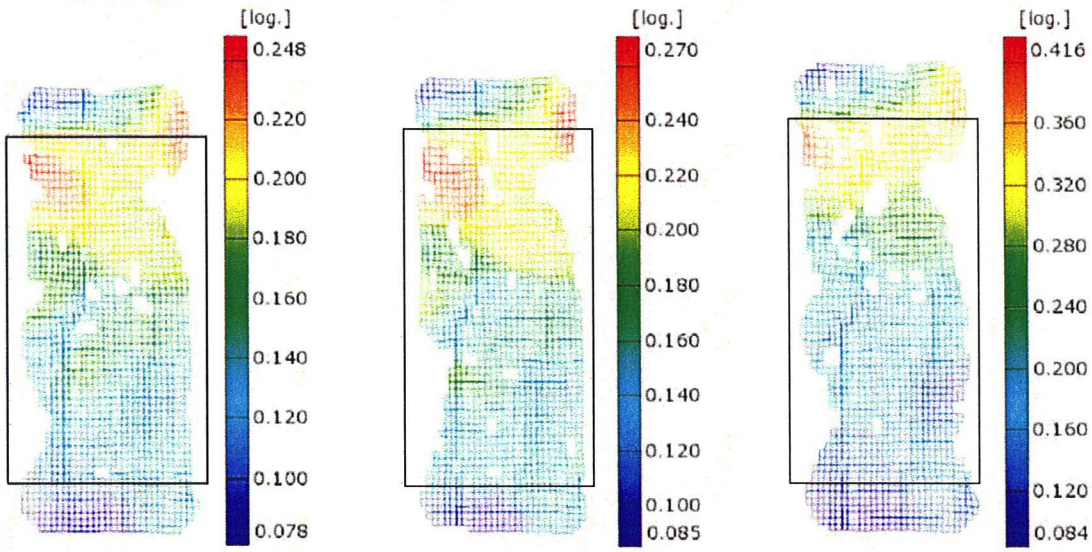

(g) Global Strain:0.15 (h) Global Strain:0.17 (i) Global Strain:0.19

Figure 4-18 Tensile true strain mapping of Side B for G600-2

Note: The area in rectangle for each image is the gauge area shown in Figure 4-17(b).

4.5.3 Fractography and Fracture Strain

Completely facture morphology of G600-2 is presented from the top-, surface- and thickness-view (Figure 4-19). Cup-cone type fracture morphology was observed from the thickness-view. Fracture strain is calculated to be 360 MPa from the section area of facture surface.

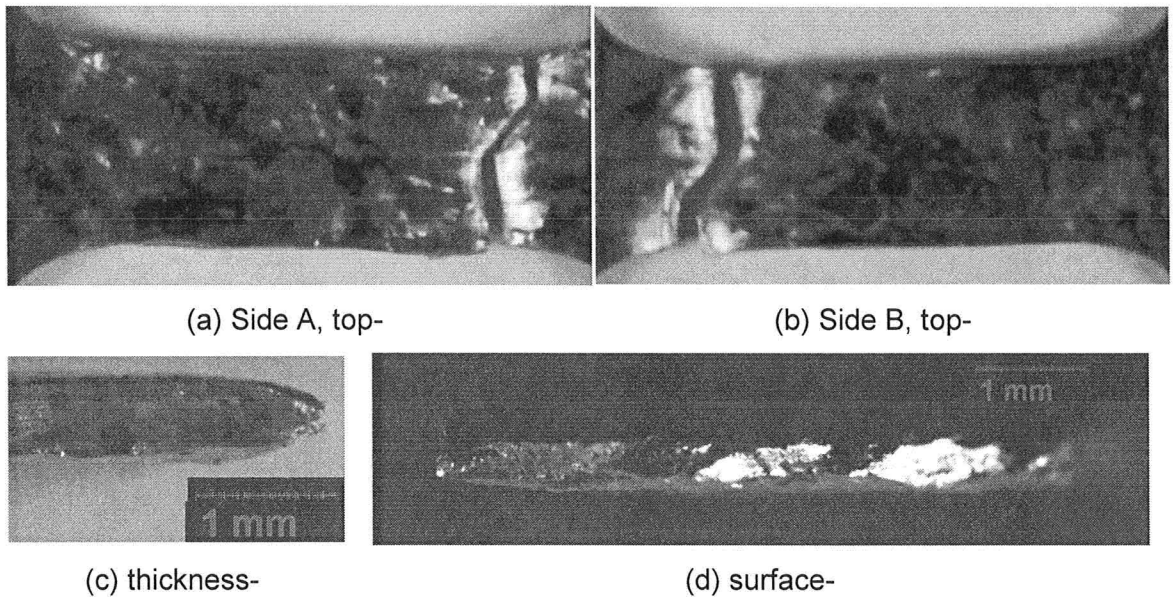

(a) Side A, top- (b) Side B, top-

(c) thickness- (d) surface-

Figure 4-19 Fractography of G600-2

4.6 Surface Features and Their Evolutions during Tensile Processes

4.6.1 Grain Morphology and its Evolution

The elongation and rotation of grains are caused by plastic deformation. Grain structure is revealed in grey level contrast with the visible etching technique and its evolution during plastic deformation is presented in Figure 4-20. The red line arrow indicates the rotation direction of one grain on the frontal plane. Grain rotation vertical frontal plane leads to the changing of grey level contrast. The division of rotation direction inside one grain was observed (circle mark in Figure 4-20).

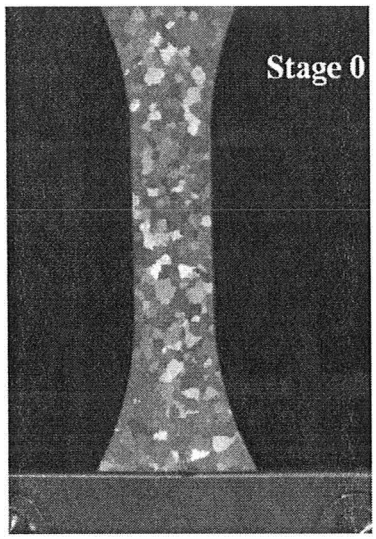

(a) Stage 0

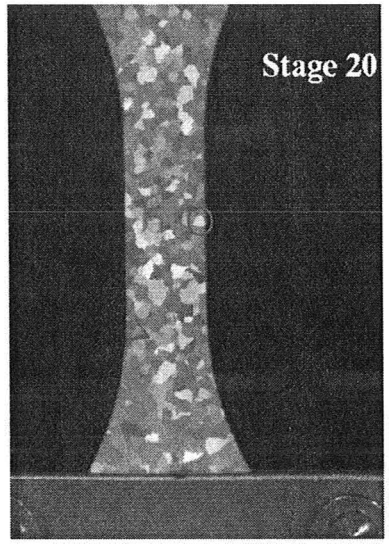

(b) Stage 20

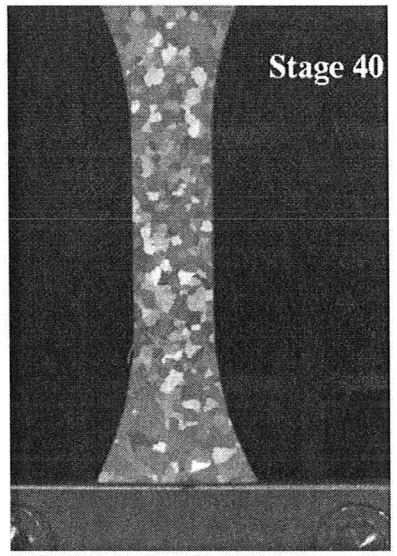

(c) Stage 40

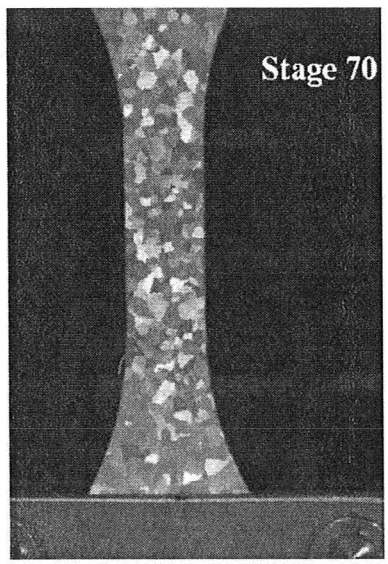

(g) Stage 70

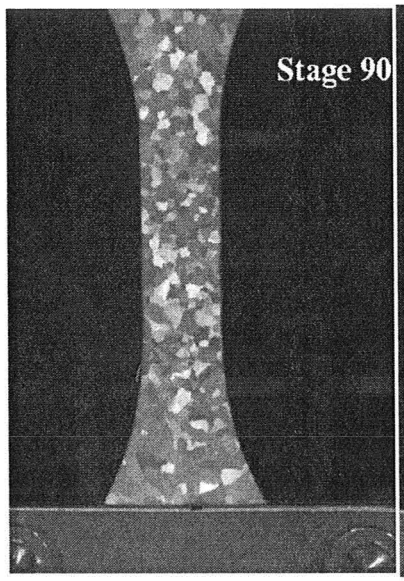

(h) Stage 90

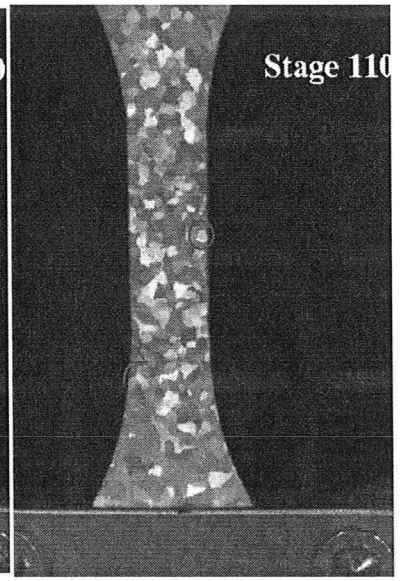

(i) Stage 110

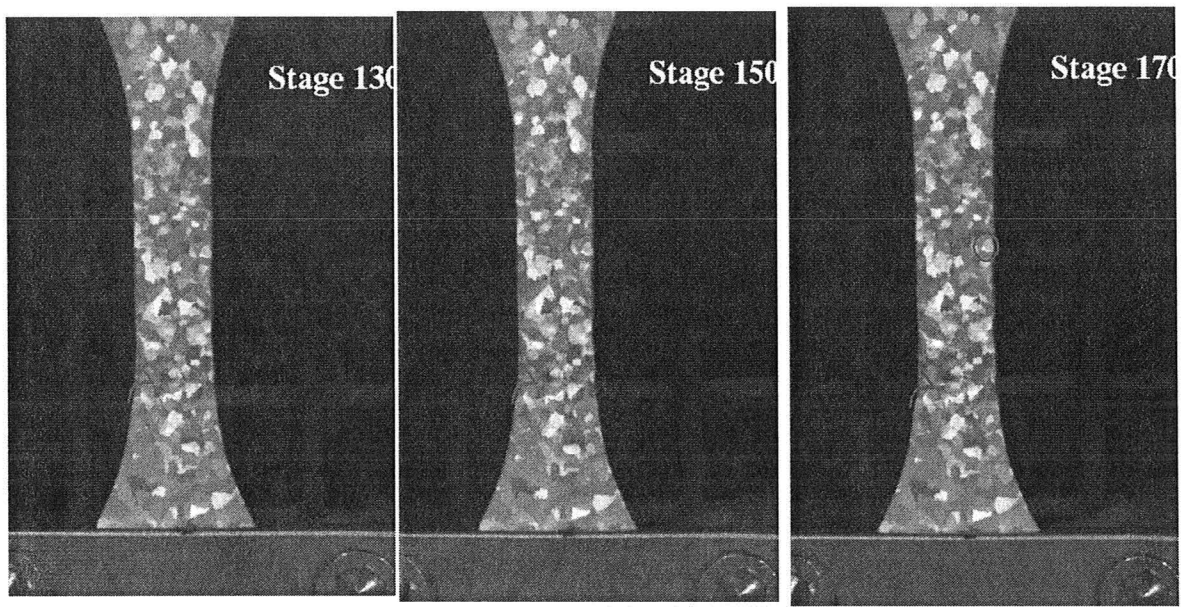

(j) Stage 130 (k) Stage 150 (l) Stage 170

Figure 4-20 Evolution of grain morphology

Note: Red line with arrow indexes the rotation direction of the grain on the frontal plane. Circle highlights the division of the rotation direction of grains.

4.6.2 Grain Orientation and other Surface Features

The purpose of in-situ tensile tests is to obtain the evolution of microstructure, especially the grain orientations. Seven steps were set during the test, named A~G in Figure 4-21. EBSD maps were collected at point A, C, E. SEM images were recorded to represent the surface morphology of specimen G1250-3 at all tensile stops. Surface features are summarized in Table 4-3.

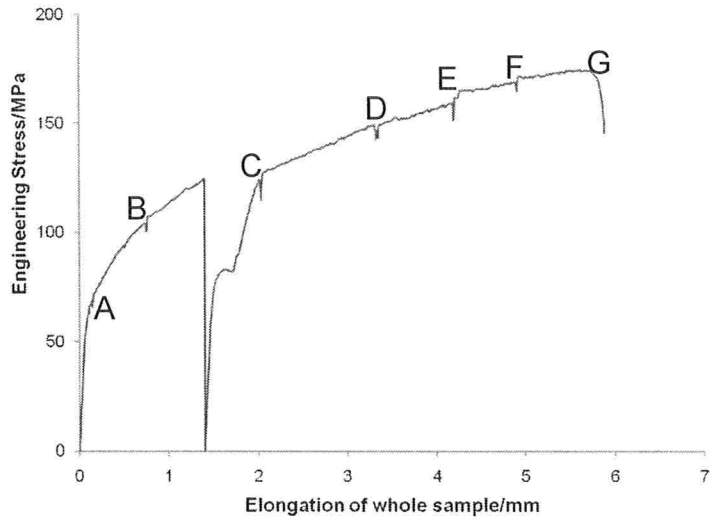

Figure 4-21 Engineering strain v.s. total elongation

Note: Elongation is estimated based on a gauge length of 50mm from an extenso-moniter on the in-situ stage.

Table 4-3 Stop points during tensile test

Steps	Engineering Stress/ MPa	Corresponding Engineering strain*	Surface Features
A	70	yield point	No
B	105	~3%	No
C	125	~6%	slight slip traces, subtle boundaries roughing, little voids
D	150	~11%	slip traces, surface voids, boundaries roughing
E	160	~14%	significant surface roughing, surface voids and deeper slip traces
F	170	~19%	More significant surface roughing, surface voids and deeper slip traces
G	174	~22%	Fracture

Note: Engineering strain is estimated based on the engineering stress-engineering strain curves of G1250-2 at certain engineering stress in the second column.

The change of surface features starts at the very beginning of plastic deformation, and concentrates at grain boundaries (Figure 4-22). From the early stage of plastic deformation, around 6% strain, slip traces and boundary

roughening and even surface voids are observed (Figure 4-23 (a)). All the features become more significant with increasing strain.

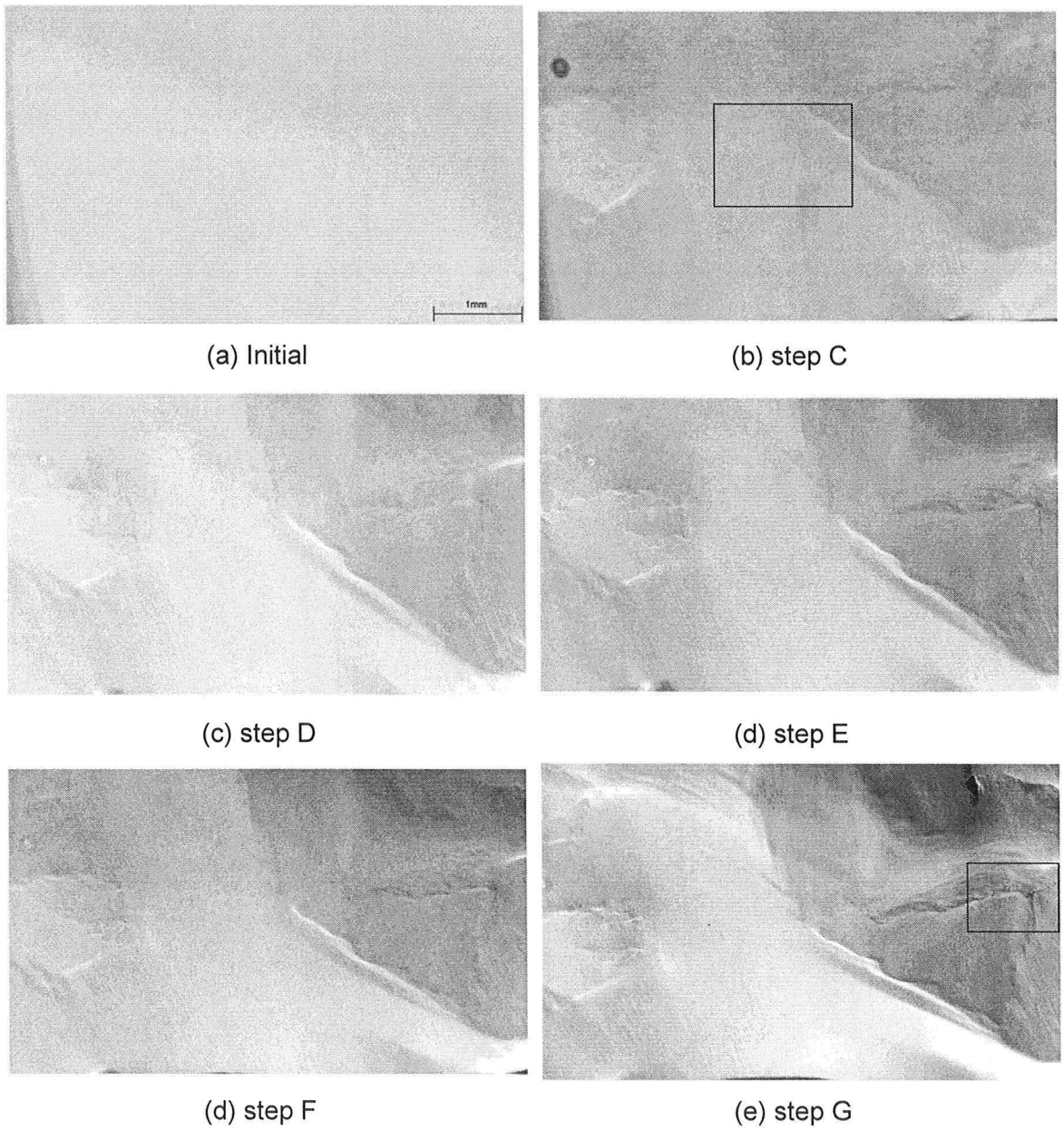

(a) Initial (b) step C

(c) step D (d) step E

(d) step F (e) step G

Figure 4-22 Evolution of surface roughening

Note: the rectangle zones in (b) and (e) are the same area for Figure 4-23 (a) and (b), separately.

The linking of surface voids was observed at grain boundaries (Figure 4-23(b)). Since those surface voids were observed from the beginning for this ductile material these voids may be presented due to the loss of second-phase particles during polishing.

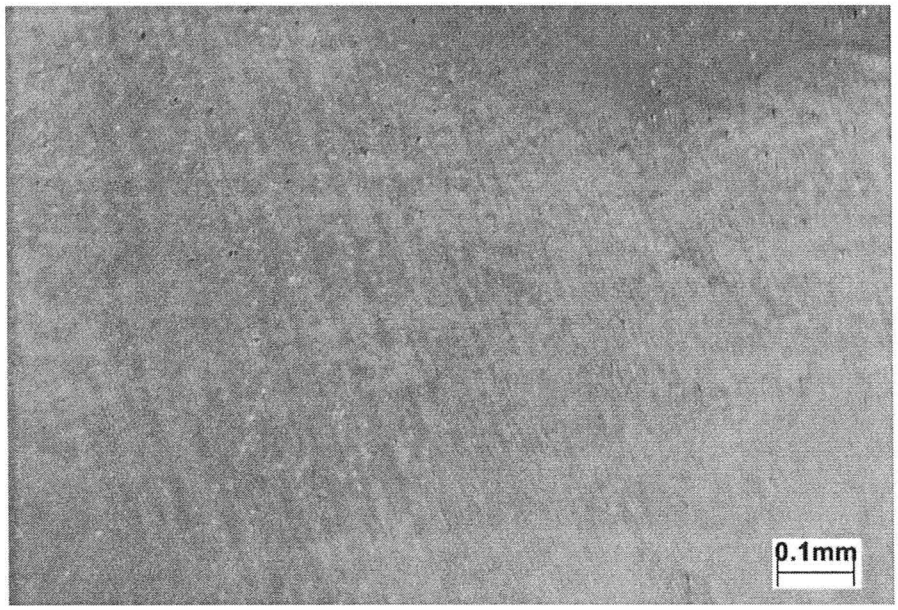

(a) Step C

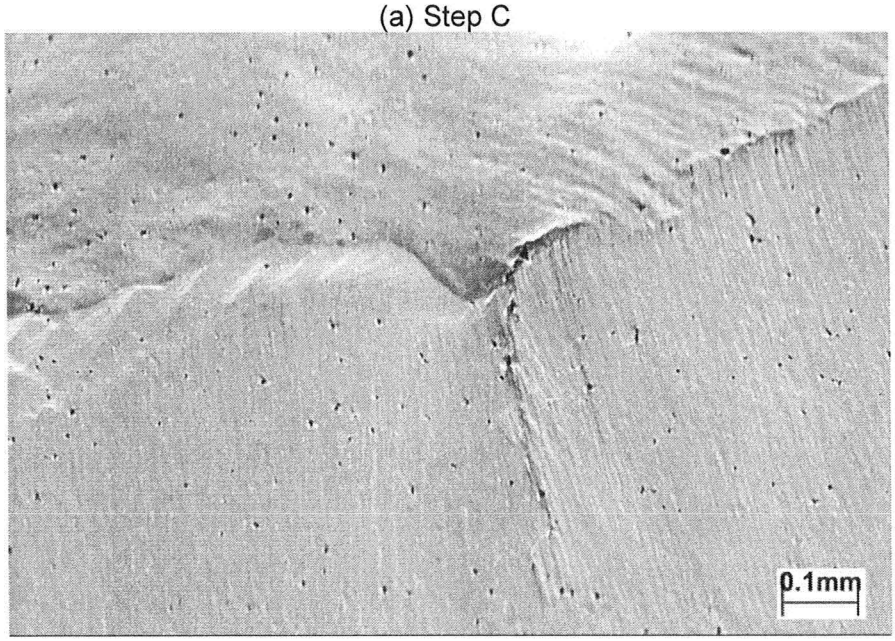

(b) Step G

Figure 4-23 Microstructure evolution

Grain orientation becomes more random during deformation. Sub-grain structure forms since the same initial grain was observed to divide into several parts (Figure 4-24).

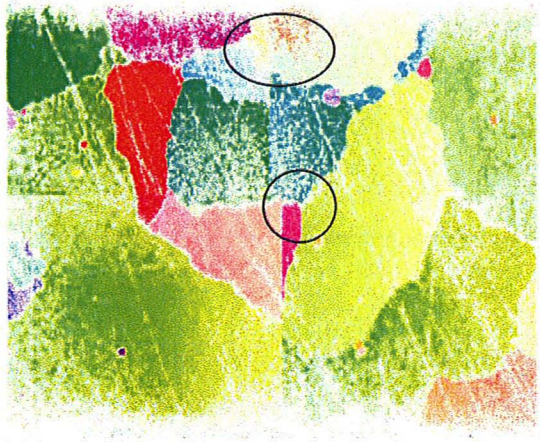

(a) Initial EBSD

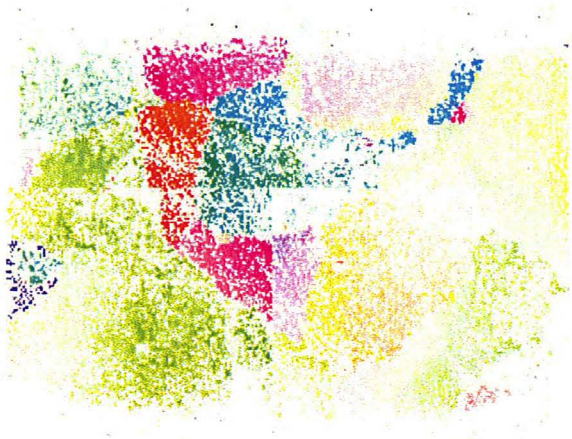

(b) Step C

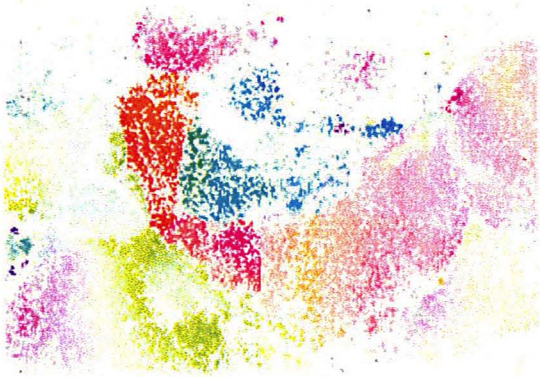

(c) Step E

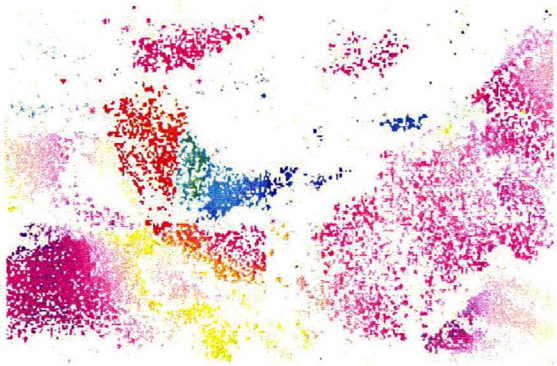

(d) Step G

Figure 4-24 Evolution of grain orientation

Notes: Zones with white color are bad areas for EBSD with low CI due to the bad polishing and deformation.

In Figure 4-24 (a), the zones marked are the crack area, in which the bottom (Circle) stands for Figure 4-23(b).

The evolution of grain orientations is represented in IPFs of tensile axis during deformation (Figure 4-25). Lattice rotates to achieve deformation axis closer to <001>, <112> or <111>.

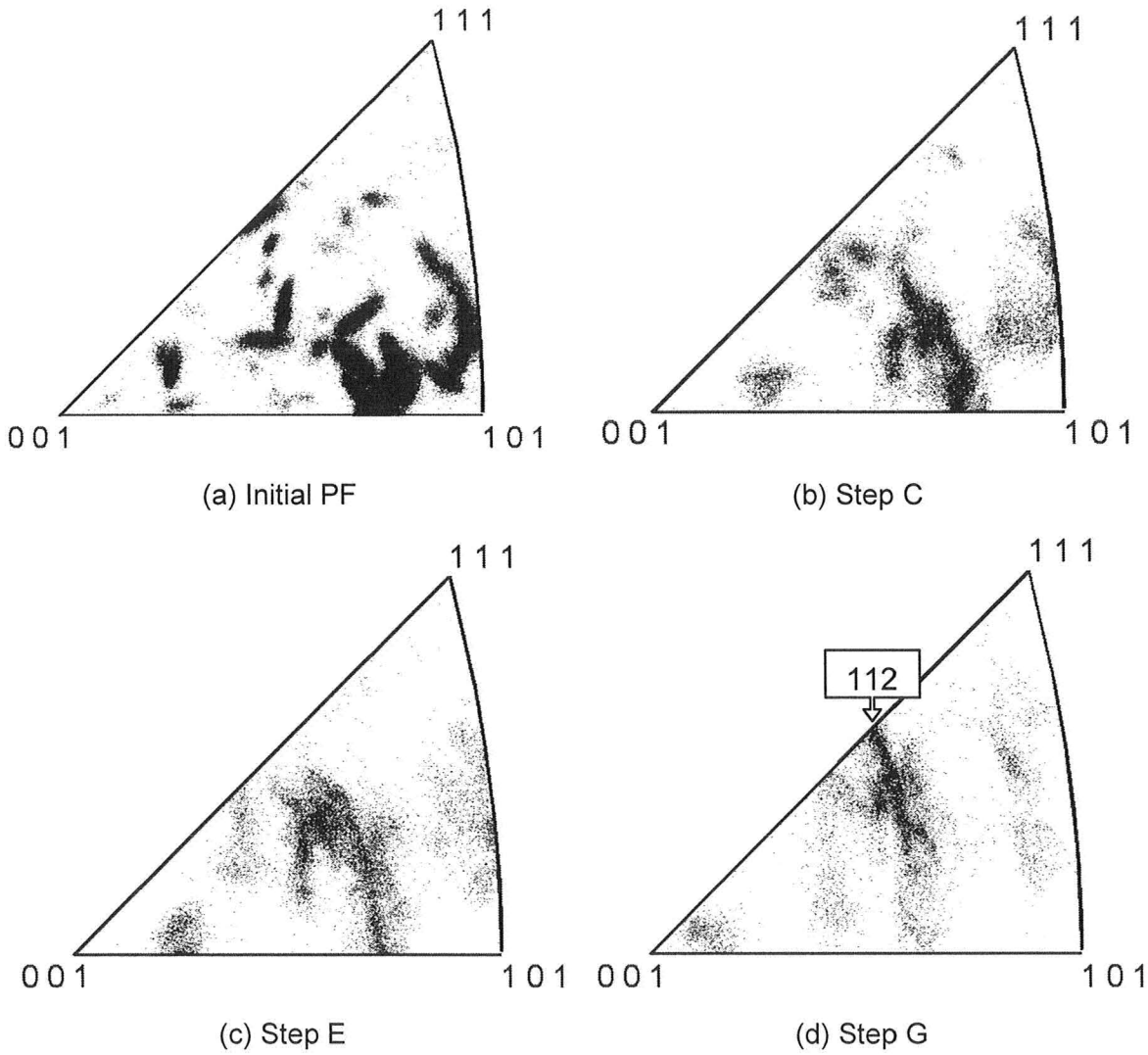

Figure 4-25 IPFs of tensile axis at different tensile steps

CHAPTER FIVE

DISCUSSION

In the current project, we have studied the mechanical response of coarse-grained samples with different grain sizes, especially their strain concentration process. We first summarize the general results, and make further analysis about the microstructure and their effect on the strain concentration processes, at sample size scale and individual grain scale. Considering one of our objectives is to verify our established models, we will compare the experimental results with the simulation results from CP-FEM and FE-TBH approaches in the second part. The comparison includes several parts: the localization position, the surface profiles, the strain mapping and the evolution of microstructure. This chapter will end with a brief critical assessment.

5.1 Microstructure Effect on Tensile responses

Grain orientation and interaction between neighbors defines the initial deformation pattern. However, the deformation pattern can also be influenced by the evolution of grain shape and orientation due to lattice spin.

5.1.1 Microstructure-deformation Relationship of G1250s

The deformation of individual grains is determined by the applied local strain and stress states which are hard to simulate using simple models. However, Taylor factors and Schmid factors of grains could present some useful information of the local deformation of individual grains. Taylor factor is determined using the total deformation of the five most activated slip systems to achieve the given deformation. Schmid factor is determined for the most activated slip systems based on the stress state of a given grain.

We calculated the cross-sectional average Taylor and Schmid factors based on the cross-sectional line scan of both layers in the thickness direction of sample G1250-2. Grey-level legend from black-to-white represents low-to-high value of either Taylor or Schmid factors (Figure 5-1(a) or (b)). Strain concentration zones appear at the cross-section with higher Schmid factors and lower Taylor factors. In addition, the strain localization path is within the region of highest average Schmid factor. This implies that grains prefer plastic deformation according to equal stress state activating simple slip system(s) inside grains. This is consistent with slip traces analysis in G1250s: inside one grain, one or two slip traces dominate the deformation.

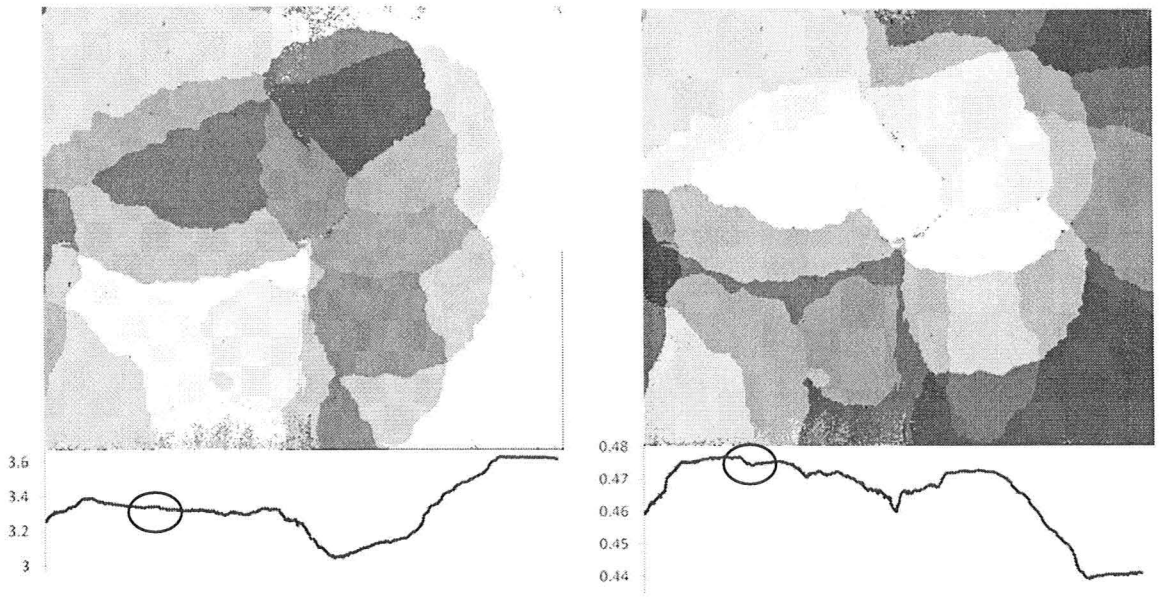

(a) Cross-section average Taylor factor (b) Cross-section average Schmid factor

Figure 5-1 Cross-section average microstructure factors: (a) Taylor factor and (b) Schmid factor; Region in circles means the highest strain concentration zone.

We first analyze the effect of initial microstructure on the beginning of plastic deformation behavior which is represented by the micro-macro Mises ratio (the ratio of local Mises strain and macro Mises strain). Overlap Micro-macro Mises ratio contour from DIC data of Side A and Side B on microstructure maps related to Schmid factor. (Figure 5-2) Large micro-macro Mises ratio fits well with the areas of high Schmid factors and small micro-macro Mises ratio relates to the low Schmid factor region. The deformation inside overlap regions of the corresponding grains in side A and B are homogeneous. The behavior of the grain boundaries are more complex, which is consistent with surface features characterization of G1250s: surface profiles change at the very beginning of deformation at boundaries and more slip traces were observed to achieve the compatibility between grains.

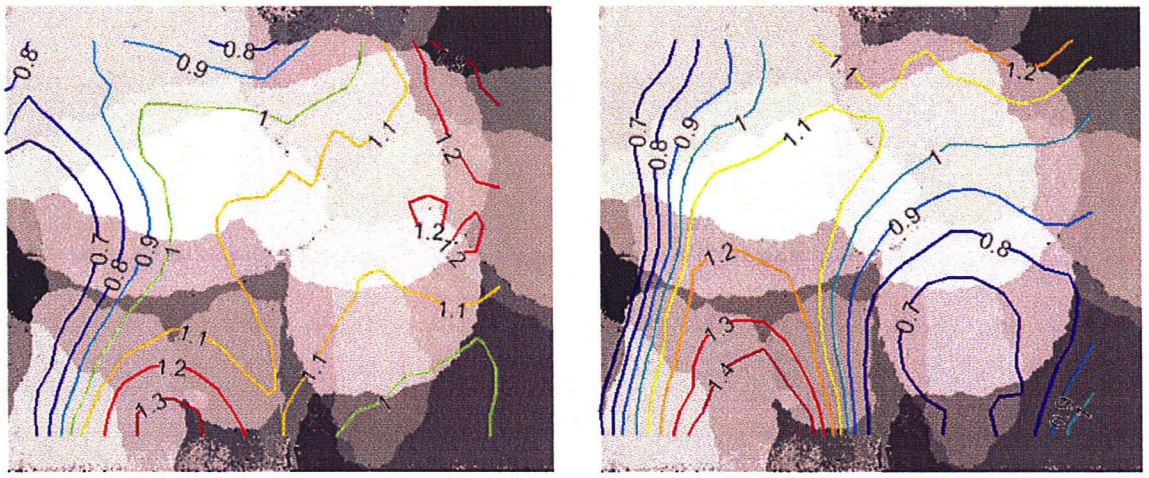

(a) Side A micro-macro Mises ratio contour (b) Side B micro-macro Mises ratio contour

Figure 5-2 Micro-macro Mises ratio contour v.s. Schmid factor

Figure 5-3 (a) and (b) present micro-macro ε_x ratio (the slope of local ε_x and macro ε_x) and micro-macro ε_y ratio (the slope of local ε_y and macro ε_y), separately. The difference of ε_y seems much smaller than that of ε_x. Grains with high Schmid factors inside strain concentration zones support large width reduction instead of elongation, which probably comes from their special orientations and edge effect. Under such orientation and boundaries conditions, activated slip systems deform more at width direction.

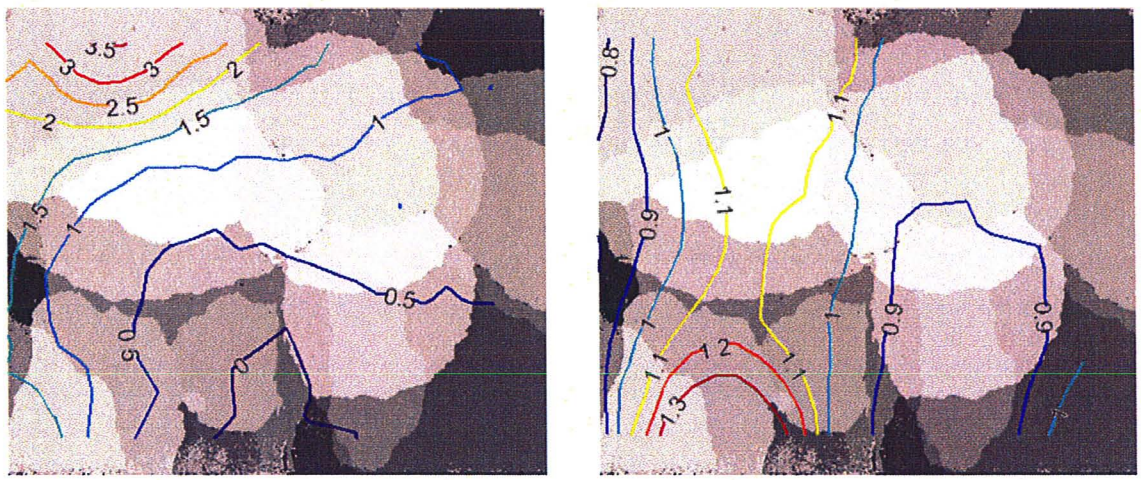

(a) micro-macro ε_x ratio, sideA (b) micro-macro ε_y ratio,sideA

Figure 5-3 Micro-macro ε_x and ε_y ratio v.s. Schmid factor

Note: ε_x and ε_x are the strain component at transverse and tensile direction, separately.

Let us now take a look at the deformation-causing evolution of microstructure. There are three final evolution directions of tensile axis: <111>, <112> and <001>. The orientation evolution of individual grains may divide into several directions (Figure 5-4). Several evolution directions, highlighted in lines with arrows originate at the same initial points.

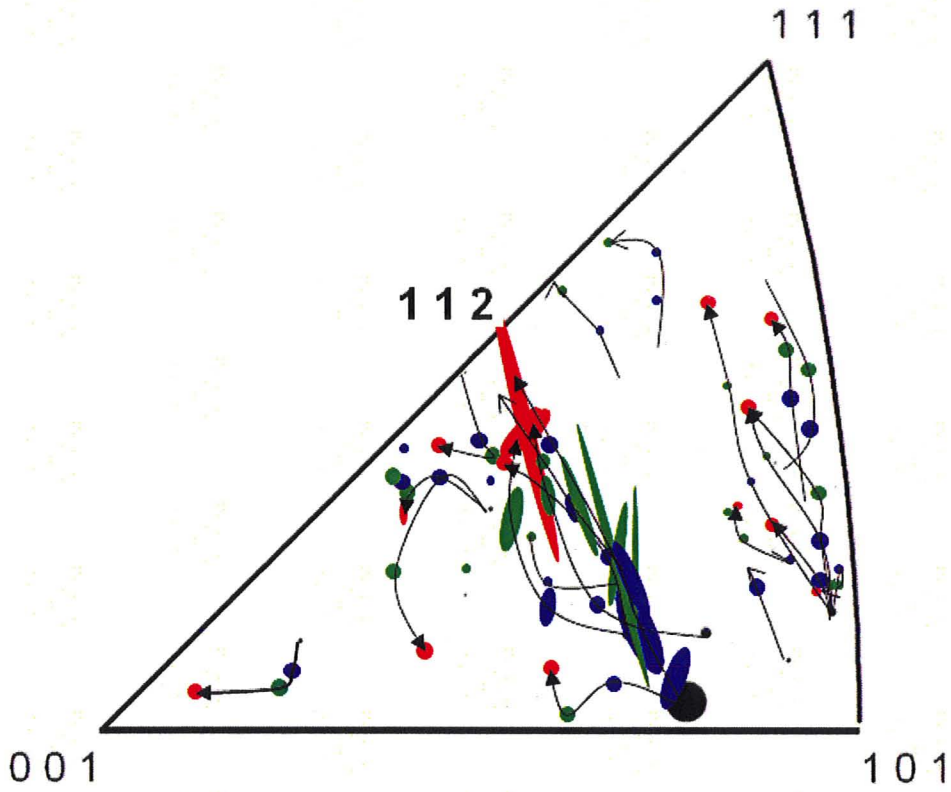

Figure 5-4 Evolution of grains in G1250-3

Note: Grain orientation evolutes following the color range of black, blue, green and red. Lines with arrow represent the evolution paths and directions.

Although experimental results based on statistical analysis for texture states no significant microstructure change until necking, grain orientation evolves evenly from the beginning of deformation until necking (Figure 5-4). This implies that microstructure evolution should be taken into account from the beginning.

We combine IPFs for the microstructure factor distribution with different orientations (Figure 5-5) with IPFs of the grain orientation of both sides of G1250-2 (Figure 5-6). According to the evolution paths described in Figure 5-4, the behavior of individual grains in specimen G1250-2 are listed:

a), In side A, Grain10-12, 14-16 and 8 (Figure 4-10) are these positions for 'hot spots'. Grain 16 is the one with highest Schmid factor among all grains. Grain 10-11, 14-15 have large evolution space to become softer related to Schmid factors. Grain 12 and 8 tend to be 'softer' and they are the ones with relative high Schmid factors.

b). In side B, Grain 5,7,8 and 10-15 (Figure 4-10) are positions for 'hot spots'. Grain 10 is the one with the highest Schmid factor among all grains. With deformation, all the other grains tend will be reoriented to these orientations which have high Schmid factors.

Grains inside the strain localization region are grains with an initially high Schmid factor and they tend to orientations with high Schmind factors. It is important to note, green grains in IPFs of tensile axis have a large IPF space to become softer.

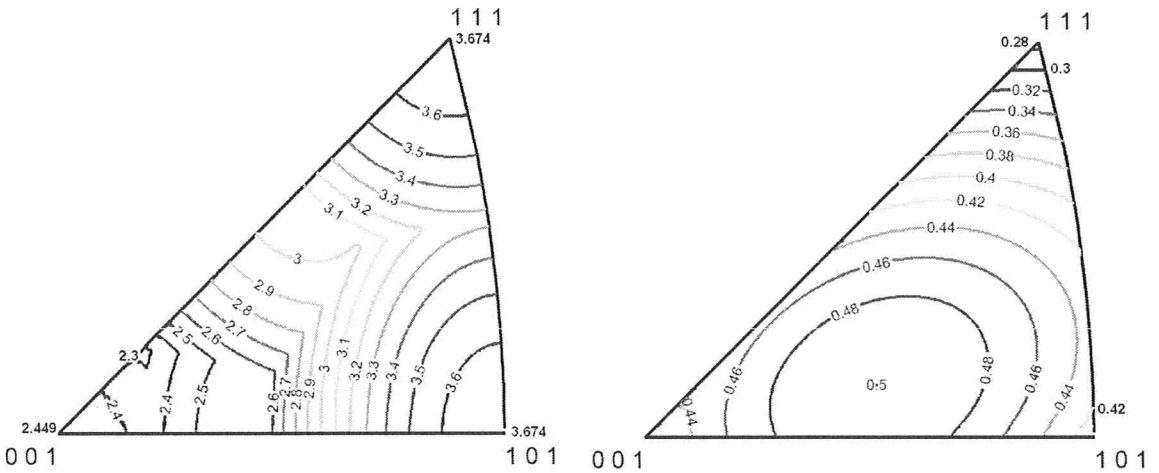

(a) Taylor factor in IPFs (b) Schmid factor in IPFs

Figure 5-5 Microstructure factor in IPFs of tensile axis

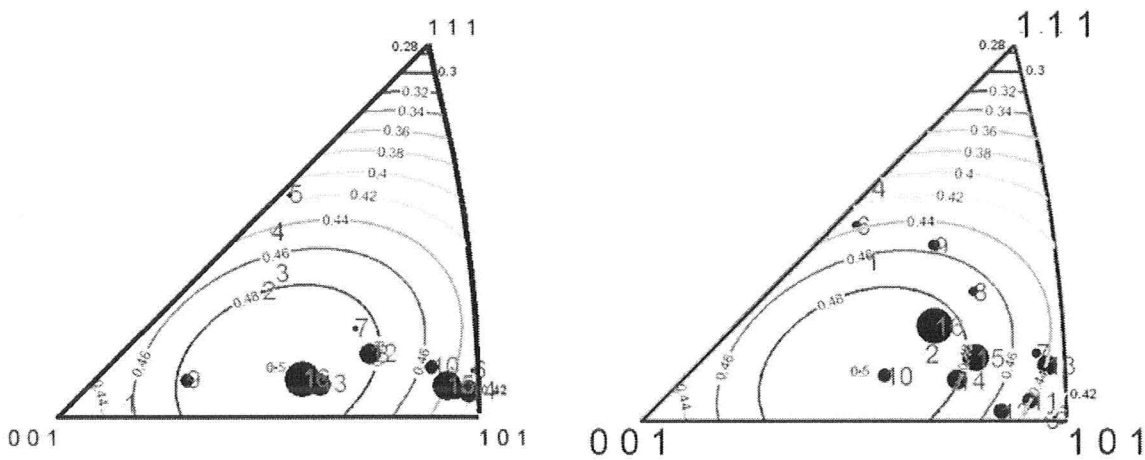

(a) Side A (b) Side B

Figure 5-6 IPFs of tensile axis of G1250-2

Considering these evolution paths, the majority of evolution paths lead to the same trend of evolution, either increasing or decreasing Schmid factors. This provides a possible explanation of why most 'hot spots' appeared at the beginning of tensile tests and keep the same positions during deformation until facture.

We can make the following observations:

a): average cross-section microstructure factor is good to predict several possible sites for strain concentration. Schmid factors are better for G1250s than Taylor factors;

b), initial microstructure strongly associates with initial deformation, and may be the determining factor: 'hot spots' occur at the area with local soft grains and soft-evolution grains;

c), grain rotates toward a certain direction and changes the relative soft and hard factors, which determine the sustained growth of 'hot spots'.

5.1.2 Tensile Response of Individual Grains

To obtain better understanding for the deformation mechanism of grains in G1250s, slip trace observation and simulation are presented in Figure 5-7. The simulation traces for the slip systems with highest Schmid factors (dotted line in Figure 5-7) were observed in grains within an error of 5°. On the other hands, one more slip traces were indentified in some grains, especially purple (close to <112>) and red (close to <001>) grains with little evolution space. This implies that the behaviors of individual grains are not fully under control by the Schmid factor. Taylor factor also is not the best parameter for indexing grain deformation as less than necessary slip systems are required to achieve the strain and stress compatibility among grains.

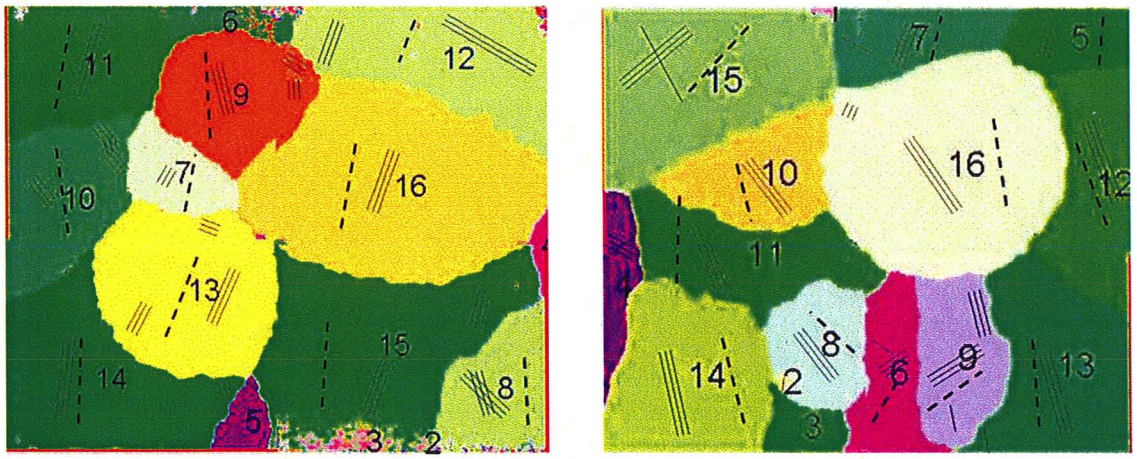

(a) Side A (b) Side B

Figure 5-7 Experimental (real lines) and simulation (dotted lines) of surface slip traces

In order to gain better understanding for the deformation processes, detailed analysis for individual grains, especially those in the strain concentration zones were carried out.

Strain partitioning of each individual grain was made using selected facet points within grains (Figure 5-8). The facet points were selected so that they would overlap with both Side A and Side B as the overlapped regions have similar stresses and strain states. The effect of boundaries between Side A and Side B was not considered.

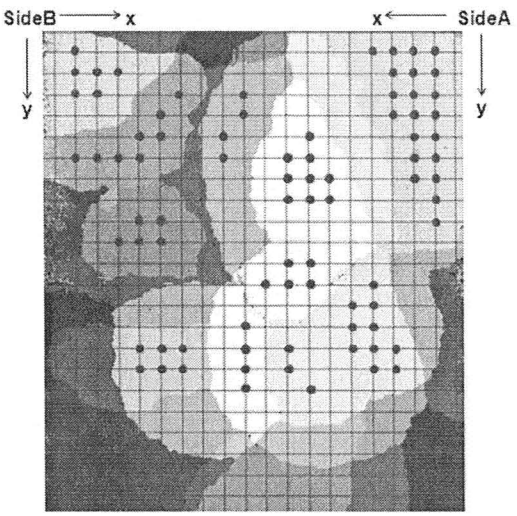

Figure 5-8 Scheme of point selection

Micro-macro Mises strain curves for individual grains are summarized as follows:

a). The behaviors of the overlap regions of corresponding grains in Side A and B are quite uniform.

b). Grain inside strain localization region (Figure 5-9(a)-(c)): Local Mises strain of these grains increases dramatically after necking. Part of region A8B14 is inside the localization zones and is the starting position for fracture. Several curves are increasing dramatically while others stop after necking (Figure 5-8(c)) at some point implying this region was torn apart since local deformation has no more continuity.

c). Grains outside localization region (Figure 5-9(d)-(f)): Local Mises strain stops increasing after localization.

d). Edge grains (Figure 5-9(a),(c),(f)): Curves for each facet in the same grain are strongly dispersed.

e). The small curvature of those curves at different strain hints above the evolution of grains. The evolution of grain orientation changes the relatively "hardness" of grains and then affects the local slope of micro-macro Mises curves.

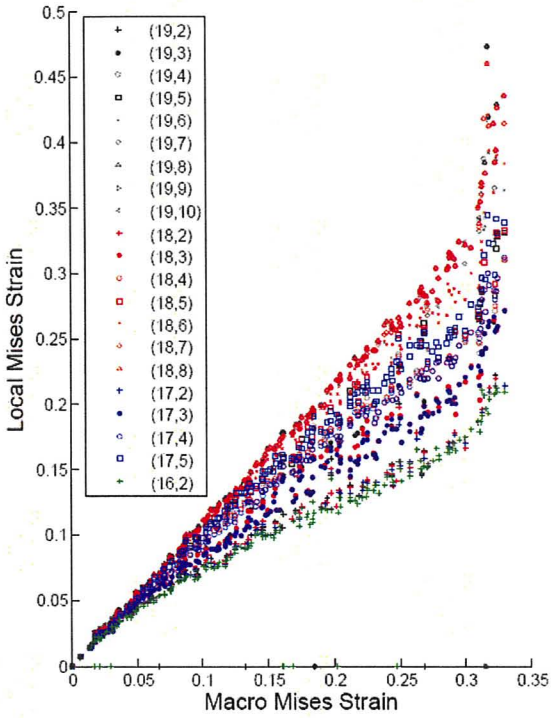

(a) A12B15

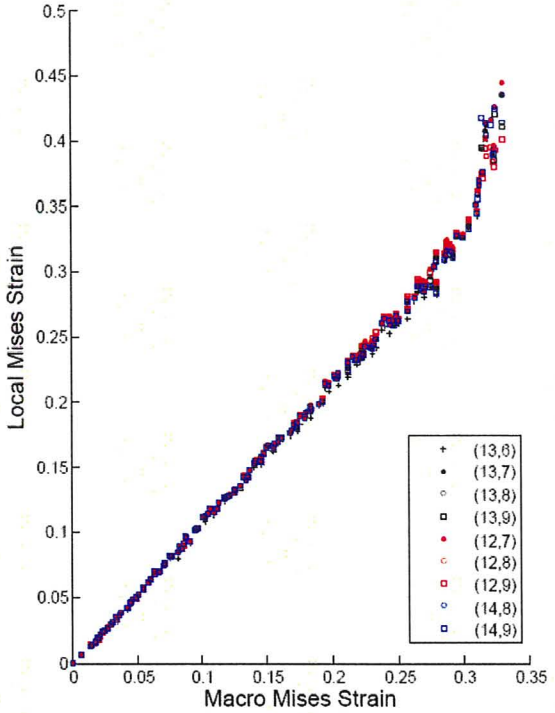

(b) A16B10

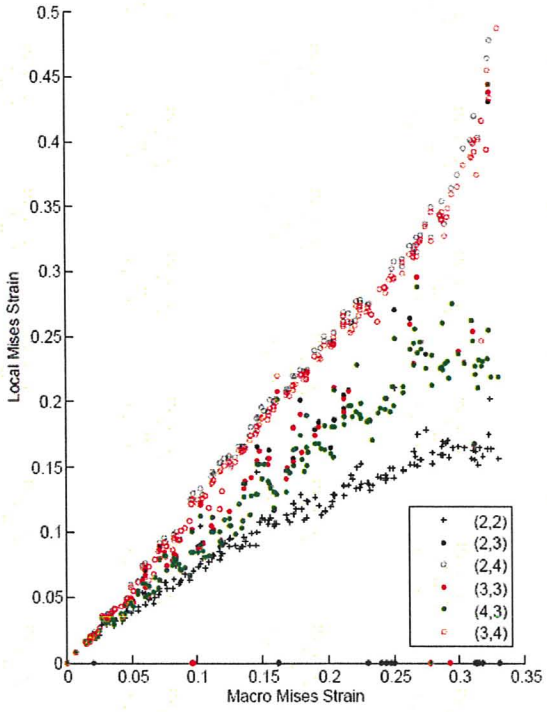

(c) A8B14

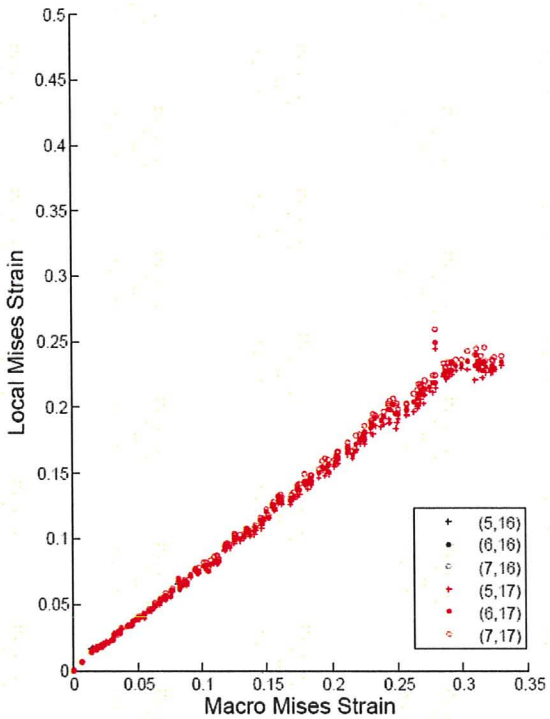

(d) A13B9

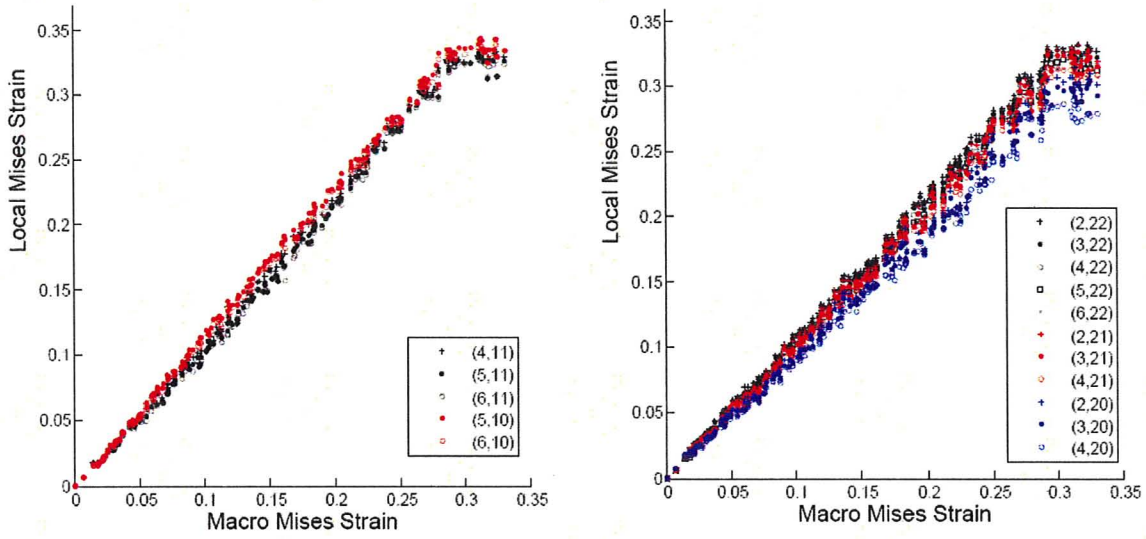

(e) A15B8 (f) A14B13

Figure 5-9 Micro-macro Mises strain of individual grains in side B of G1250-2

Note: The label in each graph is the coordinates of selected facet points in the coordinate system in Figure 5-8.

The position for these graphs are represented in form of AxxBxx, where xx is the number of grains, A and B stands for Side A and B, separately.

Complete curves for all grains are listed in Appendix.2.

No simple relationship was observation between the behavior of individual grains (i.e. micro-macro Mises ratio) and Schmid or Taylor factors. This is consistent with results of slip traces: neither one (for Schmid factors) nor five (Taylor factors) slip systems were activated inside grains.

5.1.3 Microstructure-deformation Relationship of G600s

We now switch to materials with smaller grain sizes. Cross-sectional average Taylor and Schmid factors are based on the cross-section line scan of both layers in the thickness direction of sample G600-2 (Figure 5-10(a) or (b)). Strain concentration zones appear at the cross-section with higher Schmid factors and lower Taylor factors. Compared to G1250-2, no significant advantage

of Schmid factor over Taylor factor was observed to describe strain localization path in specimen G600-2.

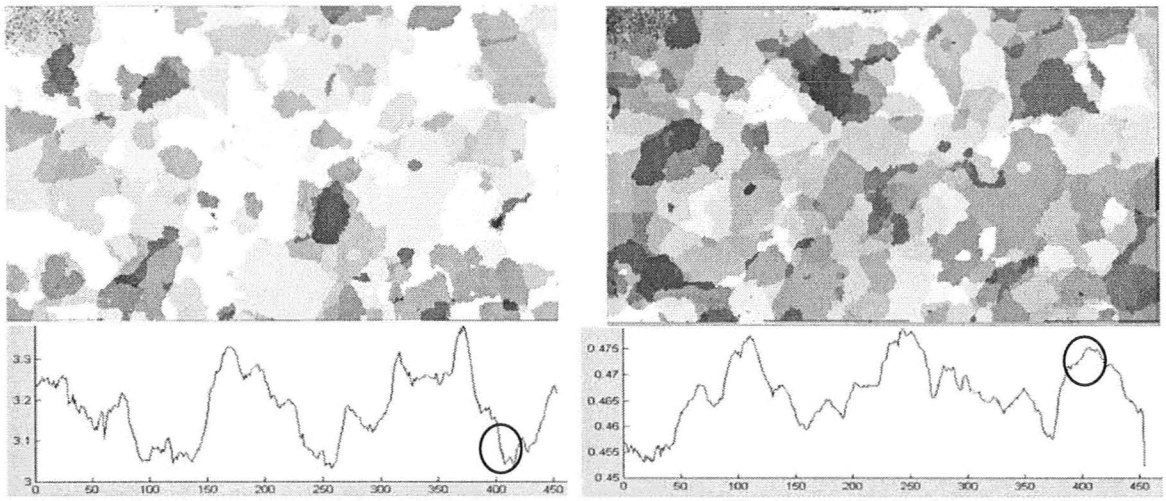

(a) Cross-section average Taylor factor (b) Cross-section average Schmid factor

Figure 5-10 Cross-section average microstructure factors: (a) Taylor factor and (b) Schmid factor; Region in circles means the highest strain concentration zone.

Figure 5-11 shows the beginning behavior though Mises strain contour overlapping microstructure grey-level images. The initial 'hot spots' settle in initial local soft regions with low Taylor factor and high Schmid factor without prefect fitting.

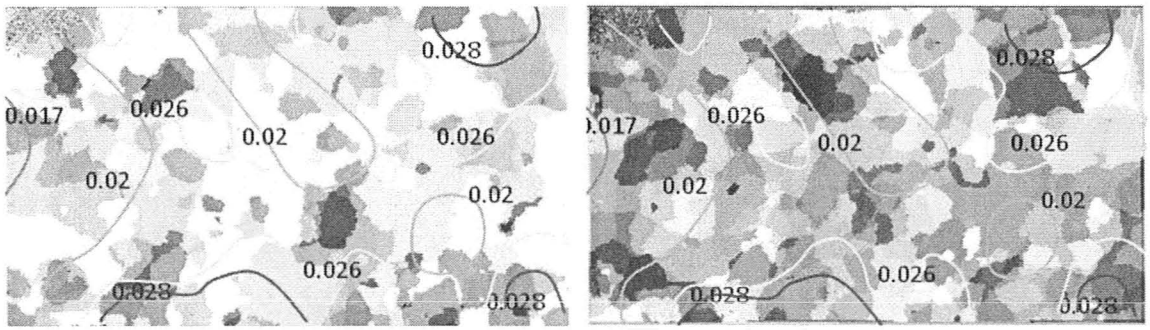

(a) Taylor-based microstructure (b) Schmid-based microstructure

Figure 5-11 Mises strain contour v.s. microstructure factors

'Hot spots' were observed to be related with the green grains in IPFs of the tensile axis (Figure 5-12). These green grains have large Taylor and Schmid factors. There are several possibilities for these green grains to be the sites for 'hot spots': a) Slip directions of the possible active systems of these grains are not the same. In most cases, the two slip systems with the largest and second largest Schmid factor are sheared in different directions so that strain compatibility with neighbors is easily achieved within these grains; b) These grains become softer with the evolution of grain orientations.

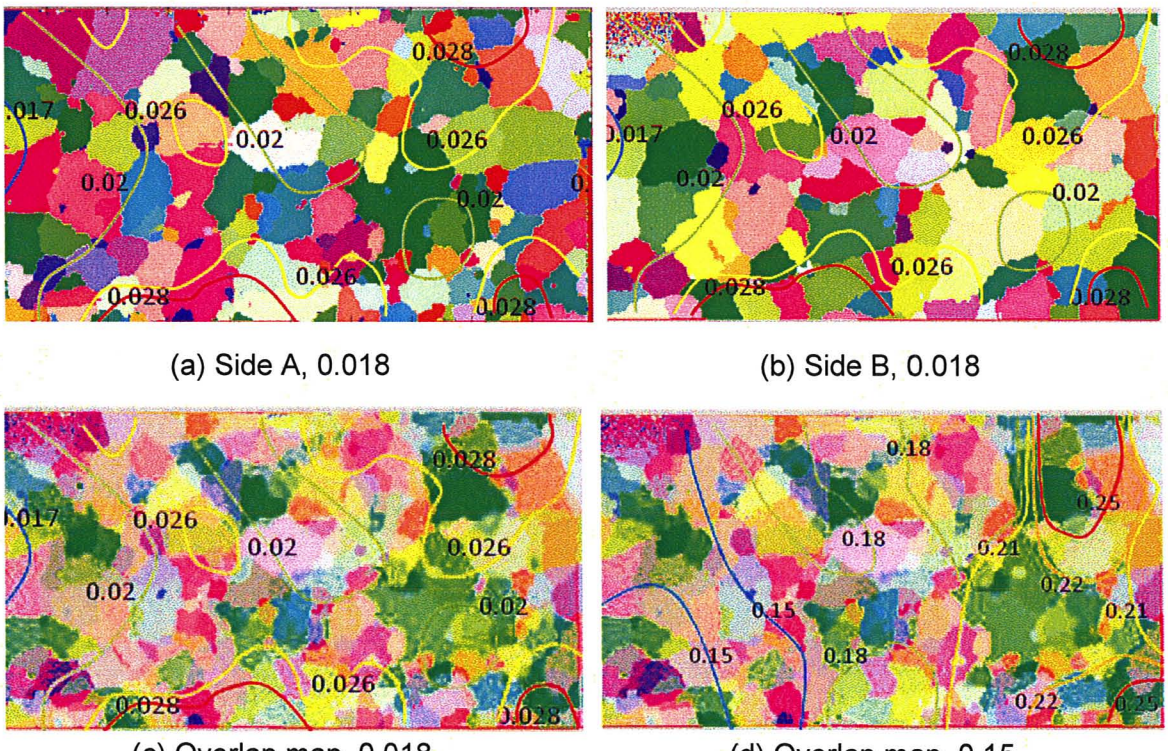

(a) Side A, 0.018

(b) Side B, 0.018

(c) Overlap map, 0.018

(d) Overlap map, 0.15

Figure 5-12 Mises strain contour v.s. IPFs of tensile axis

Note: (a)-(c) are based on the global strain of 0.018, and (d) is at 0.15 global strain.

It is clear from our study that: a). average cross-section microstructure factors (Taylor and Schmid factors have the same trend for G600s) are good to predict several possible sites for strain concentration. Although neither Schmid factor nor Taylor factor could describe the behaviors of individual grains, the

average cross-sectional Taylor factors are relatively good to present the relative "hardness" of cross-sectional area including a group of grains. b). grains with tensile direction along to <101>, are favorable positions for strain concentration.

5.2 Comparison with Simulation Results

One of the purposes of this study is to calibrate numerical models developed within our group. These microstructure-based models are developed in order to describe the major features during deformation, particularly localization paths. The simulation shown here were performed by Dr. X. Hu at McMaster University.

5.2.1 Final Morphology

Simulation results for G1250-2 obtained by CP-FEM simulation agree well with experiments for localization position and surface profiles (Figure 5-13). CP-FEM predicts well the behaviors of different oriented grains in this specimen. The same valleys and ridges are presented in both experimental and simulated results around grain boundaries. These valleys and ridges are formed due to different deformation mode between different oriented grains.

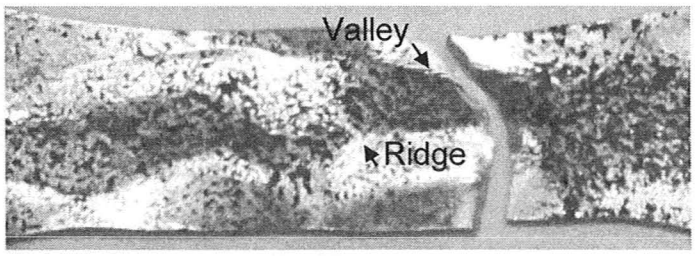

(a) Final morphology of side A

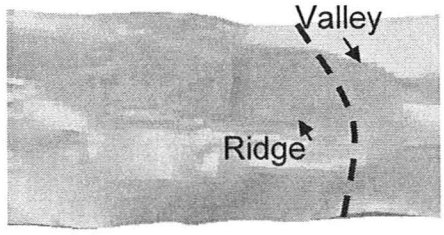

(b) Simulation of side A[86]

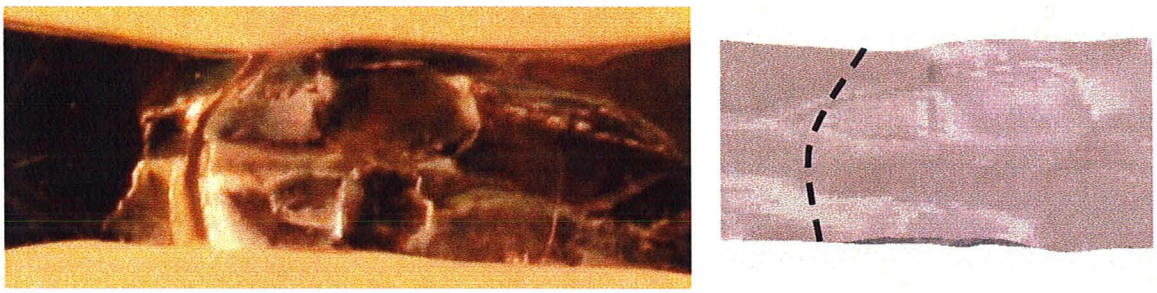

(c) Final morphology of side B (d) Simulation of side B[86]

Figure 5-13 Simulation morphology v.s. experimental results of G1250-2

Notes: in (b) and (d), contrast is from surface profiles by simulation.

Compared to CP-FEM, FE-TBH model loses more information because of its simplification of both calculation methods and assumptions. However, localized paths predicted by FE-TBH model have fairly good agreement with the experimental path which is highlighted by dotted line (Figure 5-14).

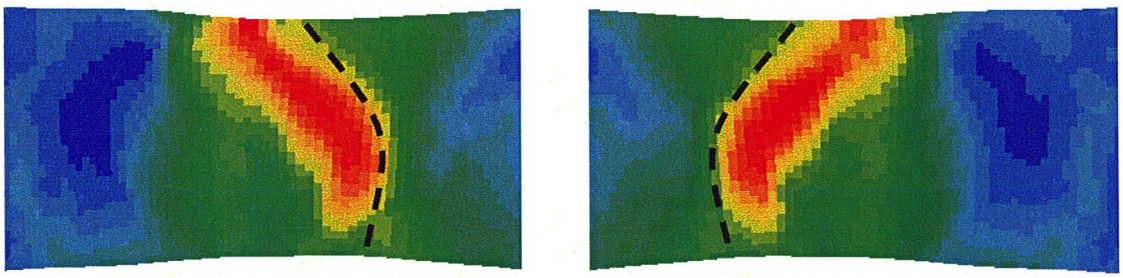

(a) Side A (b) Side B

Figure 5-14 Predictability of FE-TBH on G1250-2[86]

It is not safe to draw our conclusion on the predictability of microstructure–based models just on the comparison of G1250-2. Figure 5-15 shows surface morphology and final localized paths from CP-FEM simulation on G600-2, and the localized path across the same grains between simulation and experimental result. Careful examination was carried on the surface profiles, and simulation supports the same valleys and ridges near grain boundaries, which due to the different deformation modes for different grains.

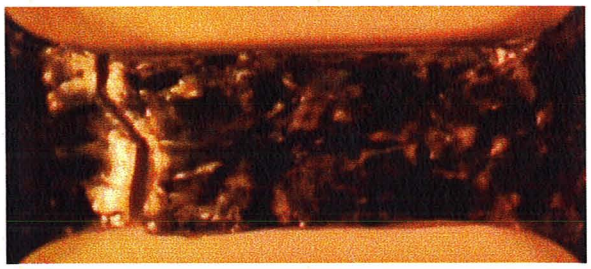

(a) Final morphology of side A

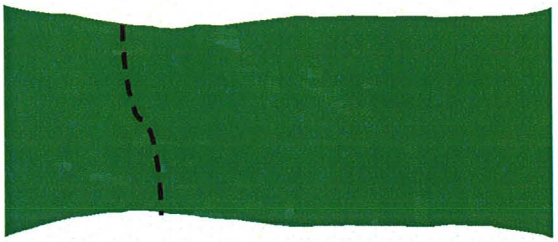

(b) Simulation of side A[86]

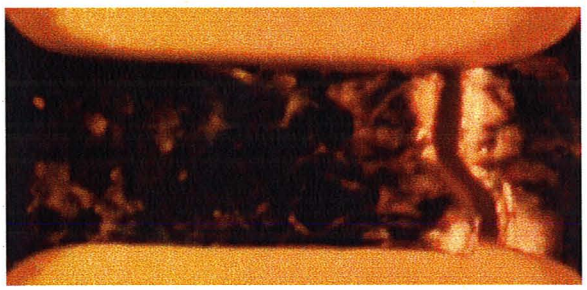

(c) Final morphology of side B

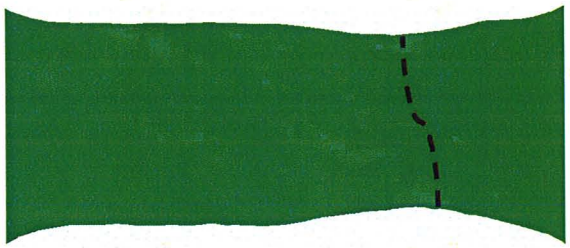

(d) Simulation of side B[86]

Figure 5-15 Simulation morphology v.s. experimental results of G600-2

Note: in (b) and (d), contrast is from surface profiles by simulation.

Slight deviation comes from the comparison of position of localization pattern predicted by FE-TBH simulation and experimental failure paths (dotted lines in Figure 5-16).

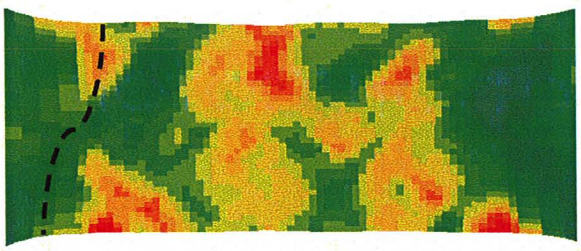

(a) Side A

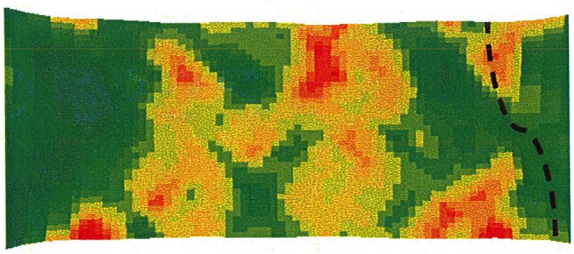

(b) Side B

Figure 5-16 Predictability of FE-TBH on G600-2[86]

5.2.2 Deformation Processes

Tensile true strain maps from experiments and simulation are used to verify the prediction accuracy of CPFEM models. Figure 5-17 lists the selective

stage strain maps, and different facet size causes the difference in local strain value but no effect on the macro strain pattern. The strain pattern between experimental results and CP-FEM simulation are the same except for a few details which may be different due to the effect of calculating facet size.

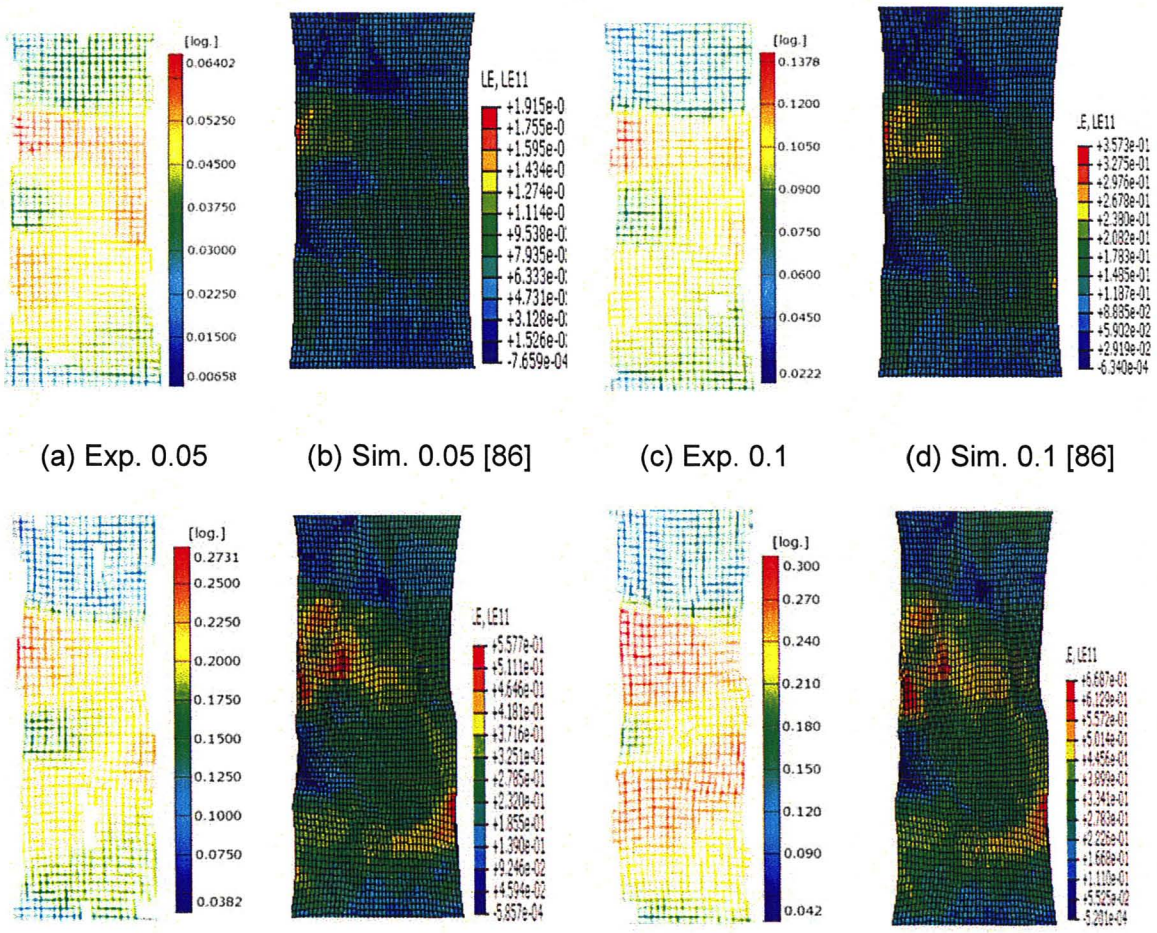

(a) Exp. 0.05 (b) Sim. 0.05 [86] (c) Exp. 0.1 (d) Sim. 0.1 [86]

(e) Exp. 0.2 (f) Sim. 0.2 [86] (g) Exp. 0.25 (h) Sim. 0.25 [86]

Figure 5-17 Comparison of strain distribution evolution between experimental and CP-FEM simulation on G1250-2

Note: Exp. and Sim. represent results from experiments and simulation, respectively. Numbers are the global tensile true stains.

Figure 5-18 states the selective strain mapping for specimen G600-2, confirming the good predictability with CP-FEM of strain concentration behaviors. Correlation of strain concentration regions at a large strain is better than the one

at small strain. In Aramis, large calculating facet size compared to relative small grain size results in extinct grain boundaries effect. Therefore, some small and sporadic high local strain regions are ignored in Aramis mapping because of the average value of each calculating facet.

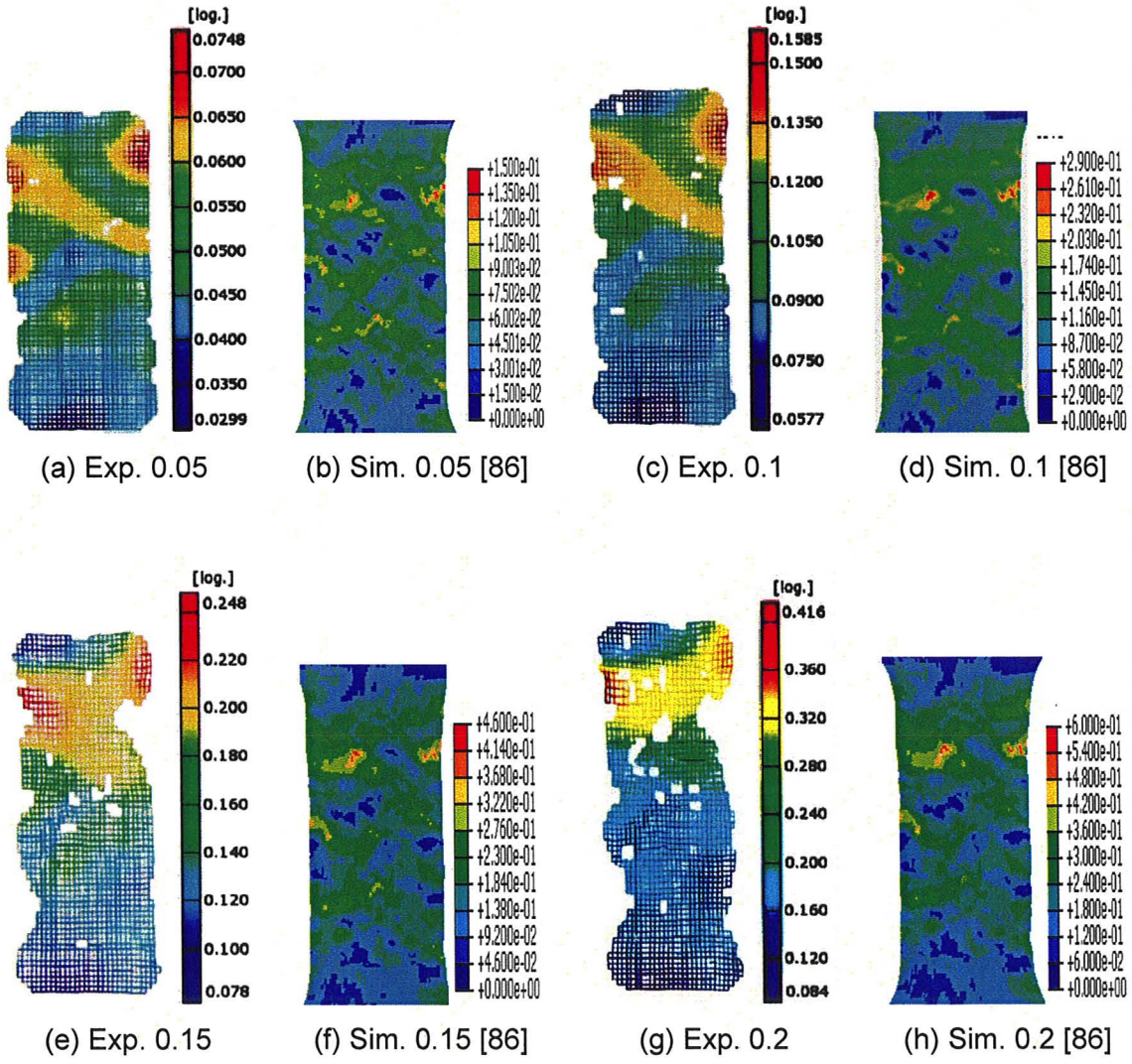

(a) Exp. 0.05 (b) Sim. 0.05 [86] (c) Exp. 0.1 (d) Sim. 0.1 [86]

(e) Exp. 0.15 (f) Sim. 0.15 [86] (g) Exp. 0.2 (h) Sim. 0.2 [86]

Figure 5-18 Comparison of strain distribution evolution between experimental and CP-FEM simulation on G600-2

Note: Exp. and Sim. represent results from experiments and simulation, separately. Numbers are the global tensile true stains.

5.2.3 Microstructure Evolution

From experimental results, it was revealed that: a) tensile axis in crystal coordination rotates toward <0 0 1>, <1 1 2> and <1 1 1>; b) the distribution of grain orientations are more random compared to the initial state. Figure 5-19 presents the comparison of experimental and CP-FEM simulation on the evolution of grain orientations with increasing deformation strain in specimen G1250-3. During deformation, simulation results state that orientations are relatively randomly distributed and concentrated at positions of <1 1 2> and <1 0 1>. Although evolution paths in simulation deviate from its real paths and grain division are different with experimental CP-FEM proves reasonably good evolution path for grain near <1 0 1>, which is in fact the most important orientation in our tensile deformation.

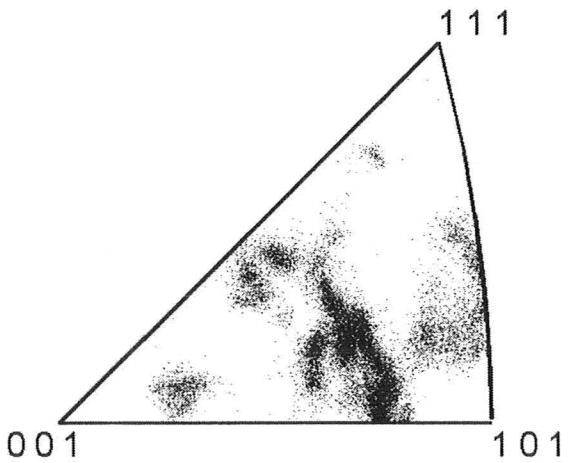

(a) Exp, 0.07

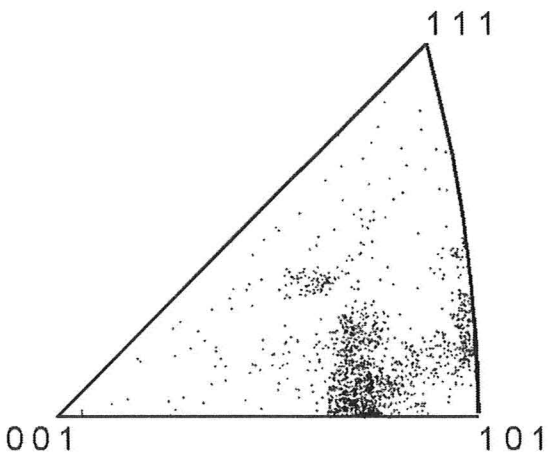

(b) Sim, 0.07

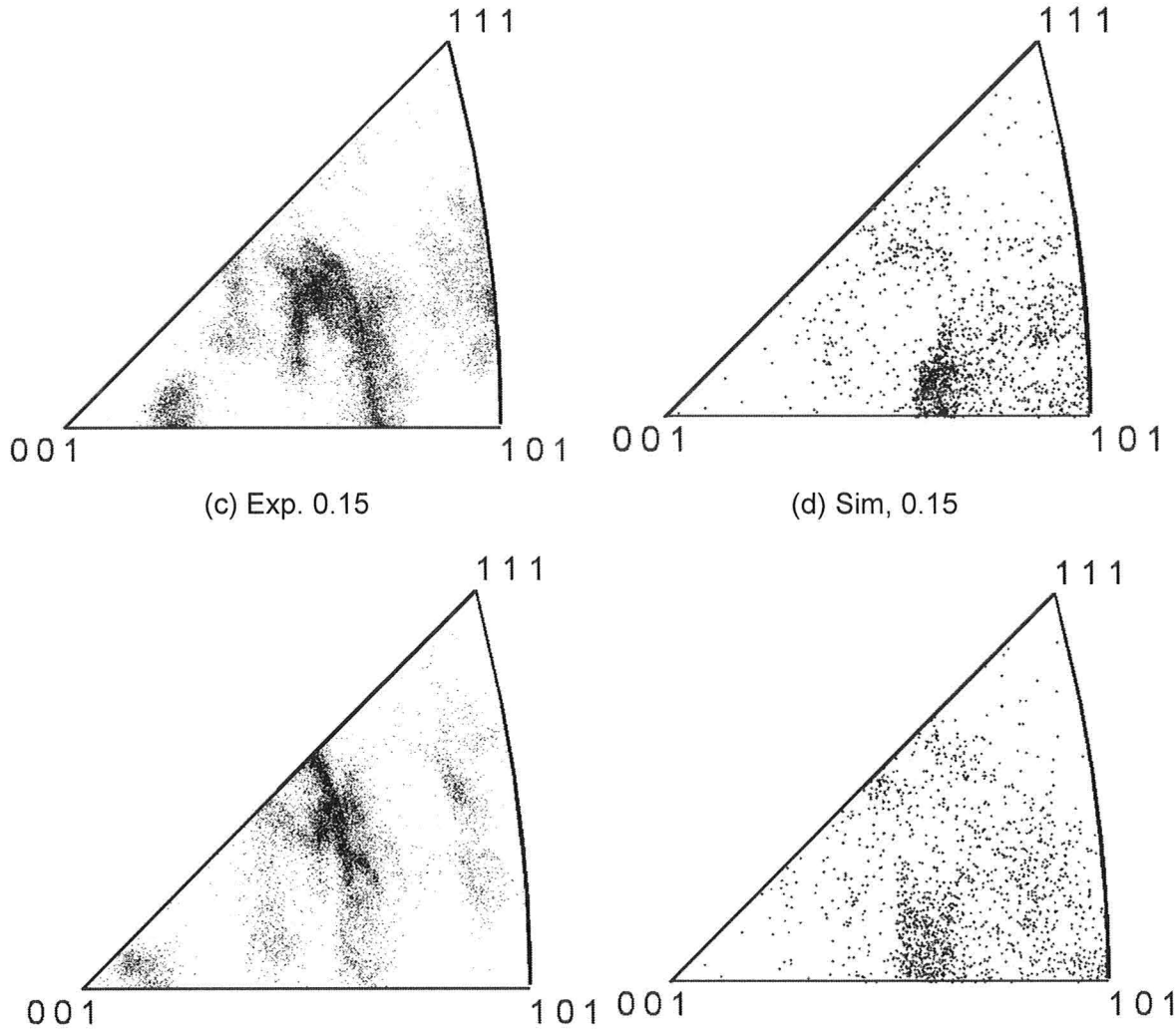

Figure 5-19 IPFs of tensile axis with specimen G600-2

Notes: Exp. and Sim. short for results from experiments and simulation. Value indexes the global tensile true stain. Simulation data for (b), (d) and (f) are from [86].

5.3 Critical Assessment

Tensile bars with a large grain size always have a short necking process and no significant facture morphology to show the width and thickness reduction.

Strain localization processes are not determined according to the engineering stress-strain curves, equation 2-3 mentioned in section 2.1.3 or the criterion that localization happens when the ε_x-ε_y ratio changes. All these criteria are consistent with each other in homogeneous materials; however, not all of them work for the coarse-grained tensile bars. The key feature of strain localization is deformation concentration in a narrow area. We define strain localization according to these point-to-point local-global strain curves: strain localization regions own dramatically increasing strain after a certain stage while deformation stops at all other regions after such a stage.

The average cross-sectional microstructure factor is good to predict several possible sites for strain concentration. Tensile behaviors of individual grains however could not be described by simple microstructure factor, which implies that different deformation modes exist due to grain interaction. Mentioned here, deformation behaviors of coarse-grained tensile bars are quite different from the ones with normal grain size. For example, ε_x-ε_y ratio for coarse-grained bars is around 0.2-0.25 compared to 0.45-0.5 for sheets with normal grain size.

Considering the properties of slip systems and the evolution paths for grains, green grains, in which tensile axis is close to <1 0 1>, are the favored sites for strain localization.

CP-FEM and FE-TBH models could capture major features of strain localization behavior, especially stain localization paths. For these simplified models, a lot of deformation details are ignored. Generally speaking, CP-FEM has better prediction accuracy than FE-TBH. However, FE-TBH offers reasonable results at greatly reduced computational time.

CHAPTER SIX

CONCLUSIONS

Based on previous study, conclusions are drawn as follows:

Thermal-mechanical treatment (rolling + annealing) was designed to get a coarse-grained structure. Due to the symmetry of the rolling procedure, a two-layer grain structure was achieved, including homogeneous bulk discoid grains and surface fine grains. Grain size reduces with increasing pre-deformation ratio and grain size increases dramatically for thickness reduction less than 6%.

Two-side EBSD maps portray this two-layer grain structure. Recrystallization grains prefer $\{001\}$ and $\{112\}$ as the rolling surface, $<110>$, $<3\bar{1}0>$ and $<63\bar{4}>$ parallel to rolling direction. These orientations are closed to R-Cube, S and H texture components of these ten major components in aluminum.

Tensile tests performed on samples with different grain sizes reveal the following points: (a) Coarse-grained specimens have shorter necking processes. (b) Good Hall-Petch relationship exists between yield strength and grain size which implies that the initial boundaries affect how grains adjust themselves to fit with their neighbors. (c) Different UTS values give the effect of oriented grains. (d) Different elastic-plastic transition areas of specimens with similar grain sizes can indicate that grain orientations do affect the beginning of plastic deformation, even at the start of deformation.

Strain distribution evolution maps present the special deformation processes of coarse-grained samples: 'hot bands' nucleate at a very earlier stage of deformation and most of them keep sustain growth throughout most deformation stages. Two-surface strain maps reveal that grains belonging to different layers work together for deformation.

Local-global strain curves provide evidence for strain localization: strain localization regions can be attributed to dramatically increasing strain after a certain stage while deformation stops at all other regions after such a stage.

In-situ tensile test combined with EBSD scans gives the following results on the evolution of grains: (a), the distribution of grain orientations becomes more random with increasing strain. (b), division inside grains are observed in parts with different neighboring grains. (c), lattice rotates to achieve deformation axis closer to <001>, <112> or <111>.

When we link the tensile processes with the initial microstructure, we find the following: (a) the average cross-sectional microstructure factor is good to predict several possible sites for strain concentration as strain concentration zones prefer the cross-section with higher Schmid factor and lower Taylor factor. (b) initial microstructure is strongly associated with the initial deformation and may actually be its determining factor: 'hot spots' occur at the area with local soft

grains and soft-evolution grains; (c), grain rotates toward certain direction and changes the relative "hardness" of grains, which determine the sustained growth of 'hot spots'; (d), those grains with <101> close to tensile direction are favored sites for strain concentration.

APPENDIX.1 CORRECTION FOR EXPERIMENTAL RESULTS OF EBSD SCANNING

Four main sources of error for grain orientations with a large area 'Beam Scan' result from:

(a). Error caused by large area scan (ε1): leads to some misorientation of grains near the border of the scanning area because of the nature of the electron beam, following detailed discussion about such 'edge effect'.

(b). Error from sample alignment (ε2): caused by the error within the frame of reference regarding to the misorientation angle between sample edge and horizontal direction. Careful experimental operation could reduce this angle to be less than 0.5°, causing the first Euler angle φ_1 to be less than 0.5°. Therefore, ε2 < 0.5°.

(c). Error from holding samples for double surface scanning (ε3): caused by the different thickness of SEM tape is less than 0.05mm in general. Then, the second Euler angle φ should be less than 0.3° considering the gauge length of bars. The conclusion is ε3 < 0.3°.

(d). Error from stage tilt: this error was ignored the in this project, this error mainly effects the size of the scanned area.

The orientation of edge grains is not accurate because of the natural curvature of the electron beam when running the large area scan. However, it is reasonable to assume that the orientation of the grain in the central area is precise and the curvature of the electron beam is center symmetric. To demonstrate this idea, three EBSD scans were set up in which the center of one scan is the edge of other two.

Scan I should be on the top of scan II with some overlaping region, which actually is the center region of scan III (Figure A-1(a)-(c)). According to our

assumption the curvature of the electron beam is symmetric to the center point, the average orientation of the overlap region between scan I and scan II should diminish the error caused by the vertical curvature although it may leave the error caused by horizontal curvature.

Randomly choose three grains (grain 1, grain 2 and grain 3) in these three scans and then draw their crystal orientations (Figure A-1(d)-(e)), respectively. The crystal orientation of grains in scan III is some kind of mean orientation between scan I and II at vertical direction, while at horizontal direction, grain orientation in scan I and II are the same and scan III has slight difference. To sum up, the real orientation of the overlap area (i.e. scan I and scan II) is the average between two scans.

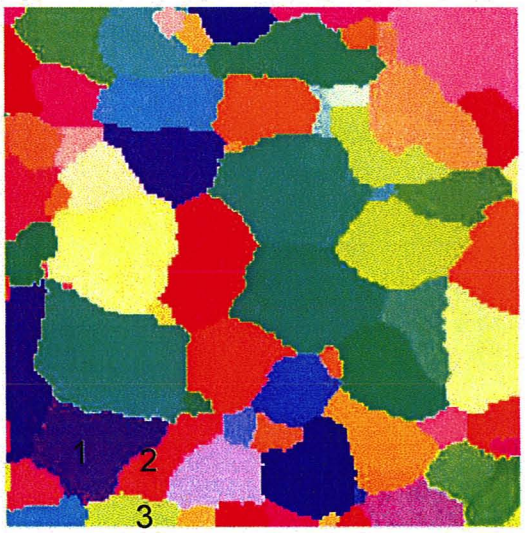

(a) IPF mapping of scanning I

(b) IPF mapping of scanning II

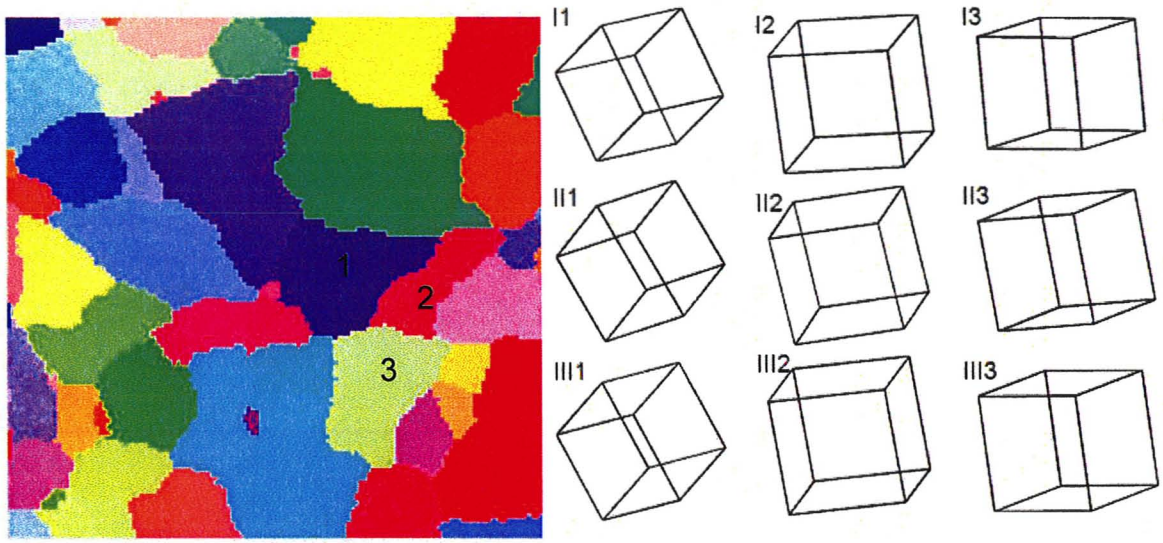

(c) IPF mapping of scanning III (d) (e) (f)

Figure A-1 IPF of transverse axis of three set-up scans

Quantity analysis is presented in Table A-1. Misangles of the same grain between different scans were calculated. We noticed that the difference between scan I and II is quite large, over 5°, which was the driving force for us to discuss this problem here. Notice here, misangle of the mean orientation of scan I and scan II with scan III is around 2.5°, probably caused by the horizontal curvature of electrical beams, especial for grain 1.

Table A-1 Misangle with different scans*

Grains	Misangle of I and II	Misangle of I and III	Misangle of II and III	Misangle of the average (I, II) and III
1	5.50°	3.53°	3.97°	2.56°
2	5.23°	3.19°	3.89°	2.36°
3	5.67°	3.48°	3.89°	2.36°

Notes: How to calculate misangle and average orientation will be discussed in details as following.

Edge grains such as grain 1 with comparable large error could be modified twice, from the vertical direction as well as the horizontal direction. Therefore, the

error caused by large area scanning could be reduce to around 2° after doing the average of all edges. Moreover, we moved the beam center a slightly higher for top scan and a slightly lower for the bottom scan to give better accuracy of these edge grains without modification.

Considering all scanning errors the total error from scanning could be

$$\varepsilon = \sqrt{\varepsilon_1^2 + \varepsilon_2^2 + \varepsilon_3^2 + \varepsilon_4^2} \approx 2.1° \qquad \text{A-1}$$

Adding another 0.5° error coming from the index accuracy of Kikuchi patterns from the TSL software the total precision of orientation is 2.2°, which is fairly good to describe mechanical properties of oriented grains.

Following is how we wrote codes for modifying the orientation of edge grains. The principle of such modification is to calculate the average orientation between the corresponding grains in the overlap area of two scans. To achieve this goal, following steps are needed to be done:

(a). calculate the misorientation angle between the neighboring data points in the same EBSD mapping along vertical and horizontal direction. Misorientation is defined as a translate matrix **Γ**, or described by a rotation axis **r** with components r_x, r_y, r_z and a rotation angle ω[87]. Shown in Equation A-2, the cosine of misangle ω is half value of the trace of **Γ** minus 1.

$$\Gamma = \begin{pmatrix} (1-r_x^2)\cdot\cos\omega + r_x^2 & r_x\cdot r_y\cdot c + r_z\cdot\sin\omega & r_x\cdot r_z\cdot c - r_y\cdot\sin\omega \\ r_x\cdot r_y\cdot c - r_z\cdot\sin\omega & (1-r_y^2)\cdot\cos\omega + r_y^2 & r_y\cdot r_z\cdot c + r_x\cdot\sin\omega \\ r_x\cdot r_z\cdot c + r_y\cdot\sin\omega & r_y\cdot r_z\cdot c - r_x\cdot\sin\omega & (1-r_z^2)\cdot\cos\omega + r_z^2 \end{pmatrix} \qquad \text{A-2}$$

When calculating **Γ**, the symmetry of fcc lattice must be considered. Given the orientation **g= [x, y, z]**, equivalent orientations can be found: (1) switch the position of those three components such as x_x, x_y, x_z, totally $C_3^2 = 6$; (2) the original one and reverse the direction of any of the three components, total 3+1= 4; (3) consider the center symmetry of all those orientation mentioned before,

2*(6*4) = 48. The orthogonal matrices $\mathbf{S}_i$ (i=1,…,24) for (1) and (2) are listed in programs and use negative $\mathbf{S}_i$ for (3) to improve the calculation speed. Obviously, the smallest misangle is the one we want, in other words, we try to find the maximum cosω among those 48 values.

In conclusion, two orientations are given in the form of g_1 and g_2, which could be translated from the original Euler angles (φ_1, φ, φ_2) using Equation A-3.

$$g = \begin{pmatrix} \cos\varphi_1 \cdot \cos\varphi_2 - \sin\varphi_1 \cdot \cos\varphi \cdot \sin\varphi_2 & -\cos\varphi_1 \cdot \sin\varphi_2 - \sin\varphi_1 \cdot \cos\varphi \cdot \cos\varphi_2 & \sin\varphi \cdot \sin\varphi_1 \\ \sin\varphi_1 \cdot \cos\varphi_2 + \cos\varphi_1 \cdot \cos\varphi \cdot \sin\varphi_2 & -\sin\varphi_1 \cdot \sin\varphi_2 + \cos\varphi_1 \cdot \cos\varphi \cdot \cos\varphi_2 & -\sin\varphi \cdot \cos\varphi_1 \\ \sin\varphi \cdot \sin\varphi_2 & \sin\varphi \cdot \cos\varphi_2 & \cos\varphi \end{pmatrix} \quad \text{A-3}$$

Their misangle is generally given in Equation A-4.

$$\omega_d = \cos^{-1}\{\frac{1}{2}(\max_{j=1,J}(L_j \cdot g_1 \cdot g_2^T) - 1)\} \quad \text{A-4}$$

(b). find the data points belonging to the same grain: in our codes, different grain indexes denote the corresponding points belonging to different grains. Figure A-2 shows the scheme to find the correct grain index for each point.

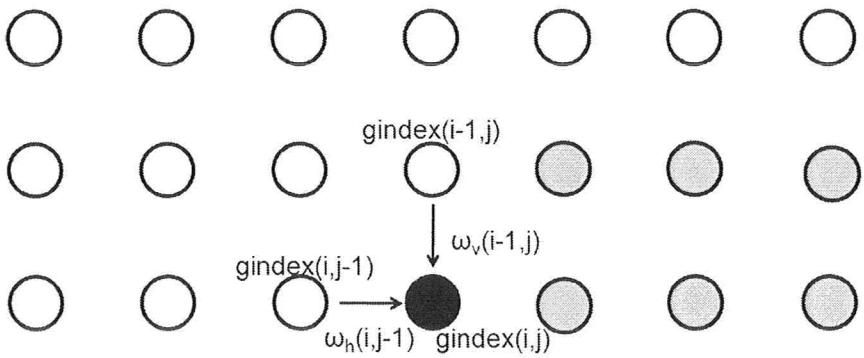

ω_v(i-1,j) < θ → gindex(i,j) = gindex(i-1,j)
ω_h(i,j-1) < θ and gindex(i,j) ≠ gindex(i,j-1)
→ find (gindex(i,j) = gindex(i,j-1)) = min(gindex(i,j),gindex(i,j-1))
ω_v(i-1,j) >= θ and ω_h(i,j-1) < θ → gindex(i,j) = gindex(i,j-1)
ω_v(i-1,j) >= θ and ω_h(i,j-1) >= θ → gindex(i,j) = newindex

Figure A-2 Scheme of finding correct grain index

In which, ω_v and ω_h are misangles between two neighboring points along vertical and horizontal direction, separately. It is easy to reach that the next point will choose the same grain index with its neighbor if the misangle is less than the critical value θ. Otherwise a new grain index should be set. One special case, grain index must be renewed if its top and left neighbors are actually in the same grain but with different grain indexes.

(c) manually input the corresponding grains in the overlap area of the two scans.

(d) calculate the mean orientation[88]: Mean orientation **g** is the mass center of a cloud of orientations $\mathbf{g}^{(k)}$ and the mass center is on the basis of a minimization of the metric distances between the mean orientation with each point. There are many different ways to define the distance d_k, here we chose the metric distance as twice of sin(ω/2):

$$d_k^{\,2} = 4\sin^2(\frac{\omega}{2}) = 3 - trace(g^{(k)}g) \qquad \text{A-5}$$

For a given set of orientation $\mathbf{g}^{(k)}$ (k=1,…,N),mean orientation **g** is defined as the minimum of the sum of d_k over k:

$$\min(3-(1/N)\sum_{k=1}^{N}\sum_{i,j} g_{ij}^{(k)} g_{ij}) \qquad \text{A-6}$$

Mathematically, use Lagrange multiplier method, we need to find matrix **M**:

$$(1/N)\sum_{k=1}^{N} g_{lm}^{(k)} = M_{lm}, \forall l,m \qquad \text{A-7}$$

Then get the matrices **N**, $\mathbf{N}^2 = \mathbf{M}\mathbf{M}^T$. Finally, obtain the mean orientation:

$$\mathbf{g} = \mathbf{N}^{-1}\mathbf{M} \qquad \text{A-8}$$

APPENDIX.2 MICRO-MACRO MISES STRAIN CURVES FOR INDIVIDUAL GRAINS IN G1250-2

Strain partitioning of each individual grains was made using selected facet points within grains (Figure 5-8). Micro-macro Mises strain curves of each selected facet point inside grains are listed as follows. The label in each graph is the coordinates of selected facet points in the coordinate system in Figure 5-8. The positions for these graphs are represented in the form of AxxBxx, where xx is the number of grains, A and B stands for Side A and B, separately.

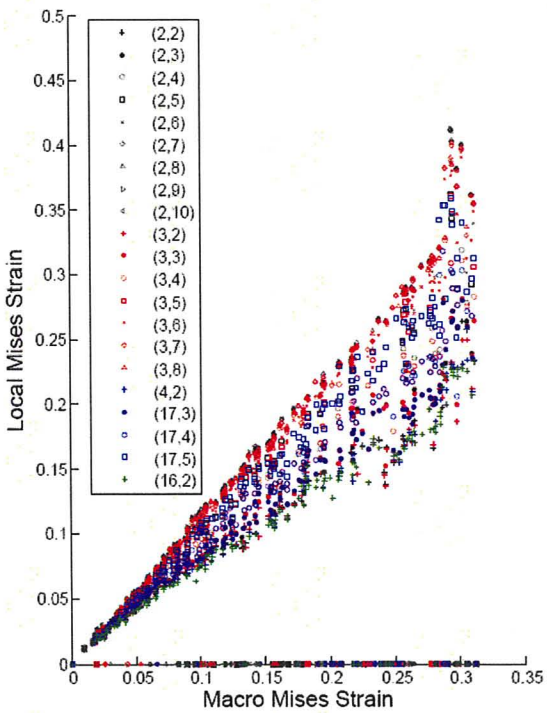

(a) Side A, A12B15

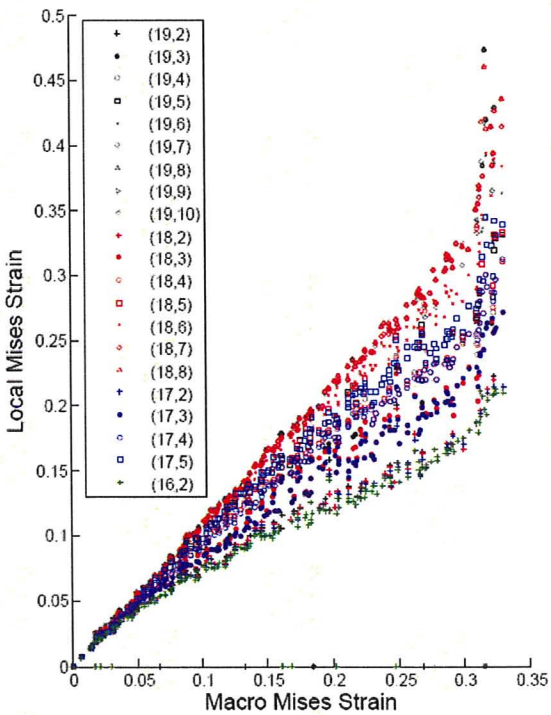

(b) Side B, A12B15

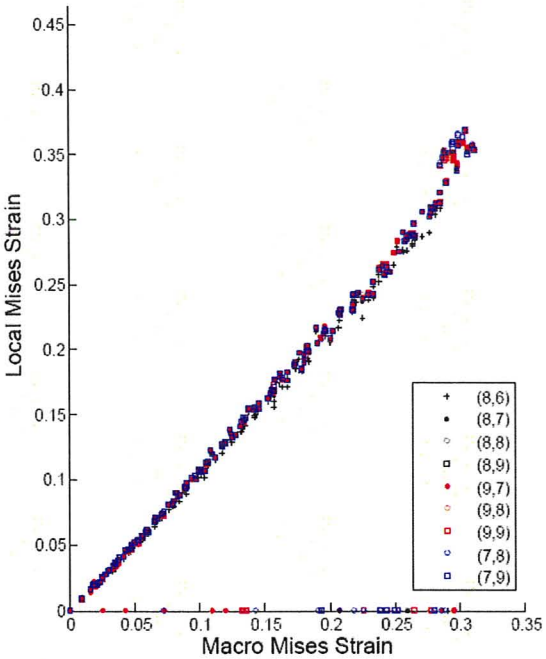

(c) Side A, A16B10

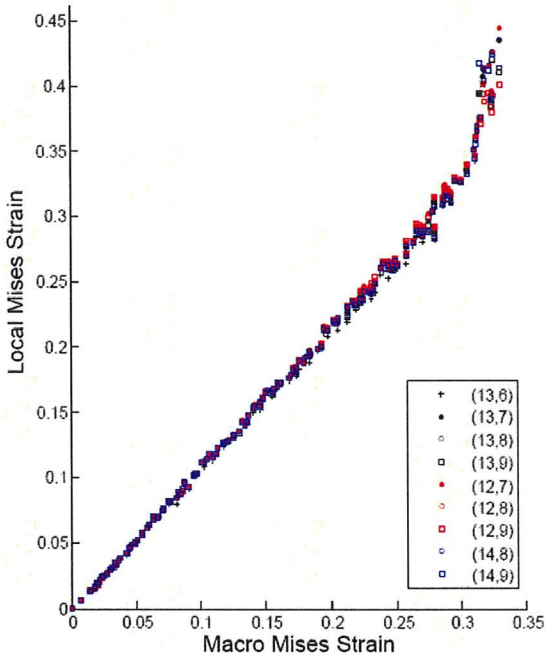

(d) Side B, A16B10

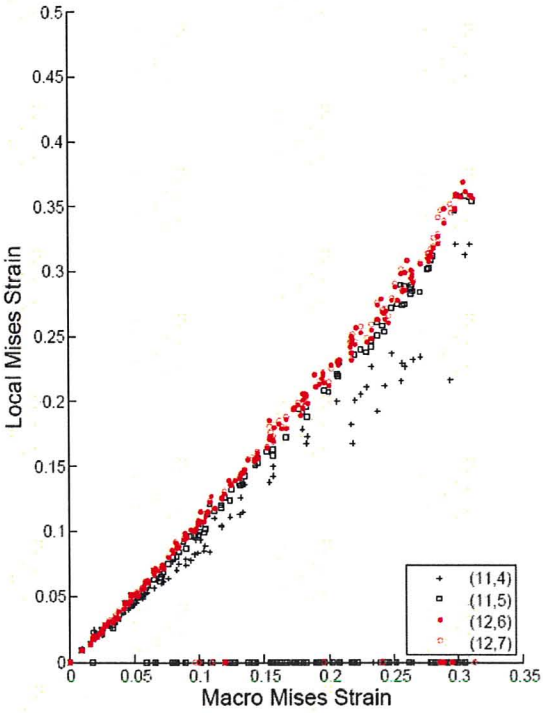

(e) Side A, A16B11

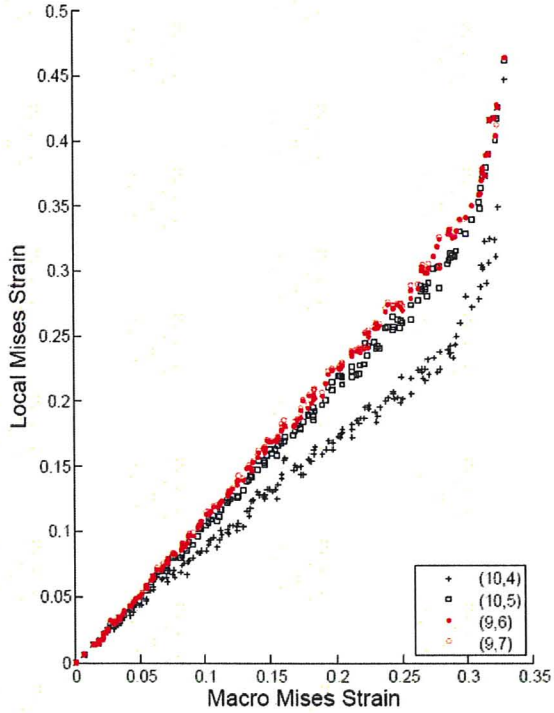

(f) Side B, A16B11

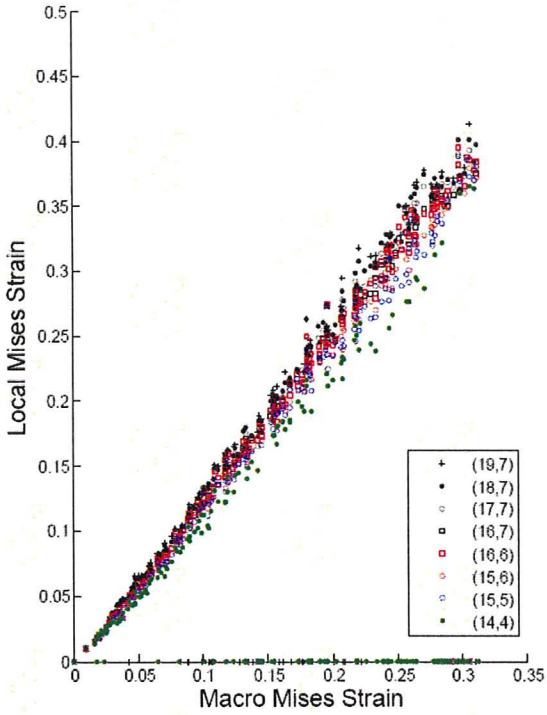

(g) Side A, A15B14

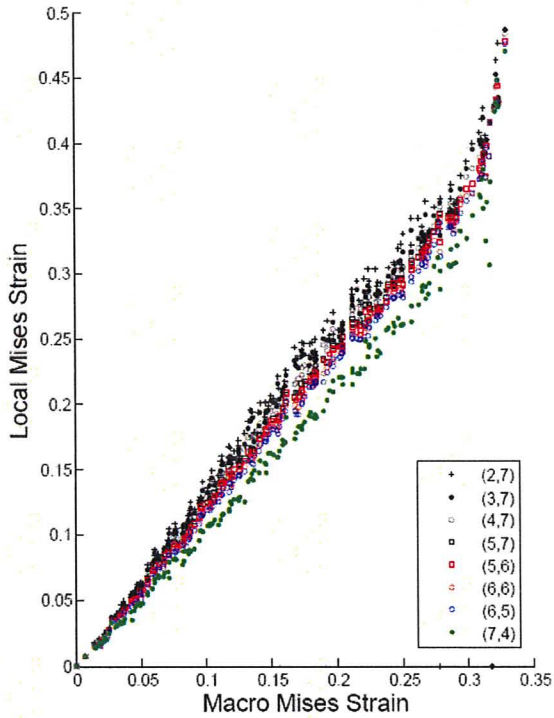

(h) Side B, A15B14

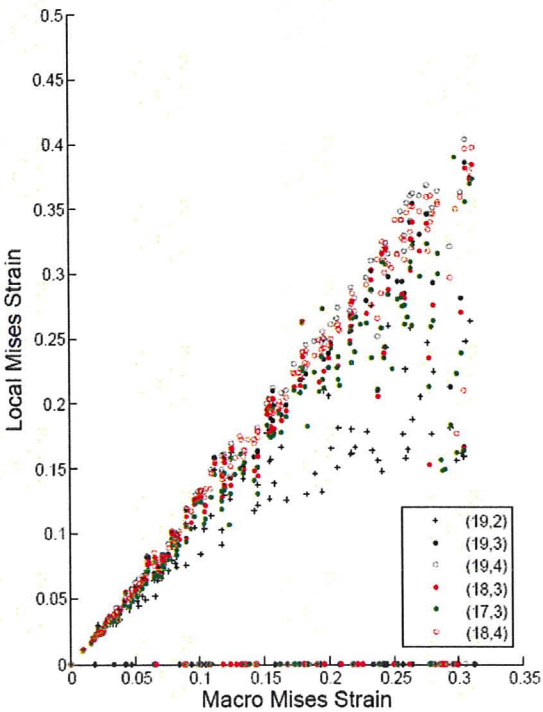

(i) Side A, A8B14

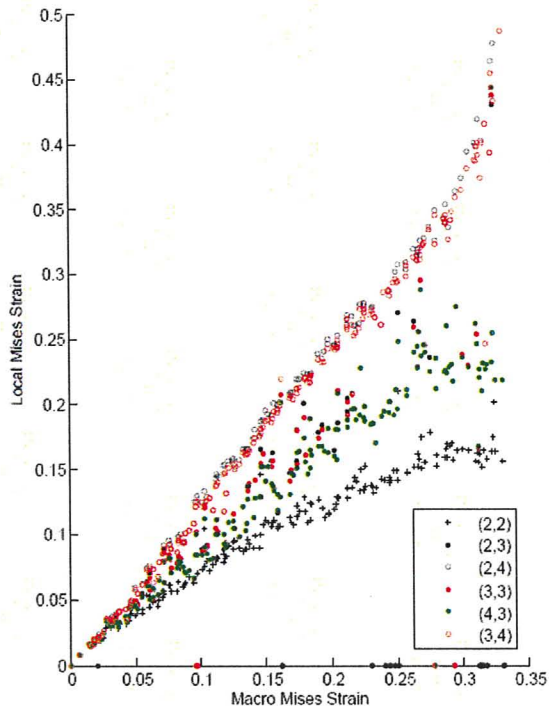

(j) Side B, A8B14

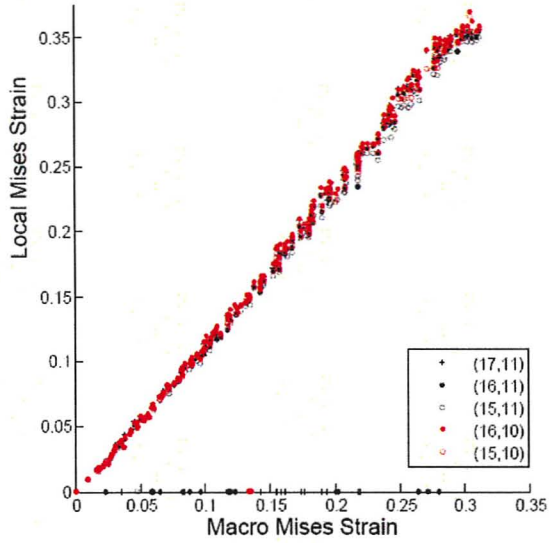

(k) Side A, A15B8

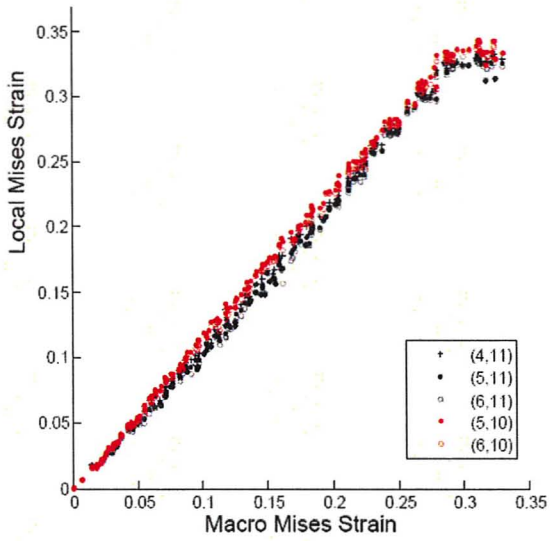

(l) Side B, A15B8

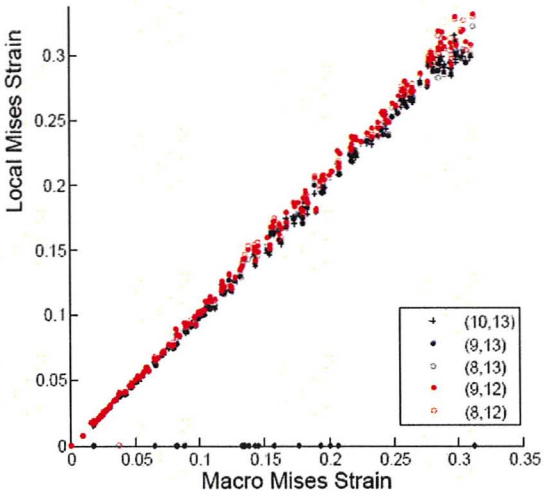

(m) Side A, A16B16

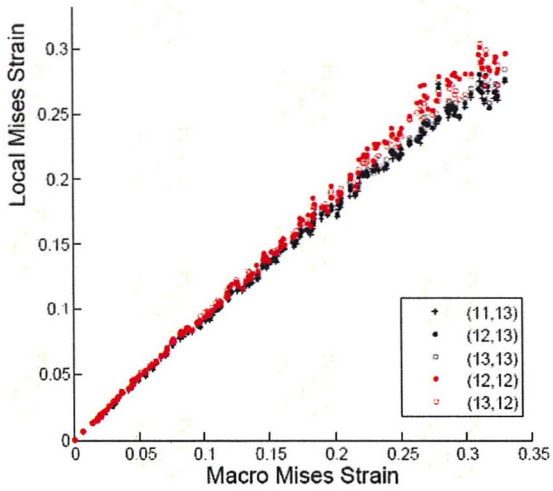

(n) Side B, A16B16

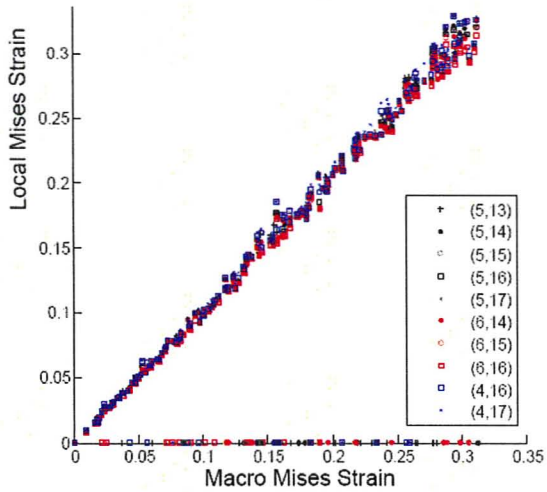

(o) Side A, A9B16

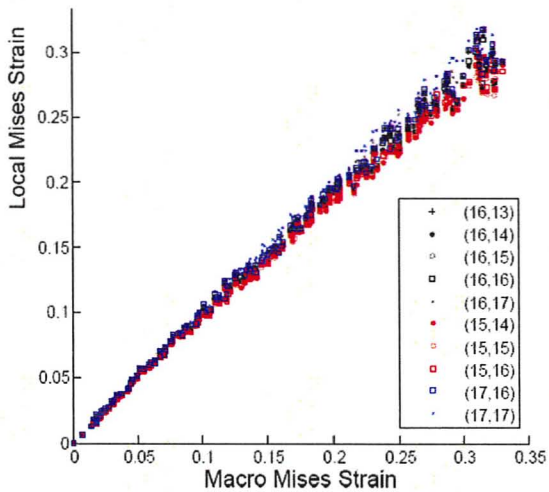

(p) Side B, A9B16

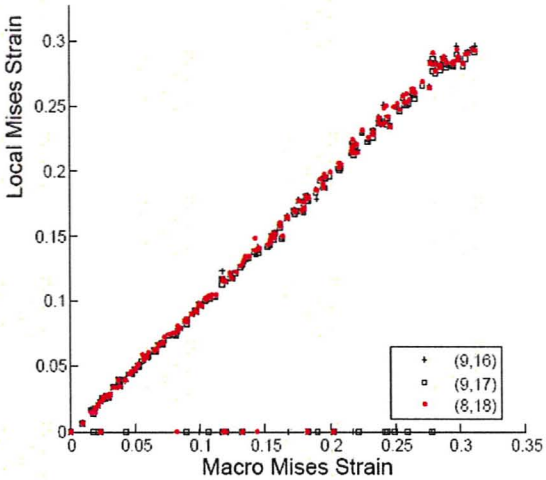

(q) Side A, A7B16

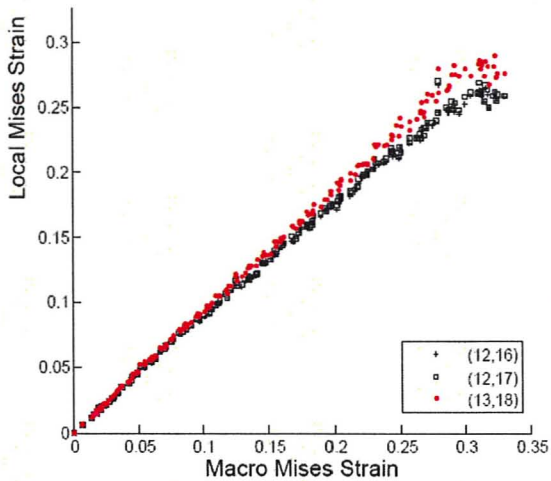

(r) Side B, A7B16

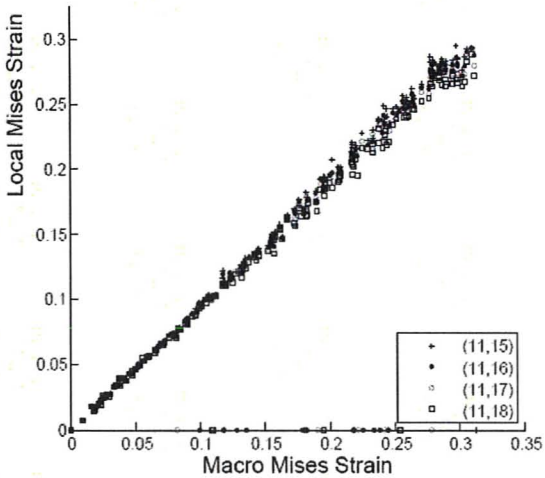

(s) Side A, A13B16

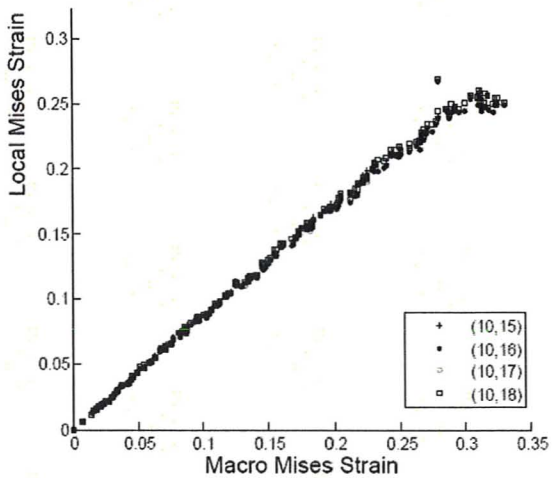

(t) Side B, A13B16

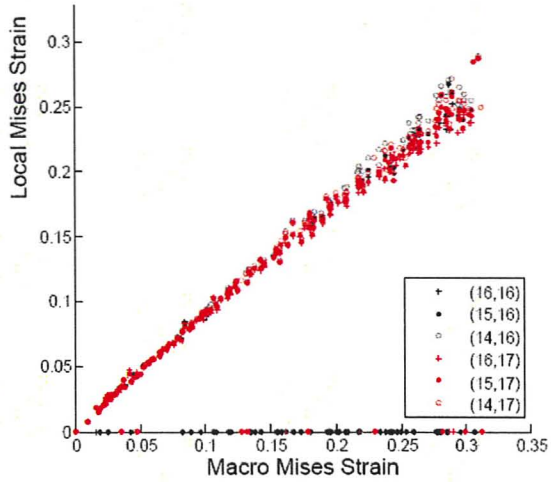

(u) Side A, A13B9

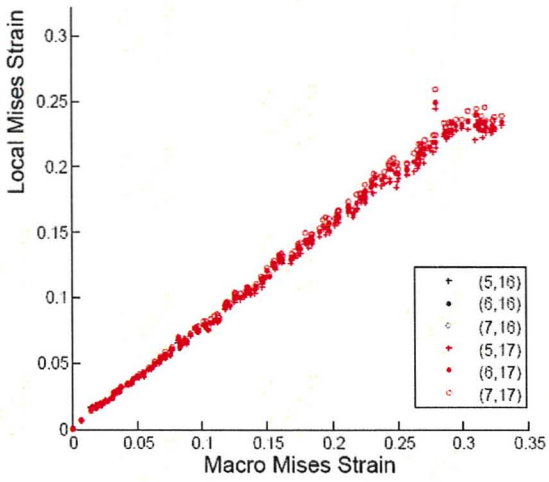

(v) Side B, A13B9

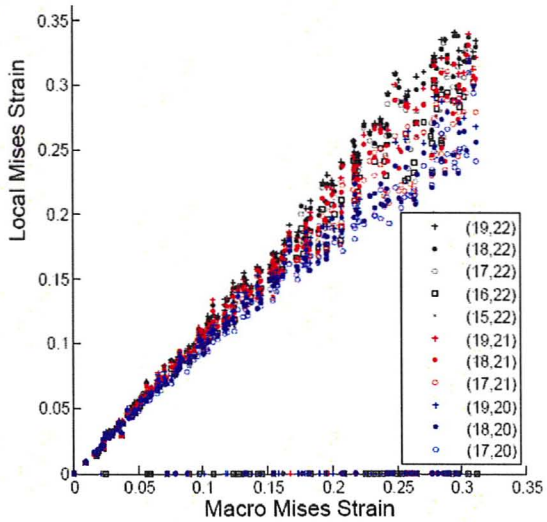

(w) Side A, A14B13

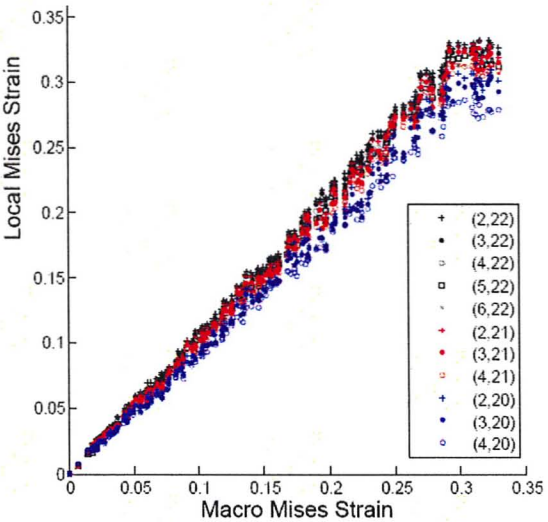

(x) Side B, A14B13

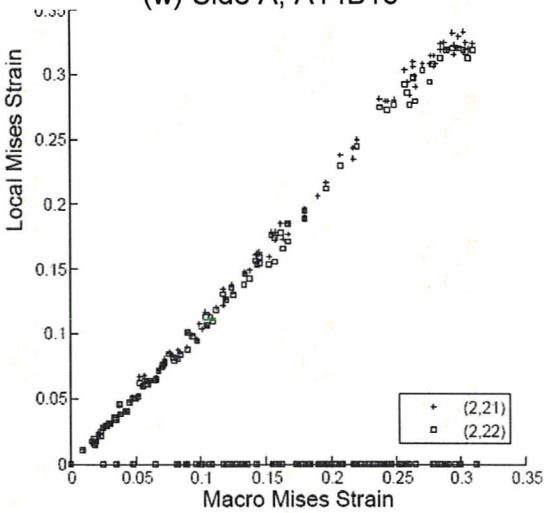

(y) Side A, A11B5

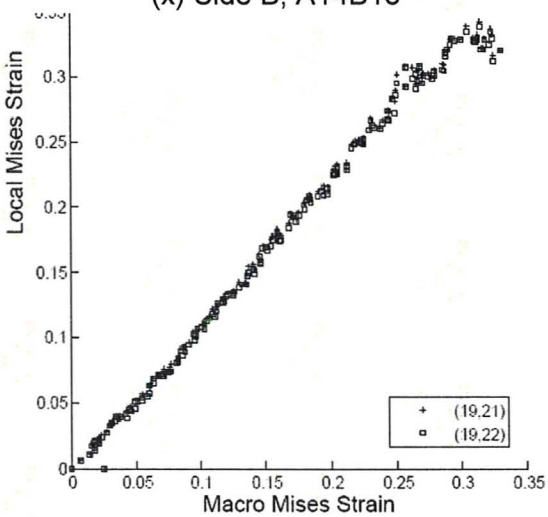

(z) Side A, A11B5

REFERENCES:

1. Hirsh, J., Automotive Trends in Aluminium - The European Prespective Materials Forum Volume, 2004. 28: p. 15-23.
2. Committee, A.I.H., ed. ASM Handbook: Vol 2. and Selection: Nonferrous Alloys and Special-Purpose Materials. ASM Handbook. Vol. 2. 1991, ASM International. 1328.
3. W.S.Miller, L.Zhuang, J.Bottema, A.J.Witterbrood, P.D. Smet, A.Haszler, and A.Vieregge, Recent Development in aluminium alloys for the automotive industry. Materials Science and Engineering A, 2000. 280: p. 37-49.
4. Kang, J.D., D.S. Wilkinson, D.V. Malakhov, H. Halim, M. Jain, J.D. Embury, and R.K. Mishra, Effect of processing route on the spatial distributions of constituent particles and their role in the fracture process in AA5754 alloy sheet materials. Materials Science and Engineering A, 2007. 456(1-2): p. 85-92.
5. Aghaie-Khafri, M. and R. Mahmudi, Flow localization and plastic instability during the tensile deformation of Al alloy sheet. Jom-Journal of the Minerals Metals & Materials Society, 1998. 50(11): p. 50-52.
6. Anand, L., K.H. Kim, and T.G. Shawki, Onset of Shear Localization in Viscoplastic Solids. Journal of the Mechanics and Physics of Solids, 1987. 35: p. 407--429.
7. Kang, J., D.S. Wilkinson, M. Jain, J.D. Embury, A.J. Beaudoin, S. Kim, R. Mishira, and A.K. Sachdev, On the sequence of inhomogeneous deformation processes occurring during tensile deformation of strip cast AA5754. Acta Materialia, 2006. 54(1): p. 209-218.
8. Aghaie-Khafri, M., Predicting flow localization and formability of aluminium alloy sheets. Proc. Instn Mech. Engrs 2004. 218(Part B: Engineering Manufacture): p. 1313-1321.
9. Penning, P., Mathematics of the Portevin-Le Chatelier Effect. Acta Metallurgica, 1972. 20(10): p. 1169-1175.
10. Casarotto, L., R. Tutsch, R. Ritter, J. Weidenmuller, A. Ziegenbein, F. Klose, and H. Neuhauser, Propagation of deformation bands investigated by laser scanning extensometry. Computational Materials Science, 2003. 26: p. 210-218.
11. Bruggemann, C., T. Bohlke, and A. Bertram, Modelling and Simulation of the Portevin-Le Chatelier Effect. 2008, Springer Berlin Heidelberg. p. 53-61.
12. Tong, W. and N. Zhang, On serrated plastic flow in an AA5052-H32 sheet. Journal of Engineering Materials and Technology-Transactions of the Asme, 2007. 129(2): p. 332-341.
13. Kok, S., A.J. Beaudoin, D.A. Tortorelli, and M. Lebyodkin, A finite element model for the Portevin-Le Chatelier effect based on polycrystal plasticity. Modelling and Simulation in Materials Science and Engineering, 2002. 10(6): p. 745-763.
14. Kok, S., A.J. Beaudoin, D.A. Tortorelli, M. Lebyodkin, L. Kubin, and C. Fressengeas, Simulation of the Portevin - Le Chatelier effect using polycrystal plasticity. Journal De Physique Iv, 2003. 105: p. 191-197.
15. McCormick, P.G., Dynamic Strain Aging Trans. Indian Inst. Met.,, 1986. 39: p. 98-106.

16. Hahner, P., A. Ziegenbein, E. Rizzi, and H. Neuhauser, Spatiotemporal Analysis of Portevin–Le Cha^telier Deformation Bands: Theory, simulation, and experiment. Physical Review B, 2002. 65(13): p. 134109(1-20).
17. K.Chihab, Y.Estrin, L.P. Kubin, and J. Vergnol, The kinetics of the Portevin-Le Chatelier bands in an Al-5at%Mg alloy Scripta Metallurgica, 1987. 21(2): p. 203-208.
18. Tong, W., H. Tao, N. Zhang, and L.G. Hector, Time-resolved strain mapping measurements of individual Portevin-Le Chatelier deformation bands. Scripta Materialia, 2005. 53(1): p. 87-92.
19. Kuhn, H., ed. ASM Handbook: Vol8: Mechanical Testing and Evaluation. ASM Handbook, ed. D. Medlin. Vol. 8. 2000, ASM International. 998.
20. Considére, A., Mémoire sur l'emploi du fer et de l'acier dans les constructions. Annls Ponts Chaussees, 1885. 9(6): p. 574.
21. Hart, E.W., Theory of the tensile test Acta Metallurgica, 1967. 15(2): p. 351-355.
22. Asaro, R.J. and A. Needleman, Overview no. 42 Texture development and strain hardening in rate dependent polycrystals. Acta Metallurgica, 1985. 33(6): p. 923-953.
23. Peirce, D., R.J. Asaro, and A. Needleman, Material Rate Dependence and Localized Deformation in Crystalline Solids. Acta Metallurgica, 1983. 31(12): p. 1951-1976.
24. McClintock, F.A., Plasticity aspects of fracture, in Fracture: An Advanced Treatise (ed. H.Liebowitz). 1971, NY: Academic Press: New York. p. 47-225.
25. R.Hill and J.W. Hutchinson, Bifurcation phenomena in the plane tension test. Journal of the Mechanics and Physics of Solids, 1975. 23(4-5): p. 239-264.
26. Marciniak, Z. and K. Kuczynski, Limit strains in the process of stretch-forming sheet metal. International Journal of Mechanical Sciences 1967. 9: p. 609-620.
27. Onyewuenyi, O.A., Microstructural Aspects of Flow Localization and Plastic Instability. Scripta Materialia, 1984. 18: p. 455-458.
28. Halim, H., D.S. Wilkinson, and M. Niewczas, The Portevin-Le Chatelier (PLC) effect and shear band formation in an AA5754 alloy. Acta Materialia, 2007. 55(12): p. 4151-4160.
29. Dillamore, I.L., J.G. Roberts, and A.C. Bush, Occurrence of Shear Bands in Heavily Rolled Cubic Metals Metal Science, 1979. 13(2): p. 73-77.
30. Kang, J.D., D.S. Wilkinson, J.D. Embury, M. Jain, and A.J. Beaudoin, Effect of type-B Portevin-Le Chatelier bands on the onset of necking in uniaxial tension of strip cast AA5754 sheets. Scripta Materialia, 2005. 53(5): p. 499-503.
31. Kang, J.D., D.S. Wilkinson, P.D. Wu, M. Bruhis, M. Jain, J.D. Embury, and R.K. Mishra, Constitutive behavior of AA5754 sheet materials at large strains. Journal of Engineering Materials and Technology-Transactions of the Asme, 2008. 130(3): p. -.
32. Wilson, D.V., Influences of Metallurgical Structure on Formability.
33. Blicharski, M., S. Dymek, and M. Wrobel, Inhomogeneities of Microstructure Evolved in Metals under Plastic Deformation Journal of Materials Processing Technology, 1995. 53: p. 75-84.
34. Duckham, A., R.D. Knutsen, and O. Engler, Influence of Deformation Variables on the Formation of Copper-type Shear Bands in Al-1Mg Acta Materialia, 2001. 49: p. 2739-2749.

35. Peirce, D., R.J. Asaro, and A. Needleman, Overview 21: An Analysis of Nonunform and Localized Deformation in Ductile Single Crystal. Acta Metallurgica, 1982. 30: p. 1087-1119.
36. Asaro, R.J. and A. Needleman, Flow Localization in Strain Hardening Crystalline Solids. Scripta Metallurgica, 1984. 18: p. 429-435.
37. Chang, Y.W. and R.J. Asaro, An Experimental Study of Shear Localization in Aluminum-copper Single Crystals Acta Metallurgica, 1981. 29(1): p. 241-257.
38. Nesterenko, V.F., M.A. Meryers, and T.W. Wright, Self-organization in the Initiation of Adiabtic Shear Bands. Acta Materialia, 1998. 46: p. 327-240.
39. I.Kovacs, Chinh.N.Q, and Kovacs-csetenyi.E, Grain size dependence of the work hardening process in Al99.99. Phys. stat.sol.(a), 2002. 194(1): p. 3-18.
40. Hansen, N., Hall-Petch relation and boundary strengthening. Scripta Materialia, 2004. 51: p. 801-806.
41. Tremblay, J.R. and C.A. Schuh, The Hall-Petch breakdown in nanocrystalline metals: A crossover to glass-like deformation. Acta Materialia, 2007. 55: p. 5948-5958.
42. L.V.Raulea, L.E.Govaert, and F.P.T.Baaijens, Grain and specimen size effects in processing metal sheets. Advanced Technology of Plasticity, 1999. 2: p. 19-24.
43. Margulies, L. and G. Winther, In Situ Measurement of Grain Rotation During Deformation of Polycrystals. Science 2001. 291: p. 2392-2394.
44. Winther, G., L. Margulies, H.F. Poulsen, S. Schmidt, A.W. Larsen, E.M. Lauridsen, S.F. Nielsen, and A. Terry, Lattice Rotation of Individual Bulk Grains during Deformation. Materials Science Forum, 2002. 408-412: p. 287-292.
45. Tatschl, A. and O. Kolednik, On the Experimental Characterization of Crystal Plasticity in Polycrystals Materials Science and Engineering A, 2003. 342: p. 152-168.
46. Mao, W. and Y. Yu, Effect of Elastic Reaction Stress on Plastic Behaviors of Grains in Polycrystalline Aggregate during Tensile Deformation. Materials Science and Engineering A, 2004. 367: p. 277-281.
47. Shen, Y.-L., On the Shear Band Formation in F.c.c. Metals. Scripta Metallurgica, 1991. 25: p. 1081-1085.
48. P.Franciosi and A.Zaoui, Multislip in f.c.c. crystals: a theoretical approach compared with experimental data. Acta Metallurgica 1982. 30(8): p. 1627.
49. Franciosi, P. and A. Zaoui, Multislip tests on copper crystals: A junctions hardening effect. Acta Metallurgica, 1982. 30(12): p. 2141-2151.
50. Havner, K.S., On lattice and material-frame rotations and crystal hardening in high-symmetry axial loading. Philosophical Magazine, 2005. 85(25): p. 2861 - 2894
51. Zaefferer, S., J.-C. Kuo, Z. Zhao, M. Winning, and D. Raabe, On the influence of the grain boundary misorientation on the plastic deformation of aluminum bicrystals. Acta Materialia, 2003. 51(16): p. 4719-4735.
52. Wright, S.I. and D.P. Field, Recent studies of local texture and its influence on failure. Materials Science and Engineering a-Structural Materials Properties Microstructure and Processing, 1998. 257(1): p. 165-170.
53. Lee, W.B. and K.C. Chan, Effect of Local Texture on the Development of M-K Groove in Biaxial Deformation. Textures and Microstructure, 1991. 14-18: p. 1221-1226.

54. Wu, P.D., A. Graf, S.R. MacEwen, D.J. Lloyd, M. Jain, and K.W. Neale, On forming limit stress diagram analysis. Internaional Journal of Solids and Structures, 2005. 42: p. 2225-2241.
55. Anand, L. and W.A. Spitzig, Initiation of Localized Shear Bands in Plane Strain. Journal of the Mechanics and Physics of Solids, 1980. 28: p. 113-128.
56. Korbel, A. and P. Martin, Microstructural events of macroscopic strain localization in prestrained tensile specimens. Acta Metallurgica, 1988. 36(9): p. 2575-2586.
57. Huang, J.C. and G.T. Gray III, Microband formation in shock-loaded and quasi-statically deformed metals. Acta Metallurgica, 1989. 37(12): p. 3335-3347.
58. Raabe, D., M. Sachtleber, Z. Zhao, F. Roters, and S. Zaefferer, Micromechanical and macromechanical effects in grain scale polycrystal plasticity experimentation and simulation. Acta Materialia, 2001. 49(17): p. 3433-3441.
59. Zhao, Z., M. Ramesh, D. Raabe, A. Cuitino, and R. Radovitzky, Investigation of three-dimensional aspects of grain-scale plastic surface deformation of an aluminum oligocrystal. International Journal of Plasticity, 2008.
60. Zhang, N. and W. Tong, An experimental study on grain deformation and interactions in an Al-0.5%Mg multicrystal. International Journal of Plasticity 2004. 20: p. 523-542.
61. Kang, J., M. Jain, D.S. Wilkinson, D. Embury, S. Kim, and A.K. Sachdev, Effect of Strain Path Change on Forming Limits of Strip Cast Automotive Aluminum Sheets AA5754, in Dislocations, Plasticity and Metal Forming, Tenth Int.Symp. on Plasticity and Its Current Applic., NEAT Press,. 2003. p. 181-183.
62. Sarkar, J., T.R.G. Kutty, D.S. Wilkinson, J.D. Embury, and D.J. Lloyd, Characterization of bendability in automotive aluminum alloy sheets. Aluminium Alloys: Their Physical and Mechanical Properties, Pts 1-3, 2000. 331-3: p. 583-588.
63. Kang, J.D., D.S. Wilkinson, J.D. Embury, and K. Hussain, Investigation on mechanism of ductile fracture of AA5754 sheet, in Aluminium Alloys 2006, Pts 1 and 2. 2006. p. 985-990.
64. Spencer, K., S.F. Corbin, and D.J. Lloyd, The influence of iron content on the plane strain fracture behaviour of AA 5754 Al-Mg sheet alloys. Materials Science and Engineering a-Structural Materials Properties Microstructure and Processing, 2002. 325(1-2): p. 394-404.
65. Yu, C.Y., P.W. Kao, and C.P. Chang, Transition of tensile deformation behaviors in ultrafine-grained aluminum. Acta Materialia, 2005. 53(15): p. 4019-4028.
66. Picu, R.C., A mechanism for the negative strain-rate sensitivity of dilute solid solutions. Acta Materialia, 2004. 52(12): p. 3447-3458.
67. N.Chung, J.D. Embury, R.G. Hoagland, and C.M. Sargent, Unstable Shear Failure in a 7075 Aluminum Alloy. Acta Metallurgica, 1977. 25: p. 377-381.
68. Kang, J.D., D.S. Wilkinson, M. Bruhis, M. Jain, P.D. Wu, J.D. Embury, R.K. Mishra, and A.K. Sachdev, Shear localization and damage in AA5754 aluminum alloy sheets. Journal of Materials Engineering and Performance, 2008. 17(3): p. 395-401.
69. Beaudoin, A.J., J.D. Bryant, and D.A. Korzekwa, Analysis of Ridging in Aluminum Auto Body Sheet Metal Metallurgical and Materials Transactions a-Physical Metallurgy and Materials Science, 1998. 29(9): p. 2323-2332.
70. Becker, R., Effects of strain localization on surface roughening during sheet forming Acta Materialia, 1998. 46(4): p. 1385-1401.

71. Christoffersen, J. and J.W. Hutchinson, A class of phenomenological corner theories of plasticity. J. Mech. Phys. Solids 1979. 27: p. 465–487.
72. Hirsh, J. and K. Lucke, Overview no.76. Acta Metallurgica 1988. 36(11): p. 2883-2904.
73. Houtte, P.V., S. Li, M. Seefeldt, and L. Delannay, Deformation texture prediction: from the Taylor model to the advanced Lamel model. International Journal of Plasticity, 2005. 21: p. 589-624.
74. Mao, W.-M., Modeling of rolling texture in aluminum. Materials Science and Engineering A, 1998(257): p. 171-177.
75. Gambin, W., ed. Plasticity and Textures. 1 ed. 2001, Springer. 99-100.
76. Hu, X.H., M. Jain, D.S. Wilkinson, and R.K. Mishra, Microstructure-based finite element analysis of strain localization behavior in AA5754 aluminum sheet. Acta Materialia, 2008. 56(13): p. 3187-3201.
77. Huang, Y., A User-material Subroutine Incorporating Single Crystal Plasticity in the Abaqus Finite Element Program. 1991, Division of Applied Sciences, Harvard University: Cambridge.
78. Delaire, F., J.L. Raphanel, and C. Rey, Plastic heterogeneities of a copper multicrystal deformed in uniaxial tension: experimental study and finite element simulations. Acta Materialia, 2000. 48(5): p. 1075-1087
79. Cheong, K.-S. and E.P. Busso, Effects of lattice misorientations on strain heterogeneities in FCC polycrystals. Journal of the Mechanics and Physics of Solids, 2006. 54: p. 671-689.
80. Wilson, D.V., A.R. Mirshams, and W.T. Roberts, An experimental study of the effects of sheet thickness and grain size on limit-strains in biaxial stretching International journal of mechanical sciences, 1983. 25(12): p. 859-870
81. Hu, X.H., D.S. Wilkinson, M. Jain, and R.K. Mishra, Modeling strain localization using a plane stress two-particle model and the influence of grain level matrix inhomogeneity. Journal of Engineering Materials and Technology-Transactions of the Asme, 2008. 130(2): p. -.
82. Weck, A., D.S. Wilkinson, H. Tocla, and E. Maire, 2D and 3D Visualization of Ductile Fracture. Advanced Engineering Materials, 2006. 8(6): p. 469-472.
83. Tvergaard, V. and A. Needleman, Three dimensional microstructural effects on plane strain ductile crack growth. International Journal of Solids and Structures, 2006. 43(20): p. 6165-6179.
84. Sheng, P.-J., J.-M. Quan, and M.-P. Tian, eds. The Foundation of Materials Science. 1998: Beijing.
85. Braunschweig, Aramis V4.7 Manual. 2001: GOM mbH.
86. Hu, X.H., unpublished work. 2009.
87. K.Sztwiertnia and J.Pospoech, Reduction of Misorientation between Two Cubic Crystals into the Base Domain of Axis-angle Space. Textures and Microstructure, 1990. 12: p. 233-242.
88. M.Humbert, N.Gey, J.Muller, and C.Esling, Determination of a Mean Orientation from a Cloud of Orientation. Application to Electron Back-Scattering Pattern Measurements. Journal of Applied Crystal, 1996. 26: p. 662-666.